

AN ABSTRACT OF THE THESIS OF

Craig M. Smith for the degree of Master of Science in Atmospheric Sciences
presented on September 4, 2003.

Title: A Modeling Study of Katabatic Flows

Redacted for Privacy

Abstract approved: _____.

A modeling study is undertaken to better understand the physics of katabatic flows. This study is divided into three topics; a comparison between a large eddy simulation (LES) and a mesoscale model of katabatic flows, a sensitivity study of katabatic flows to various physical parameters, and an investigation into the effect of subgrid scale terrain features on katabatic flow models. In the first topic, a comparison between LES, and a mesoscale model, ARPS, of katabatic flows is made to better quantify the accuracy of subgrid parameterization in ARPS. It is shown that, although the modeled flows agree on a number of parameters, the LES model produces a lower and faster jet than that of ARPS, and also cools more near the surface. The momentum budgets of the two models agree well with each other. The ARPS model has a higher amount of TKE than the LES model, due to an overproduction by shear in the ARPS subgrid parameterizations.

The second portion of this thesis represents a sensitivity study of katabatic flows to various physical parameters. The depth and strength of katabatic flows are shown to vary with surface heat fluxes, slope angle, and ambient stratification. Katabatic flows are shown to grow in depth and magnitude as slope angle increases, due to an increase in entrainment of overlying ambient air. The ratio of advection to mixing is shown to collapse to a near universal value regardless of surface heat fluxes. With increasing ambient stratification, entrainment in katabatic flows becomes small and the momentum equation is reduced to a two-way balance between buoyancy and drag. In this case, the heat flux of entrained air into the katabatic flow approaches that of the surface cooling, and the flow ceases to grow in the down-slope direction. Finally, predictions for bulk velocity and buoyancy strength scales are developed as a function of slope angle and surface heat fluxes.

The last portion of this study focuses on the effect of subgrid scale terrain features on katabatic flows. It is shown that in areas of inadequate terrain resolution, the effect of the terrain smoothing routine in ARPS is to increase the slope height in areas of concave mountains. The concept of energy conversion in katabatic flows is introduced, and it is shown that the effect of raising terrain is to assign parcels more buoyant potential energy than they would otherwise have, and thus over-predict the magnitude of katabatic flows. Finally, an investigation into the effect of changing upper slope angle on katabatic flows over combined slopes is made. It is concluded that a combined slope cannot be predicted using a linear combination of simple slopes, since the transition portion of the slope results in a turbulent hydraulic jump with enhanced mixing. The magnitude of mixing in the turbulent hydraulic jump in combined slopes is shown to depend on the difference between upper and lower slope angle.

A Modeling Study of Katabatic Flows

by

Craig M. Smith

A THESIS

submitted to

Oregon State University

in partial fulfillment of

the requirements for the

degree of

Master of Science


Presented September 4, 2003

Commencement June 2004

Master of Science thesis of Craig M. Smith presented on September, 4 2003.

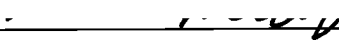
Approved:

Redacted for Privacy



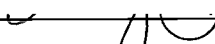
Major Professor, representing Atmospheric Sciences

Redacted for Privacy



Dean of College of Oceanic and Atmospheric Sciences

Redacted for Privacy



Dean of Graduate School

I understand that my thesis will become part of the permanent collection of Oregon State University libraries. My signature below authorizes release of my thesis to any reader upon request.

Redacted for privacy



Craig M. Smith, Author

ACKNOWLEDGMENTS

I would like to express thanks and appreciation to my adviser, Dr. Eric Skyllingstad, for providing me with an interesting research topic and being an endless source of guidance and help to improve my study. It has been my pleasure to work with him. I would also like to thank the members of my committee, Dr. Roger Samelson, Dr. Larry Mahrt, and Dr. Douglas Markle, for their comments on this research as well.

I would like to thank the Atmospheric Sciences faculty whom I have taken classes from and TA'ed for here at Oregon State University. I would also like to thank the students of the department as well, in particular Mark Matheson and Nicolai Thum, for their help.

I would also like to thank my family back home in San Diego, for their support of my ever-changing career path. I would like to thank my friends as well, especially Sara Wright, for always brightening my spirits. Finally I would like to thank my cat Panda, without whom I would never have had the inspiration to come here in the first place.

This work was supported by the U.S. Department of Energy, under the auspices of the Atmospheric Sciences Program of the Office of Biological and Environmental Research, Grant DE-FG03-99ER62840, and used resources of the National Energy Research Scientific Computing Center, which is supported by the Office of Science of the U.S. Department of Energy under contract No. DE-AC03-76SF00098.

TABLE OF CONTENTS

1. Introduction	1
1.1 Motivation	1
1.2 Background	7
1.3 Description of the current study	17
2. Study of Simple Slopes	19
2.1 Model introduction	19
2.2 Comparison between ARPS and LES results	24
2.3 The effect of surface heat fluxes	32
2.4 The effect of slope angle	48
2.5 The effect of ambient stratification	61

TABLE OF CONTENTS (Continued)

3. Study of Combined Slopes versus Simple Slopes	73
3.1 Simple versus combined slope	71
3.2 The equivalent slope angle method	83
4. Conclusions	92
References	97

LIST OF FIGURES

<u>Figure</u>	<u>Page</u>
1.1 Close up of model domains over the Salt Lake City Valley.	5
1.2 Profiles of terrain on the west side of the Salt Lake City Valley.	6
1.3 Schematic of velocity and potential temperature profiles for katabatic flows.	7
2.1 Three dimensional view of ARPS model domain and mountain.	20
2.2 Three dimensional view of LES model domain.	23
2.3 X-Z cross section of ARPS model domain for $\alpha = 14$ degrees.	24
2.4 Velocity and potential temperature profiles of LES and ARPS model at a location 5.9 km downslope.	25
2.5 Momentum budget for LES and ARPS model at a location 5.9 km downslope.	27
2.6 TKE as a function of height for LES and ARPS model at a location 5.9 km downslope.	29
2.7 TKE budget as a function of height for the LES and ARPS model at a location 5.9 km downslope.	30
2.8 X-Z cross section of ARPS modeling domain for surface heat flux and ambient stratification study runs.	32
2.9 X-Z cross section of the downslope evolution of potential temperature fields for $Q_0 = 20, 50, \text{ and } 100 \text{ W/m}^2$	34
2.10 X-Z cross section of the downslope evolution of velocity fields for $Q_0 = 20, 50, \text{ and } 100 \text{ W/m}^2$	35
2.11 Velocity profiles as a function of height for surface heat flux runs at 6.5 km downslope.	36

LIST OF FIGURES (Continued)

<u>Figure</u>	<u>Page</u>
2.12 Buoyancy deficit profiles as a function of height for surface heat flux runs at 6.5 km downslope.	36
2.13 Buoyancy, advection, and mixing and drag terms in the total momentum budget as a function of downslope distance for surface heat flux runs.	37
2.14 Buoyancy normalized momentum budget (top two) and advection to mixing ratio as a function of down-slope distance for surface cooling runs.	39
2.15 Buoyancy strength scale versus downslope distance for surface heat flux runs.	42
2.16 Velocity strength scale versus downslope distance for surface heat flux runs.	43
2.17 The coefficient of velocity strength scale versus surface heat flux.	43
2.18 The coefficient of buoyancy strength scale versus surface heat flux.	44
2.19 Buoyant potential energy and kinetic energy versus downslope distance for surface heat flux runs.	46
2.20 Katabatic efficiency versus surface heat flux.	47
2.21 X-Z cross section of ARPS model domain for slope angle study runs.	48
2.22 X-Z cross section of the downslope evolution of velocity fields for $\alpha = 4, 10$, and 16 degrees.	50
2.23 X-Z cross section of the downslope evolution of potential temperature fields for $\alpha = 4, 10$, and 16 degrees.	51
2.24 Velocity profiles as a function of height for slope angle runs at 5 km downslope.	52

LIST OF FIGURES (Continued)

<u>Figure</u>	<u>Page</u>
2.25 Buoyancy deficit profiles as a function of height for slope angle runs at 5 km downslope.	52
2.26 Along slope momentum budget 5 km downslope as a function of slope angle.	53
2.27 Velocity strength scales versus downslope distance for slope angle runs.	54
2.28 Buoyancy strength scales versus downslope distance for slope angle runs.	54
2.29 The coefficient of velocity strength scale versus sine of slope angle.	57
2.30 The coefficient of buoyancy strength scale versus sine of slope angle.	57
2.31 Buoyant potential energy and kinetic energy versus downslope distance for slope angle runs.	59
2.32 Katabatic efficiency versus sine slope angle.	60
2.33 X-Z cross section contour of downslope velocity profiles for the neutral, $\Gamma = 2$ K/km, and $\Gamma = 6$ K/km cases.	63
2.34 X-Z cross section contour of potential temperature profiles for the neutral, $\Gamma = 2$ K/km, and $\Gamma = 6$ K/km cases.	64
2.35 Velocity profiles as a function of height for ambient stratification runs at 6.5 km downslope.	65
2.36 Potential temperature deficit profiles as a function of height for ambient stratification runs at 6.5 km downslope.	65
2.37 Along slope momentum budget as a function of height for ambient stratification runs 6.5 km downslope.	66

LIST OF FIGURES (Continued)

<u>Figure</u>	<u>Page</u>
2.38 Buoyancy, advection, and mixing and drag terms in the total momentum budget as a function of downslope distance for ambient stratification runs.	67
2.39 Buoyancy normalised momentum budget (top two) and advection to mixing ratio as a function of down-slope distance for ambient stratification runs	69
2.40 Buoyancy strength scale versus distance as a function for ambient stratification runs.	70
2.41 Velocity strength scale versus distance as a function for ambient stratification.	70
2.42 Buoyant potential energy and kinetic energy versus downslope distance for ambient stratification runs.	71
2.43 Katabatic efficiency versus ambient stratification.	72
3.1 X-Z cross section of the right half of the ARPS modeling domain for combined slope study runs, showing simple and combined slope profiles.	74
3.2 Velocity profiles of simple and combined slopes at locations A, B, and C.	75
3.3 X-Z cross section of the downslope evolution of velocity fields for simple and combined slope flows.	76
3.4 Potential temperature deficit profiles of simple and combined slopes at locations A, B, and C.	76
3.5 TKE profiles as a function of height for simple and combined slope flows at locations A, B, C.	77
3.6 Total turbulent kinetic energy as a function of downslope distance for combined and simple slopes.	78
3.7 Velocity strength profiles as a function of downslope distance for simple and combined slope flows.	78

LIST OF FIGURES (Continued)

<u>Figure</u>	<u>Page</u>
3.8 Buoyancy strength profiles as a function of downslope distance for simple and combined slope flows.	79
3.9 Advection to mixing ratio as a function of down-slope distance for simple and combined slope flows.	81
3.10 Buoyant potential energy and kinetic energy versus downslope distance for simple and combined slope flows.	82
3.11 X-Z cross section of the right half of the ARPS modeling domain for upper slope angle combined slope study runs, and location A, where the flows will be compared.	84
3.12 Graphical representation of equivalent slope angle method.	85
3.13 X-Z cross section of the downslope evolution of velocity fields for combined slopes and simple slope flows. $\alpha_2 = 9.2$ for the top plot, $\alpha_2 = 14.5$ for the middle plot, and $\alpha_2 = \alpha_1 = 5.7$ for the bottom plot.	86
3.14 Downslope evolution of velocity strength scales for the upper slope angle cases.	87
3.15 Equivalent slope angle versus combined slope angle ratio for the equivalent slope angle method.	88
3.16 Total turbulent kinetic energy as a function of downslope distance for upper slope angle runs.	91
3.17 Buoyancy, advection, and mixing and drag terms in the total momentum budget as a function of downslope distance for upper slope angle runs.	91

LIST OF TABLES

<u>Table</u>	<u>Page</u>
2.1 The variation of velocity and buoyancy strength scale coefficients with surface heat fluxes	42
2.2 The variation of velocity and buoyancy strength scale coefficients with slope angle	56

A Modeling Study of Katabatic Flows

1. Introduction

Cold air drainage flows are a common occurrence in nocturnal boundary layers over complex terrain. As such, these flows represent an important part of our understanding of complex terrain meteorology and transport and mixing in stable boundary layers.

1.1 Motivation

Much progress in modeling slope flows has been made in the past few decades. Models of terrain induced atmospheric processes, however, are constrained by terrain resolution. Since katabatic flows are inherently a terrain induced flow, it follows that accurate modeling of them requires high resolution of terrain features. In this respect, models of atmospheric boundary layer processes are constrained by the power of computers. In modeling a certain domain, one has to choose a grid resolution coarse enough to ensure the model will be done in a timely fashion, and fine enough to pick up the smaller scale aspects of the flow.

Most current operational mesoscale models are run at grid resolutions between 4 and 36 km. Typically the model terrain is smoothed over using a filter. Whereas at smaller grid spacing, less smoothing is required to produce a surface that is acceptable to the model, and hence more terrain irregularities are picked up,

at higher grid spacing, many smaller features in areas of complex terrain are filtered out and inadequately resolved. This study will look at possible errors that may be introduced by subgrid scale terrain features in mesoscale model forecasts over areas of complex terrain. In particular, a part of this study will focus on the systematic differences between katabatic flows over simple slopes, and those with a slope angle that is not constant. Information about the models of simple and combined slopes will help us tailor drainage flow predictions in areas of inadequate terrain resolution, and produce qualitative relationships about the role of subgrid scale terrain features in katabatic flows.

An example of this phenomena lies in the vertical mixing and transport (VTMX) data set that was taken in Utah in 2000. As an example of the effect of grid spacing is presented below. A close up view of the of model domains over the Salt Lake City Valley is pictured in figure 1.1. Horizontal grid spacing in the models is 5 km (top), 2.5 km (middle), and 1 (km). A cross section is taken through the valley, near the southern tip of the Salt Lake, indicated by the solid line. The terrain profile along the eastern side of the valley in this cross section is shown in figure 1.2. This figure shows that as grid spacing is increased the terrain is changed in two distinctive ways. First, increased grid spacing tends to reduce the height of the peaks, generating an overall gentler slope, and less potential energy input into the system. Second, in the vicinity of the slope angle change, the level of terrain is raised. It is this phenomena that we are most interested in, since the effect of raising the terrain is to assign parcels more potential energy than they would otherwise have, and assigning parcels more energy should lead to greater increases of kinetic energy down-slope. To learn more about this effect, the results of a

sensitivity study of katabatic flows to slope angle will be used in predictions of combined slope flow parameters.

There are also other fundamental aspects of slope flows that have yet to be fully explored. For example, we have information on the role of ambient stratification in inhibiting the growth of slope flows, although it has been suggested that in highly stratified environments, slope flows will become one dimensional with the surface cooling balanced by the entrainment of warmer ambient overlying air. One of the goals of this study is to examine the effect that ambient stratification has on cold air drainage flows, and examine the relationship of the growth of cold air drainage flows and the turbulent entrainment of warmer ambient air.

In addition, the mechanisms that determine the surface cooling that drives flow down slopes are poorly understood. Observational evidence is lacking for the myriad surface cooling regimes applied in katabatic flow models up to date. In the past, modelers have employed a wide variety of thermodynamic boundary conditions over the slope to drive the flow. A sample of the methods include prescribing a temperature difference between the surface and air just above the surface as in Davies et al (1995), specifying a constant heat flux as in Manins and Sawford (1979), and Bader and Mckee (1983), decreasing the surface temperature until a specified ground temperature deficit is achieved and then holding the surface heat flux constant from then on as in Nappo and Rao (1987), and using a full radiation and surface physics package as in McNider and Pielke (1984) and Yamada (1981). However, none of these thermodynamic surface boundary conditions seem to be justified from observational data, and furthermore, most

boundary layer parameterizations used in mesoscale models have been formulated from observational studies over flat ground. It is not known how well or if these parameterizations work for flows over slopes. Therefore, another goal of this study is to determine what effect surface heat flux has on models of katabatic flows.

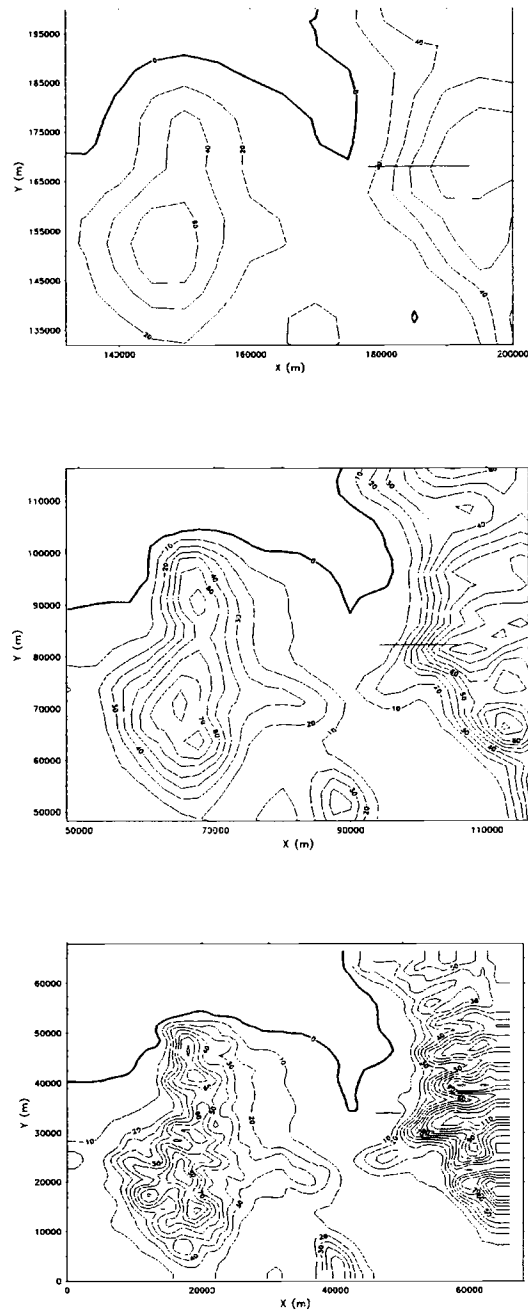


Figure 1.1: Close up of model domains over the Salt Lake City Valley. Salt Lake is in the upper left-hand corner of the domains. Grid spacing in the models in 5 km (top), 2.5 km (middle), and 1 km (bottom). Terrain profile is indicated by the line across the right hand side of the valley, near the southern tip of the Salt Lake.

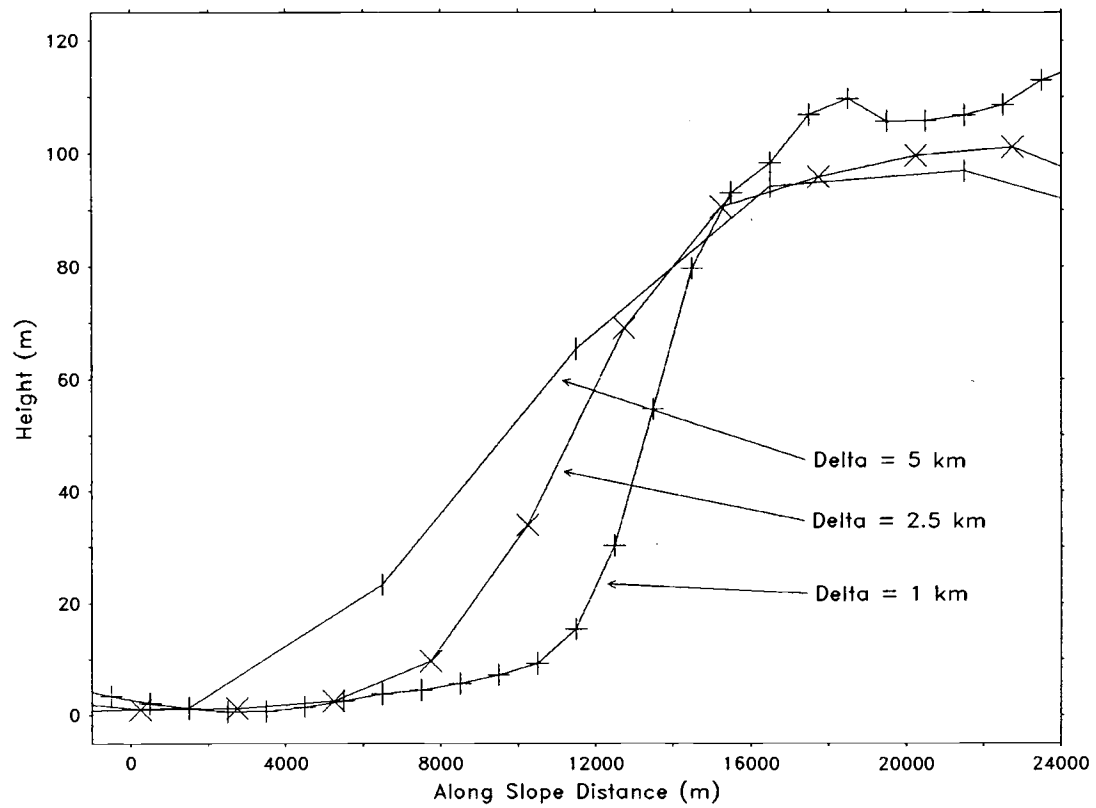


Figure 1.2: Profiles of terrain on the west side of the Salt Lake City Valley. +, |, and X, represent grid points in the models with 1 km, 2.5 km, and 5km horizontal grid spacing respectively.

1.2 Background

A depiction of cold air drainage flows is presented in figure 1.3, where Q_0 is the surface cooling applied over the entire slope that is driving the flow. For simplicity we use a coordinate system tilted to the horizontal so that the s -coordinate and n -coordinates are in the down-slope and slope-normal directions respectively. We will ignore cross slope effects on the flow, and consider the flow to be essentially two dimensional. Katabatic flows are driven by surface cooling, which causes air near the surface of a slope to increase in density and flow downhill. In the absence of solar heating, the Earth's surface cools by longwave radiation while air adjacent to the surface cools by conduction. The result is that parcels near the surface of a slope become denser than parcels at the same height away from the slope, thus generating a gradient in buoyancy that drives cooler, denser air near the surface downhill.

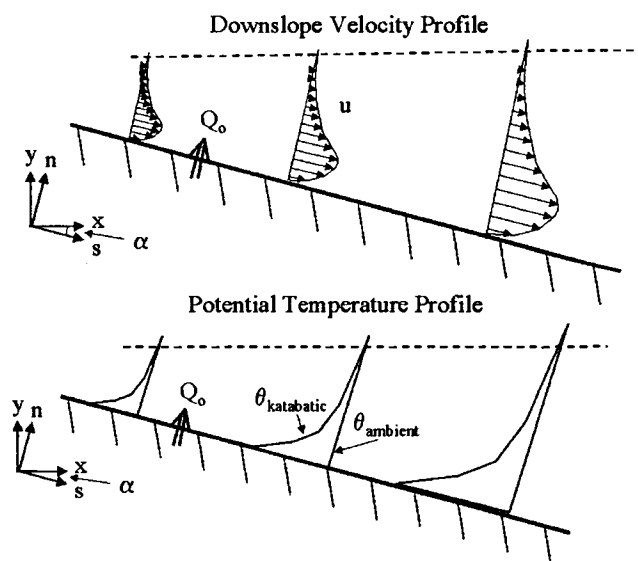


Figure 1.3: Schematic of velocity (left) and potential temperature (right) profiles for katabatic flows.

Early studies of cold air drainage flows focused on finding analytical solutions for slope flows through the use of restrictive assumptions on terms in the momentum budget and turbulent eddy diffusivities. These studies have typically neglected temporal variations, down-slope evolution of the flow, turbulent flux divergence, or entrainment of ambient air into the flow, in obtaining analytical profiles of down-slope flows. Manins and Sawford (1979) recognized that analytical descriptions of the temporal and spatial evolution of slope flows that do not include restrictive assumptions appear unattainable. That is, only by neglecting physics such as advection and assuming constant eddy diffusivity coefficients are analytical solutions to slope flows possible.

In the past 20 years there has been a series of numerical modeling studies of katabatic flows. In numerical models, restrictive assumptions about the flow do not need to be made in order to gain insight into the physics. Typically, however, these studies have focused on the effects of mean synoptic scale flow and stable stratification on slope flows. A few investigators have explored the effect of surface heat fluxes, slope angle, and valley width/height ratio in their studies. Studies on the effect of a changing slope angle on a simple slope flows are almost nonexistent.

One of the first analytical solutions to slope flows was proposed by Prandtl (1942). In his one dimensional model, the flow is assumed to be steady and invariant in the down-slope direction, and the slope angle is assumed to be small. Advection is neglected in the momentum budget so that the buoyancy term is balanced by turbulent flux divergence, and eddy diffusivities are assumed constant

with height in the drainage flow. Entrainment of warmer, overlying air into the drainage flow is neglected, emphasizing the importance of mixing and drag in the model. Businger and Rao (1965) neglect the turbulent momentum transport and the buoyancy term is balanced by the down-slope advection of momentum. More recent studies have shown that in some slope flows the entrainment term accounts for a relatively small portion of the momentum budget, justifying Prandtl's neglect of advection to certain extent and making his model useful for predictions of many of the flows that have been studied observationally.

Subsequent models of drainage flows focused on adding more physics to Prandtl's model. Defant (1949) extended Prandtl's approach to large slope angles and modified the eddy diffusivities to obtain good agreement with observations on a steep slope in the Innsbruck Range. Ball (1956) extended Prandtl's approach to include advection, but neglected entrainment processes, while Ellison and Turner (1959) extended Ball's hydraulic approach to account for entrainment processes. They showed that the depth of buoyancy driven slope flows increases with down-slope distance by entrainment of ambient air into the flow. Furthermore, they conducted experiments to determine the entrainment physics, and developed parameterizations of entrainment coefficients which were subsequently used in many successful models of cold air drainage flows. Nappo and Rao (1987), however, point out that it has not been established if the parameterizations of entrainment physics obtained from laboratory data are applicable to slope flows under a variety of conditions.

Using Ellison and Turner's (1959) laboratory parameterizations, Manins and Sawford (1979) developed a model that calculated down-slope development of average flow values. Manins and Sawford's model predicted that entrainment was the dominant retarding mechanism in drainage flows, and was more important than surface stresses. Furthermore, they concluded that surface stresses may be negligible in the dynamical balance of fully developed slope flow, since the strong stratification near the surface essentially isolates the katabatic flow from surface influences. Further investigations into momentum balances of slope flows disagreed with Manins and Sawford's conclusion. Horst and Doran (1986) deduced that interfacial stress was only one quarter of surface stress. Kondo and Sato (1988) concluded that to obtain good models of drainage flows for a variety of conditions, neither surface nor interfacial stresses should be neglected.

Fitzjarrald (1986) suggested that similarity of slope flows to Prandtl's (1942) profiles depends on entrainment rates. For large entrainment rates, constant values of eddy diffusivity are not justified. Rao and Snodgrass (1981) developed a model of nonstationary drainage flows with height dependent eddy diffusivities to allow for greater mixing at the top of the flow. They also investigated the effect of some physical parameters such as slope angle, surface cooling, atmospheric stability and surface roughness on slope flows. However, their model did not include an explicit accounting of the effects of the interfacial entrainment of ambient air into the drainage flow.

Doran and Horst (1983) modified Prandtl's (1942) analysis to account for down-slope variation of the flow by approximating the advection terms in the governing equations by their slope-averaged values, and relating the eddy

diffusivities to the local turbulent kinetic energy. They conclude that the model employed by Manins and Sawford (1979) was inappropriate to describe their observations on Rattlesnake Mountain.

Nappo and Rao (1987) employed a numerical model to examine the effects of different slope angles and ambient stratification on drainage flows. Theirs was a time dependent, two dimensional model which allowed for down-slope evolution and entrainment of ambient air into the flow. Results of key flow parameters are presented as functions of slope angle, down-slope distance, and ambient stratification. They found that increasing ambient stratification affects the flow by reducing its depth, speed, and entrainment rate. Furthermore, they note that strongly stratified conditions lead to a regime which is essentially one dimensional, i.e. the flow is invariant in the down-slope direction, as in Prandtl's (1942) analysis. According to Nappo and Rao (1987), larger ambient stratification results in advection and entrainment of warmer ambient air, which acts to decrease the buoyancy deficit in the katabatic layer, the driving force for drainage flows. They also claim that the entrainment rate coefficient is not independent of stratification (contrary to Manins and Sawford) and that the rate of growth of the buoyancy deficit with down-slope distance decreases as the ambient stratification is increased.

1.3.1 Simple slopes and valley drainage flows

Numerous strategies for naming slope flows based on topography have been devised. In general, these have tried to distinguish between flows on simple slopes, flows on slopes draining into valleys, and flows in valleys.

Doran and Horst (1983) recognized that most slope flows in valleys are influenced by flow convergence from tributaries and side walls. Even Manins and Sawford (1979) conclude that their results were contaminated by flow convergence. With this in mind, Doran and Horst (1983) produced an observational study of slope flows over a nearly two dimensional ridge in Washington. They note that valleys tend to produce flows that are more topographically sheltered from external conditions than ridges, and significant contamination of drainage flows occurred at this site due to the sensitivity of simple slope flows to synoptic scale and mesoscale disturbances. Thus, the observations of flows over a simple slope observed at Rattlesnake Mountain in Doran and Horst (1983) and Horst and Doran (1986) were contaminated by strong cross slope winds.

Papadopoulos et al (1997) point out that most observationally and numerically studied flows are valley drainage flows or down-slope flows along valley side walls. These flows tend to be stronger than flows along a simple slope, and are not easily isolated from the larger scale valley flows into which they drain. Furthermore, Mahrt et al (2002) states that in terrain with a multiple length scales, drainage flows can occur simultaneously on a variety of scales.

1.3.2 Surface heat fluxes

Although numerous models of cold air drainage flows have been made, there seems to be no general agreement on the amount of surface cooling that is driving these flows. Historical detailed measurements of surface fluxes for cold air drainage flows do not exist, setting the stage for a variety of creative ways to prescribe lower boundary conditions in numerical models.

In general, this has been accomplished in three ways. Models such as McNider and Pielke (1984), and Yamada (1981) have utilized a full radiation and surface physics package to describe surface heat fluxes. Other models such as Davies et al (1995) have prescribed a temperature difference between the surface and air just above the surface. Manins and Sawford (1979), and Bader and McKee (1983) use a constant heat flux as their lower boundary condition. Finally, Nappo and Rao (1987) decreased the surface temperature until a specified ground temperature deficit was achieved and then held the surface heat flux from then on. However, none of these lower boundary conditions seem to be justified from observational data. In recognizing this, Doran, Horst and Whiteman (1990) point out that

a proper description of valley flow dynamics requires a detailed surface energy budget description to properly determine the lower boundary condition for the thermodynamic equation. Assumptions of constant cooling rates, constant temperature deficits, or sensible heat fluxes independent of down-slope distance are not supported by the data.

1.3.3 TKE

A great deal of effort has been put into observing and modeling turbulent kinetic energy budgets over flat ground. In that the structure of nocturnal boundary layers over flat ground is significantly different than those over slopes, it is still not known if boundary layer parameterizations formulated from observational studies over flat ground are applicable to models of slope flows.

Horst and Doran (1988) studied the turbulence characteristics of slope flows on Rattlesnake Mountain. They found that the local turbulent kinetic energy (TKE) balance is largely a balance between shear generation and viscous dissipation, in that slope flows are stably stratified and do not support buoyant generation of TKE. Furthermore, they point out that at the height of the jet maximum, shear production is predicted to be zero, and lower order closures would predict that turbulence above the low level wind maximum can become decoupled from surface influences. Hence, surface scaling of turbulence parameters is not justified for katabatic flows.

Denby (1999) provides a second order model of turbulence in katabatic flows. He presents TKE budgets for drainage flows calculated using two different closures (a diagnostic buoyant length scale and a prognostic dissipation equation) and compares his results to those of a 1.5 order TKE model. He also points out that the assumptions that are used in M-O theory predict a decoupling of the katabatic layer above and below the wind maximum, unless ad hoc assumptions about the minimum mixing length are employed at the height of the jet maximum. In higher order models, however, the turbulent transport term can become important at the

height of the wind maximum, as well as above this height where wind shear can become small.

Skyllingstad (2003) provides a large eddy simulation (LES) of a katabatic flow and describes in detail the TKE budget of the flow. He states that for steeper slopes, down-slope acceleration from buoyancy forcing is balanced by mixing and advection. Mixing is important near the surface, where velocity gradients are highest, while advection becomes more important above the jet maximum. Most TKE is generated through shear near the surface and just above the down-slope jet. Although the TKE is primarily destroyed by dissipation, the buoyancy term is still important. He points out that mesoscale models of drainage flows must have sufficient vertical resolution to produce a good model of katabatic flows. If the vertical structure of the flow is not resolved, then the turbulent exchanges at the top and bottom of the flow are surely inaccurate. He also stresses the importance of turbulent exchange above and below the jet in determining the depth and strength of the flow. And finally, he states that further research is needed to determine how models behave when terrain features are not properly resolved, as in the case for most operational models.

1.3.4 Changing slope angles

The effect of changing slope angles on a simple slope flow is only briefly mentioned in the literature. As most slopes tend to be steeper near the mountain or ridge tops than near the foot of the slope, we might expect that systematic differences would be evident in the literature on observational campaigns of slope

flows. This was first observed in Doran and Horst's (1983) study of drainage flows on Rattlesnake Mountain. They noted that the lowermost tower at this site had a smaller slope angle than towers further upslope. The authors were using a simple one dimensional model to simulate the katabatic flows on the upper steeper portion of this ridge. Their model could not account for changes in slope angle, and discrepancies between observed and simulated values at the lowermost tower were attributed to a slope angle that decreased with down-slope distance. At the lower tower, Horst and Doran's (1986) predictions of flow parameters based on an equivalent length from the tower to the top of the ridge met with moderate success. They conclude that their one dimensional model was not sophisticated enough to simulate katabatic flows over a slope with changing slope angle.

Many authors make no mention of a change in slope angle in their domain. For example, a mesoscale model of the diurnal cycle over a slope with changing slope angle was made by Bader et al (1987). Their slope included an upper portion with 8 % grade, followed by a longer portion with 1% grade. The authors, however, do not note the effects of the change in slope angle on the katabatic flow.

Papadopoulos et al (1997) also make a brief mention of the effect of changing slope angle in noting that the slope angle at observational towers lower down their slope are not as steep as those higher upslope. They state that this change in slope angle can account for discrepancies between observations and modeled down-slope evolution of the flow. In particular, Nappo and Rao (1987) predicted a linear relationship between buoyancy deficit length scale and down-slope distance for a near neutral stability and constant slope angle.

Monti et al (2002) state that discontinuities in slope angle may lead to higher elevation steeper slope flows overrunning existing katabatic flows on gentler slopes of lower elevation. They point out that most slope flows are supercritical, that is, information may not be passed upstream, only in the downstream direction. Hence the flow responds to a change in slope angle by changing its depth by way of a hydraulic jump, since larger slope angles support larger down-slope velocities.

1.4 Description of the current study

This thesis is a modeling study of the development and structure of katabatic flows and their relation to parameters such as surface heat fluxes, ambient stratification, slope angle and slope profile.

Chapter two begins with an introduction to the models used in this study. This is followed by a comparison between an LES and a mesoscale model of katabatic flows in section 2.2. The purpose of this comparison is to verify the subgrid scale parameterization of the mesoscale model.

The following sections of chapter two represent a sensitivity study of slope flows to various factors. This study will focus on the effect of surface heat fluxes (section 2.3), slope angle (section 2.4) and ambient stratification (section 2.5) on simple slope flows. In the past, surface heat fluxes have not been adequately measured in observational studies of katabatic flows. In that surface heat fluxes are driving the flow, an account of their effect is crucial to our understanding of on slope flows. The effect of ambient stratification on slope flow will be explored to

determine if slope flows essentially become invariant in the down-slope direction under strong ambient stratifications as predicted by Nappo and Rao (1987). To gain insight into the relationships between combined and simple slope flows, I will also study the effect on slope angle on simple slope flows. Throughout this chapter, the concept of katabatic efficiency will be applied to better understand energy conversion in katabatic flows.

Chapter three is a comparison of modeled flows over simple and combined slopes of varying upper slope angle. Section 3.1 examines the differences between simple and combined slope flows, while section 3.2 studies the effect of the upper slope angle on drainage flows over the lower portion of a combined slope. Results from this chapter will help to tailor numerical drainage flow predictions in areas of inadequate terrain resolution, and produce parameterizations of subgrid scale terrain features in models of katabatic flows in areas of complex terrain.

2. Study of Simple Slopes

2.1 Model introduction

Simulations of cold air drainage flows were run using the Advanced Regional Prediction System (ARPS) and the LES model to make a comparison between the two models and check the subgrid parameterizations of the ARPS model. The LES model is better able to resolve smaller scale features of the flow, and can directly model the largest energy containing eddies, whereas in the ARPS model, all turbulence is parameterized. By using the LES model we can gain more accurate information about the scale processes in the flow and check the turbulence parameterizations of the ARPS model.

2.1.1 ARPS

ARPS was chosen for the mesoscale model runs. ARPS is a three dimensional, nonhydrostatic, compressible model which uses terrain-following coordinates (Xue et al, 2000). The model domain is shown in figure 2.1. The domain is 32 km by 0.6 km by 4 km in the X, Y and Z directions respectively. Grid size is 100 m by 100 m in the horizontal with 320 grid points in the X direction and 6 grid points in the Y direction. The vertical coordinate is terrain-following with a grid size that is stretched using a hyperbolic tangent function to allow for a very fine grid size of 5 m near the surface where resolution is critical. The domain is 4 km high with 80 levels in the vertical. An analytic two dimensional triangular mountain profile was prescribed with the slopes in the x-

direction. The mountain is uniform in the cross slope y-direction, covering the entire domain. Boundary conditions in the y direction are periodic. In the x direction the boundary conditions are open (radiation). The top and bottom boundary conditions are rigid. The model is initialized at rest with an isothermal atmosphere.

Constant cooling rates are applied at the bottom boundary to drive the flow. In order to prescribe the proper surface cooling to drive the flow, radiation physics are turned off, and the surface physics are set to constant surface drag coefficients. The soil type is sandy loam, the vegetation type is cultivation and the roughness length is 0.01 m. In addition, moisture and microphysics processes are turned off for the simulations. The model is run for one hour by which time the drainage flow has come to steady state.

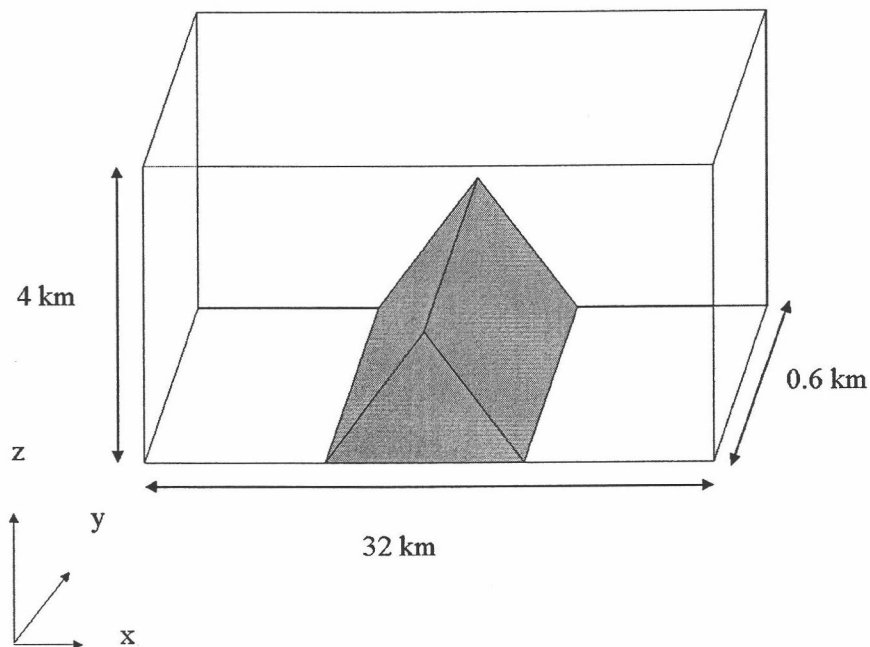


Figure 2.1: Three dimensional view of ARPS model domain and mountain.

The subgrid model used is 1.5 order TKE closure after Moeng (1984). In this scheme the eddy diffusivity is related to a mixing length l , and the turbulent kinetic energy, e ,

$$K_{mj} = 0.1 e^{1/2} l_j$$

For the simulations in this study the horizontal grid spacing is much larger than that in the vertical, so the horizontal mixing length, l_h is set to Δ_h , the grid spacing in the horizontal direction. The vertical mixing length, l_v , for the stably stratified case, is defined as the minimum of the vertical grid spacing, Δ_v and l_s .

$$l_v = \min(\Delta_v, l_s) ,$$

where l_s is defined as a relationship between the turbulent kinetic energy and the Brunt-Vaisaila frequency, N^2 , after Hassid and Galperin (1983).

$$l_s = 0.53 \sqrt{\frac{e}{N^2}} ,$$

where N^2 is the Brunt-Vaisalia frequency, which is a relationship between the potential temperature gradient in the vertical direction, gravity, g , and a reference potential temperature, θ_0 .

$$N^2 = \frac{g}{\theta_0} \frac{d\theta_{ambient}}{dz}$$

2.1.2 LES

An LES model is used to investigate further the smaller scale structure of slope flows. The LES model is a modified version of that described in Skillingstad et al (2003). This model is based on the equations of Deardorff (1980) with a subgrid turbulence closure provided by the filtered structure-function approach of Ducros et al.(1996).

The model domain, shown in figure 2.2, is rotated so that the coordinates are terrain-following. Boundary conditions in the cross slope direction are periodic. A closed boundary condition is applied in the upslope direction, and an open boundary condition is applied in the down-slope direction using a simple radiative scheme following Durran (1999). For the top boundary condition a wave absorbing layer is applied following Klemp and Lilly (1978). Slope-normal velocities at the model top are set using the area-averaged down-slope outflow velocity to allow for conservation of mass.

The domain size is 7680 m long, 150 m wide and 37.5 m deep. The grid spacing is 3.0 m and there are 2560, 200, and 50 points in the down-slope, cross slope and normal directions respectively. Constant cooling rates of 30 W/m^2 are imposed at the bottom boundary surface to drive the flow. The model is initialized at rest with an isothermal atmosphere and allowed to come to steady state.

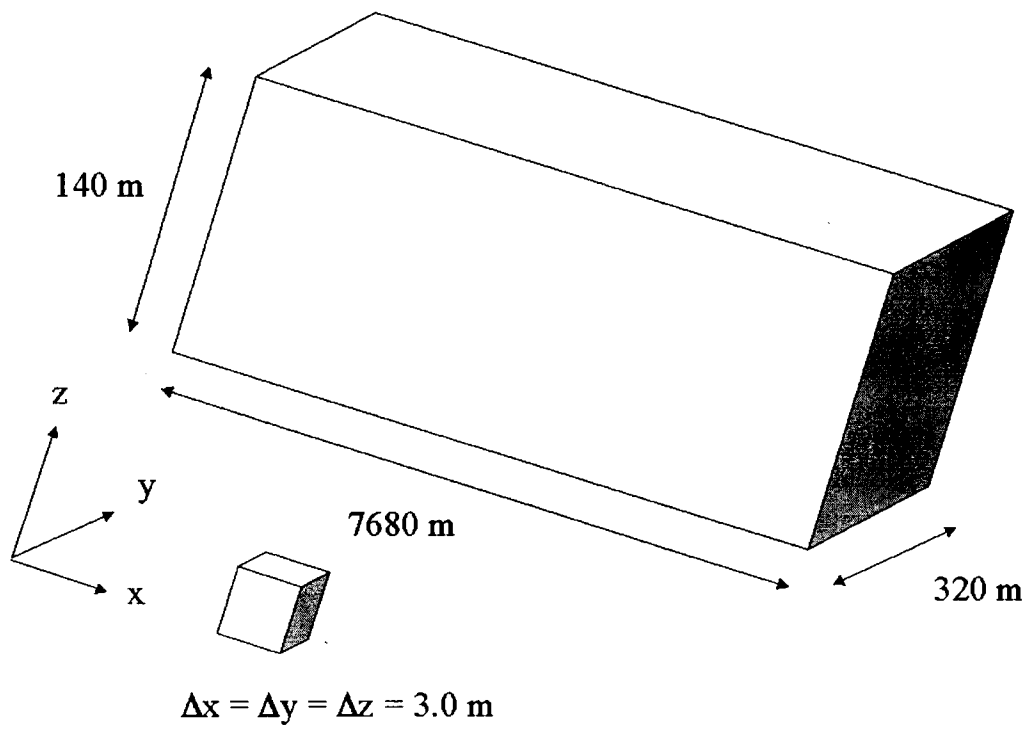


Figure 2.2: Three dimensional view of LES model domain.

2.2 Comparison between ARPS and LES results

Cold air drainage simulations were run with the ARPS and LES model. The model runs are described in detail in section 2.1.1, and an X-Z cross section of the ARPS domain is shown in figure 2.3. The LES model runs are described in detail in section 2.1.2. The slope angle, α is 14 degrees. Surface fluxes are applied uniformly along the slope at 30 W/m^2 of cooling to drive the flow. Both models are initialized at rest, with an isothermal atmosphere, and allowed to run until the flow comes to steady state.

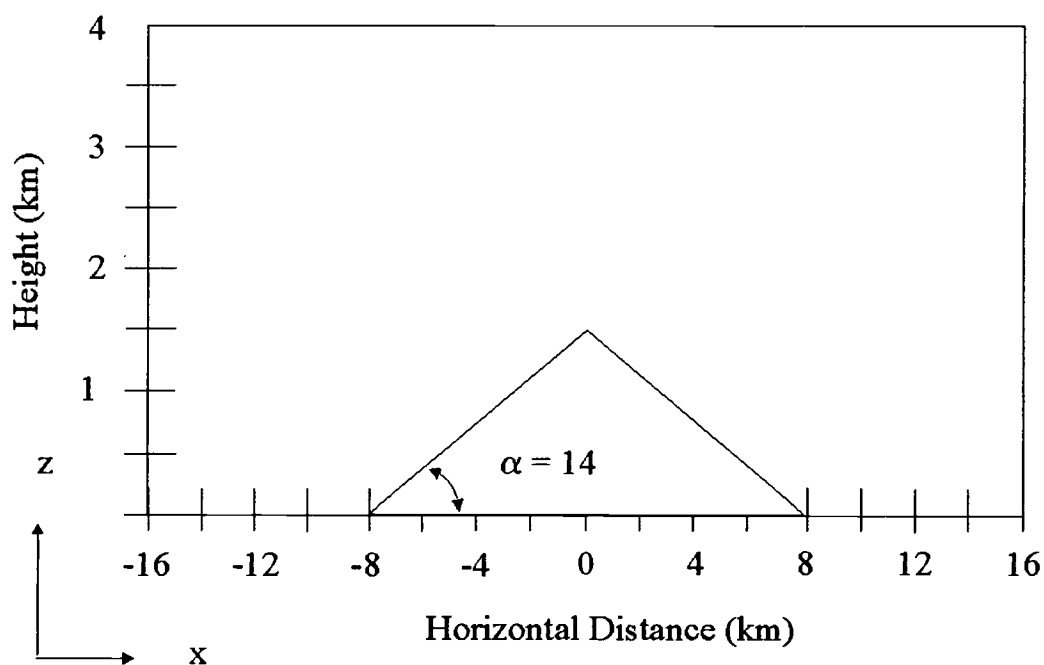
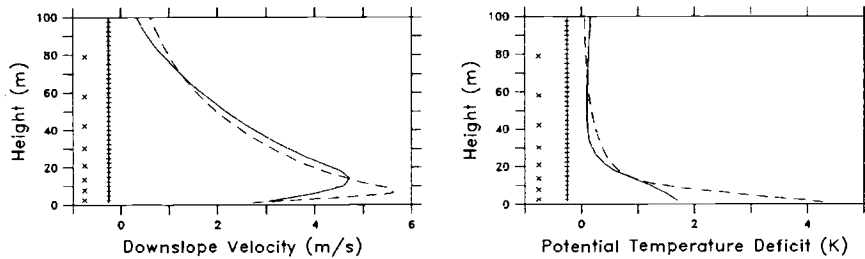


Figure 2.3: X-Z cross section of ARPS model domain for $\alpha = 14$ degrees.

Results of the simulations reveal some differences between the two models. This is evident in the velocity profiles 5.9 km down the slope, figure 2.4. Also

shown in this plot are the vertical grid points used in the LES and ARPS model. The LES model produces a jet that is lower and greater in magnitude than that of the ARPS model. In this figure it can also be seen that the LES model also cools more near the surface than the ARPS model, as indicated by the plot of potential temperature deficit versus height on the right. Potential temperature deficit is defined as the temperature of the ambient air minus the temperature of the air in the katabatic flow, at the same level. Part of this could also be due to the first grid point in the ARPS model being 5 m above the surface, significantly higher than that of the LES model.



Figures 2.4: Velocity profile (left) and potential temperature deficit profile (right) and of LES (- -) and ARPS (-) model at a location 5.9 km down-slope. Also shown are the vertical grid points for the LES (+) and the ARPS (x) model.

Katabatic flows are driven by buoyancy forcing, and retarded by advection, vertical mixing, and drag. The relative magnitude of the individual terms in this three-way momentum balance varies with height. The mean momentum equation in the down-slope direction may be written as in Mahrt (1982).

$$\begin{array}{cccccc}
 \frac{\partial u}{\partial t} & + & u \frac{\partial u}{\partial s} & + & w \frac{\partial u}{\partial n} & = & \sin \alpha \, g \frac{\theta}{\theta_0} & - & \cos \alpha \, g \frac{\partial(\bar{\theta}h)}{\partial s} & - & \frac{\partial(\overline{u'w'})}{\partial n} \\
 \text{I} & & \text{II} & & \text{III} & & \text{IV} & & \text{V}
 \end{array}$$

Where the pressure gradient term has been rewritten so that

$$\frac{1}{\rho_o} \frac{\partial p}{\partial x} = \cos \alpha \frac{g}{\theta_o} \frac{\partial(\bar{\theta}h)}{\partial x},$$

θ_o is a reference potential temperature, and the average potential temperature is defined as

$$\bar{\theta} = \frac{1}{h_o} \int_0^h \theta dz$$

In the momentum equation we have neglected the coriolis term, and rewritten the pressure term by assuming hydrostatic balance in the slope-normal direction. Also, using K-theory, we can express the turbulent flux divergence as

$$\frac{\partial}{\partial n} \overline{u'w'} = \frac{\partial}{\partial n} K_m \frac{\partial u}{\partial n}$$

Term I in the momentum equation is time rate of change of momentum. All flows in the present study are stationary, that is, they have achieved steady state, so the storage term will be neglected. Term II is the sum of the down-slope and slope-normal advection terms. This term represents the horizontal advection of lower momentum from up-slope. Term III is the katabatic acceleration or the buoyancy term. This term is the primary driving force for the flow. The thermal wind, term IV, represents a retarding factor due the down-slope increase in stability, and is much smaller than the buoyancy term for the flows in this study. Term V represents the turbulent flux divergence. This term acts to retard the flow by mixing. The surface drag is included in this term as a boundary condition.

Setting the storage term to zero, using K-theory and rearranging, we can rewrite the down-slope momentum equation as

$$\sin \alpha \, g \frac{\theta}{\theta_0} - \cos \alpha \frac{g}{\theta_0} \frac{\partial(\bar{\theta}h)}{\partial s} = \frac{\partial}{\partial n} K_m \frac{\partial u}{\partial n} - \left(u \frac{\partial u}{\partial s} + w \frac{\partial u}{\partial n} \right)$$

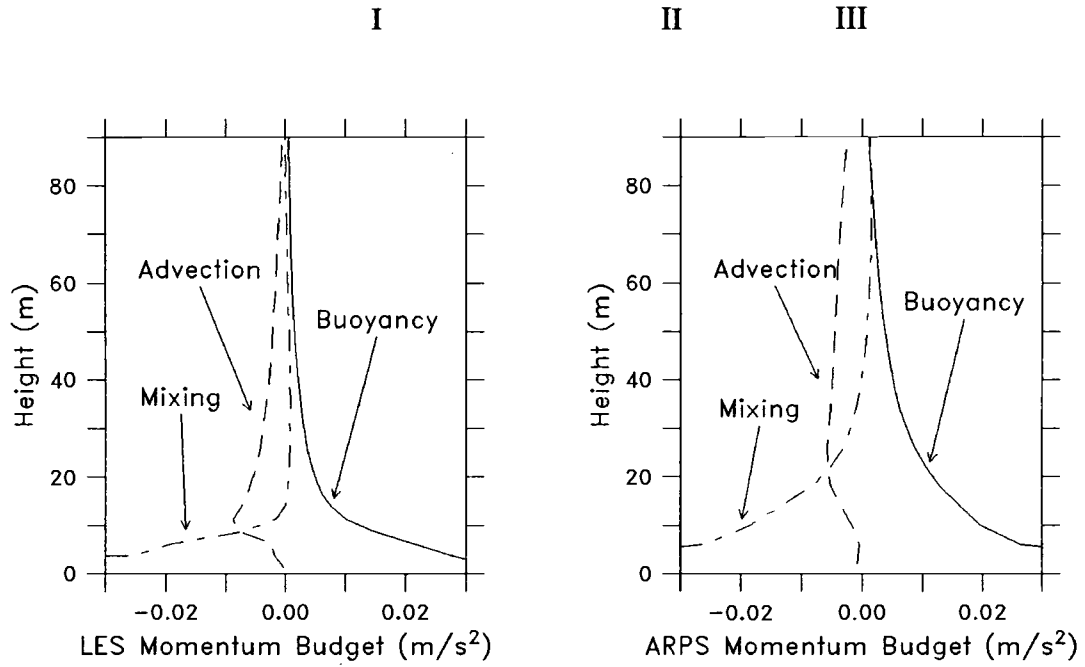


Figure 2.5: Momentum budget for LES (left) and ARPS (right) model at a location 5.9 km down-slope.

A comparison of the momentum budgets 5.9 km down-slope as a function of height of the LES and ARPS model is shown in figure 2.5. There is good agreement between the two momentum budgets. Near the surface, the buoyancy force, I, is large in magnitude, and is driving the flow downhill, while vertical mixing and drag, II, acts to slow down the flow. Near the surface, the buoyancy

term is greater in magnitude in the LES model than in the ARPS model, due to cooler near surface temperatures in the LES model. While drag is the dominant retarding mechanism near the surface, away from the slope, advection, term III, of becomes more important. In the LES momentum budget, advection becomes more important than mixing and drag at around 10 m, near the height of the jet. In the ARPS model advection becomes more important than mixing and drag at 25 m, just above the height of the jet. Also, the mixing and drag term is larger in the ARPS model than the LES from the jet height up.

In this case, the momentum equation represents a three-way balance between advection, buoyancy, and mixing. As here, when the thermal wind, coriolis, and storage term are small relative to the buoyancy term in the momentum budget, the flow can be classified as a shooting flow, according to Mahrt (1982).

Turbulence is the critical factor in determining the exchange of heat and momentum between the surface and the ambient air in katabatic flows. The turbulent kinetic energy as a function of height at a point 5.9 km down slope is shown in figure 2.6. Qualitatively, the agreement between the two is very good. A minimum of TKE near the jet height is picked up by both the ARPS and LES model. This minimum of TKE with respect to height is due to the absence of local velocity gradients in the flow at the jet height. Since velocity gradients produce TKE thru shear, we find lower TKE in areas of lower velocity gradients. Both TKE profiles have the same structure, but the ARPS model TKE is higher in magnitude than the LES model. Since the models have similar velocity profiles, this indicates that the subgrid parameterization in ARPS is overestimating the production of TKE.

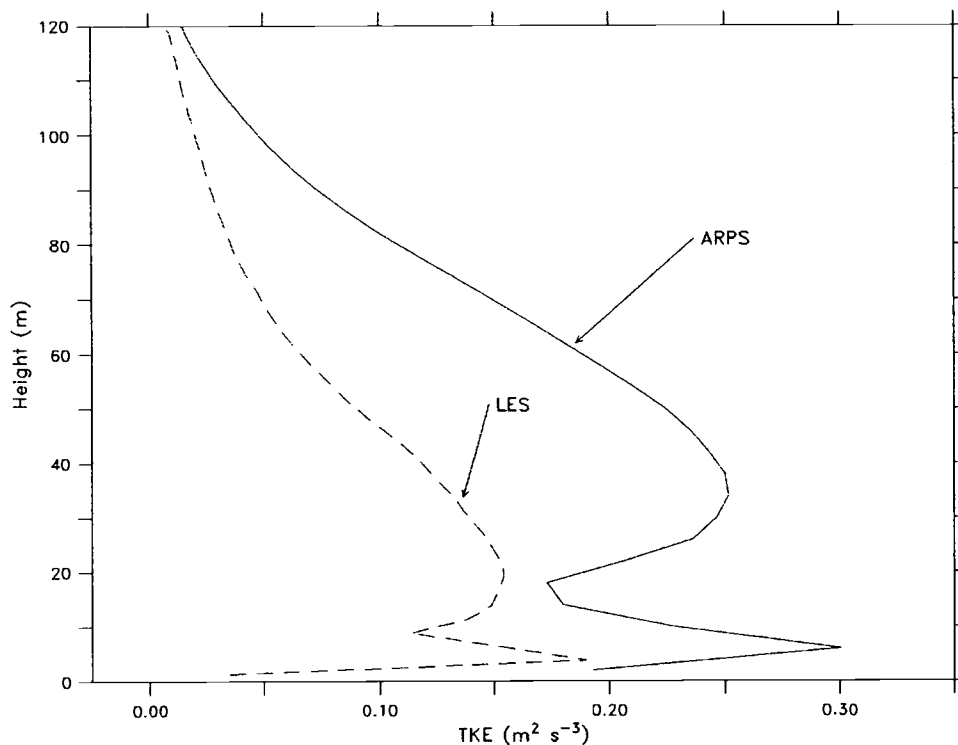


Figure 2.6: TKE as a function of height for LES and ARPS model at a location 5.9km down-slope.

This can be verified by examining the TKE budgets of both models. The TKE budgets for both models agree well with each other, and are presented as function of height 5.9 km down-slope is shown in figure 2.7. The TKE equation is written below.

$$\frac{\partial e}{\partial t} + U_j \frac{\partial e}{\partial x_j} = \frac{g}{\theta_0} \left(\overline{u_i' \theta_i'} \right) - \overline{u_i' u_j'} \frac{\partial U_i}{\partial x_j} - \frac{\partial \left(\overline{u_j' e} \right)}{\partial x_j} - \frac{1}{\rho} \frac{\partial \left(\overline{u_i' p'} \right)}{\partial x_i} - \epsilon$$

I II III IV V VI VII

Where the shear production term, term IV, is parameterized as follows.

$$\overline{u'w'} = K_m \frac{\partial U}{\partial n}$$

And the pressure and turbulent transport terms, terms V and VI, are parameterized as in Deardorff (1980).

$$\frac{\partial}{\partial x_i} \left[u_i' \left(e + \frac{p'}{\rho} \right) \right] = \frac{\partial}{\partial x_i} \left(2K_m \frac{\partial e}{\partial x_i} \right)$$

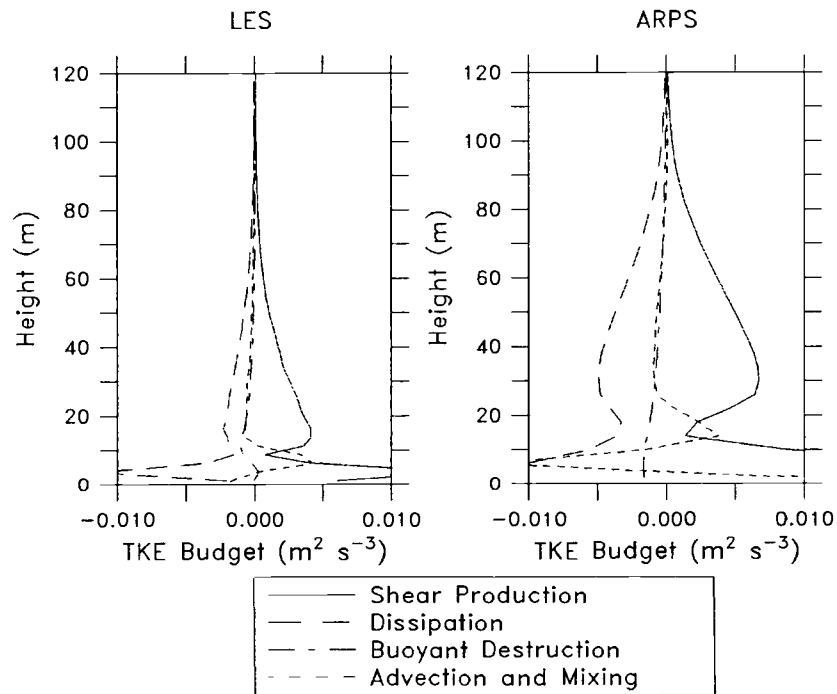


Figure 2.7: TKE budget as a function of height for the LES and ARPS model at a location 5.9 km down-slope.

In stably stratified flows, the primary source of TKE is the shear production term (IV). Velocity gradients are highest near the surface and just above and below the jet height, hence shear production is highest in these areas. Likewise, because TKE production by shear tends to generate relatively small eddies, dissipation, (VII), is also highest in these areas. Since velocity gradients in the slope-normal direction generate turbulence through shear production, we find that at the jet height, where velocity gradients are zero, there is a local minimum of shear production of TKE. The overproduction of TKE by shear in the ARPS model, could be due to a number of factors, including the turbulent length scale parameterization, and grid spacing used in the model. Due to the stably stratified nature of katabatic flows, there is no buoyant generation of TKE in katabatic flow, and the stable stratification acts to suppress the turbulence. The buoyancy term (III), is always negative, and is greatest in magnitude where stratification is highest, near the surface. The final term in the TKE budget is the advection and mixing term. This term includes the advection of TKE by the mean flow (II), and turbulent and pressure transport of TKE (V and VI). This term acts to redistribute turbulent energy from areas of high TKE to areas of low TKE. In particular, this term is positive near the jet height and becomes strongly negative just below the jet height. So this term acts to transport TKE from areas of high TKE (where it is produced), to areas of low TKE (near the height of the jet).

2.3 The effect of surface heat fluxes

Simulations were run using the ARPS model to determine the effect of surface heat fluxes on drainage flows. The model runs are described in detail in section 2.1.1, and an X-Z cross section of the domain is shown in figure 2.8. The slope angle, α was 6.1 degrees. Surface fluxes were applied uniformly along the slope at 20, 30, 40, 50, 60, 70, 80, 90 and 100 W/m² of cooling to drive the flow. The model was initialized at rest, with an isothermal atmosphere, and allowed to run for one hour of model time, by which time the flow had come to steady state.

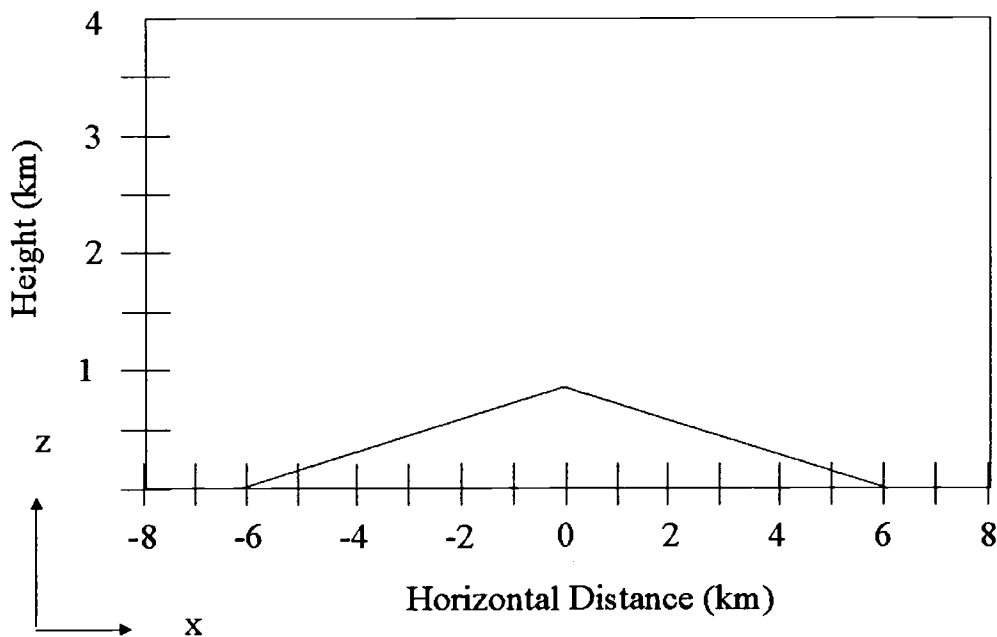


Figure 2.8: X-Z cross section of ARPS modeling domain for surface heat flux and ambient stratification study runs.

Results of the simulations show that surface cooling strongly affects both velocity and temperature deficit fields. As the surface cooling is increased, the flow deepens and the down-slope velocity increases in magnitude. Figure 2.9 shows an X-Z cross section of the down-slope potential temperature evolution of the flow for surface cooling of 20, 50 and 100 W/m². Figure 2.10 shows an X-Z cross section of down-slope velocity contours of the flow for surface cooling of 20, 50 and 100 W/m². Figure 2.11 shows velocity profiles for these runs as a function of height at a location 6.5 km down-slope, near the foot of the slope. The height of the jet, z_{\max} , does not increase with increase surface heat fluxes, but the magnitude of the down-slope velocity jet increases from 3.6 m/s for the 20 W/m² case, to 6.4 m/s for the 100 W/m² case. The buoyancy deficit profile 6.5 km down the slope is shown in figure 2.12. As surface cooling increases from 20 W/m² to 100 W/m², the near surface buoyancy deficit increases in magnitude from 4 K to 12 K.

A look at the momentum budget as surface fluxes increase reveals that buoyancy, advection, and mixing and drag terms in the momentum budget all behave in a similar manner. This can be seen in figure 2.13, a plot of these terms summed up over the first 50 m from the slope surface to obtain the relative contribution of each term to the momentum budget of the flow as a function of down-slope distance. Hereafter, the vertically integrated momentum budget will be referred to as the total momentum budget, and unless otherwise stated, will represent a summation in the vertical direction from the surface to 50 m from the surface.

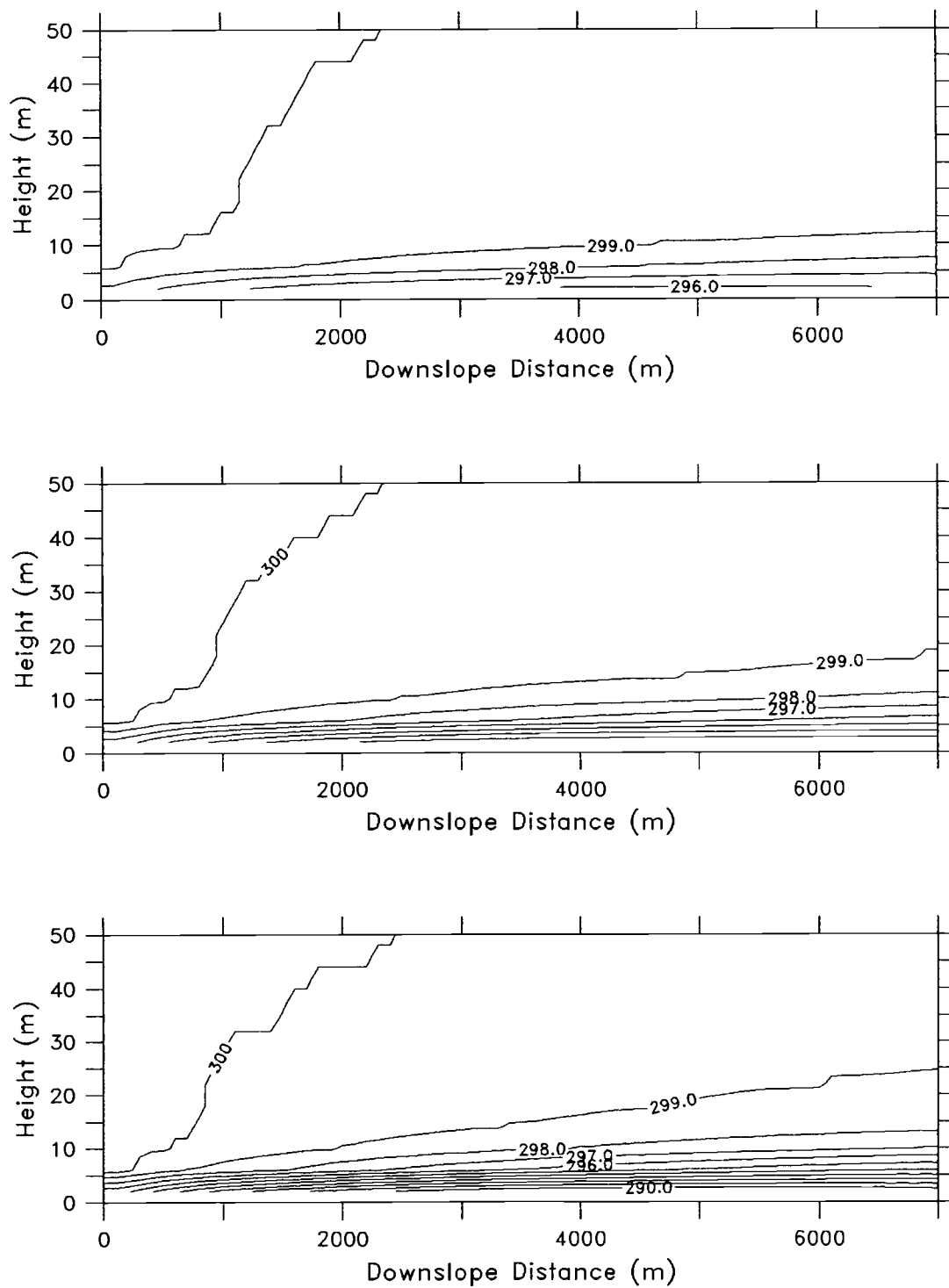


Figure 2.9: X-Z cross section of the down-slope evolution of potential temperature fields for $Q_0 = 20$ (top), 50 (middle), and 100 W/m^2 (bottom).

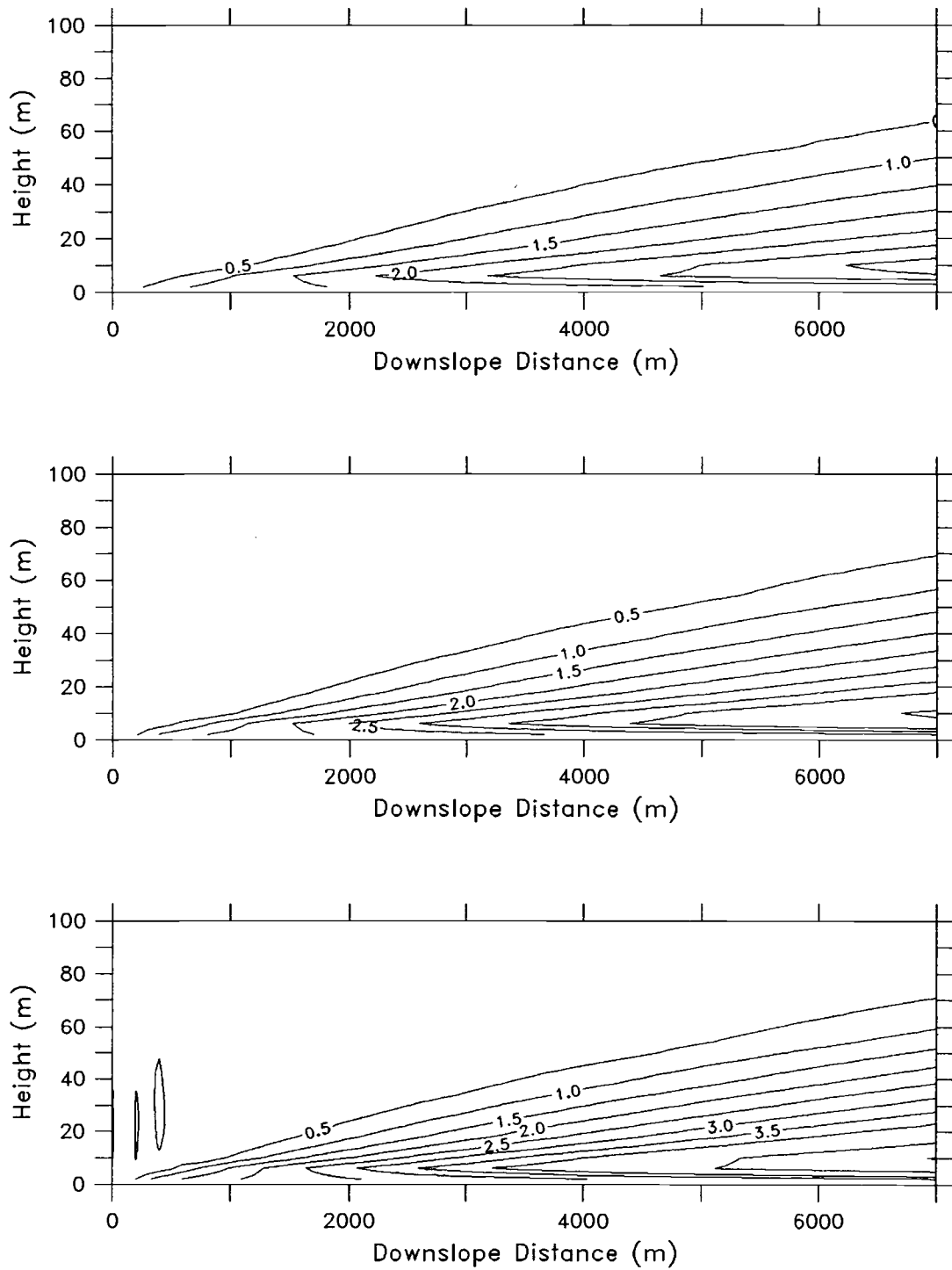


Figure 2.10: X-Z cross section of the down-slope evolution of downslope velocity fields for $Q_0 = 20$ (top), 50 (middle), and 100 W/m² (bottom).

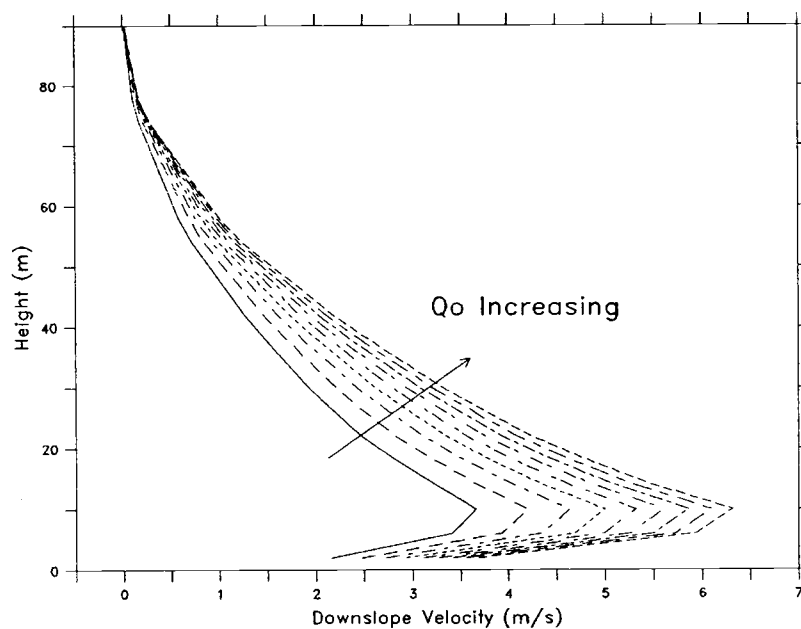


Figure 2.11: Velocity profiles as a function of height for surface heat flux runs at 6.5 km down-slope.

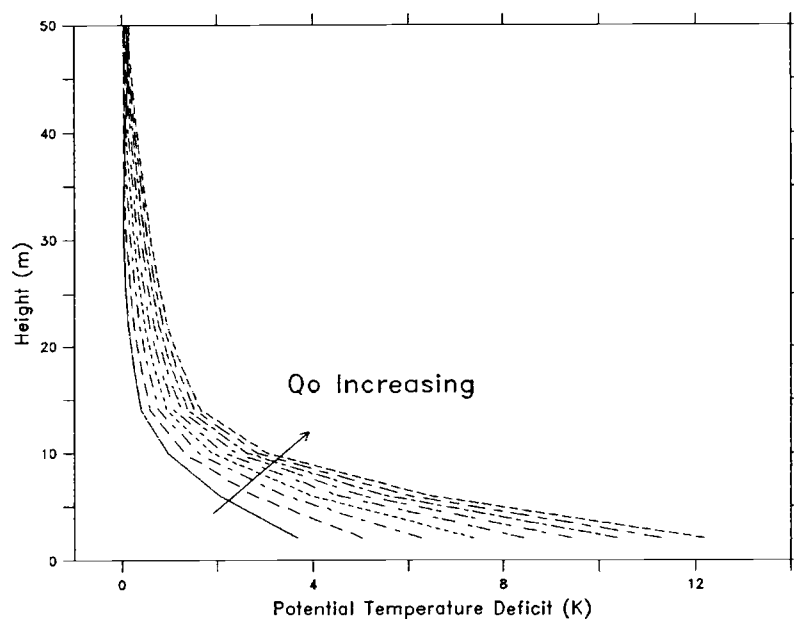


Figure 2.12: Buoyancy deficit profiles as a function of height for surface heat flux runs at 6.5 km down-slope.

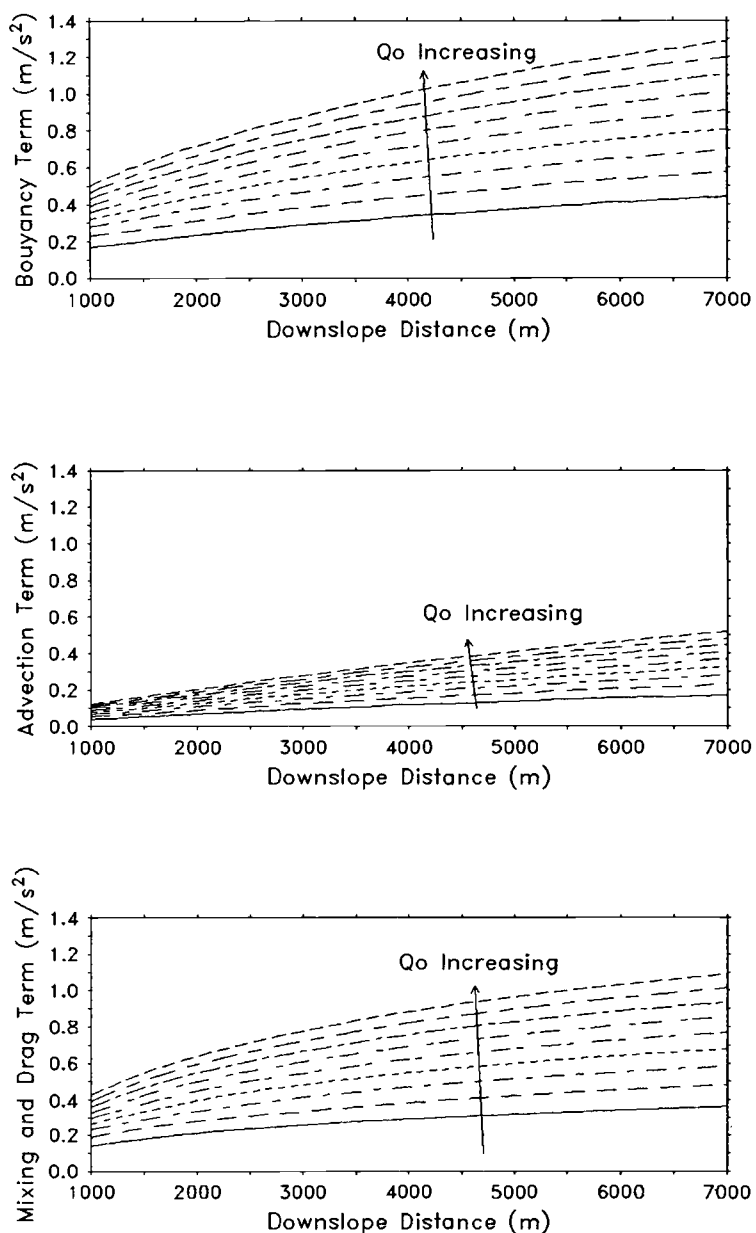


Figure 2.13: Buoyancy (top), advection (middle), and mixing and drag (bottom) terms in the vertically integrated momentum budget as a function of down-slope distance for surface heat flux runs.

More insight into the effect of surface heat fluxes on the momentum budget of slope flows is gained by looking at the buoyancy normalized momentum budget. Here, the momentum budget is normalized by the buoyancy term, to create a nondimensional momentum budget.

$$1 = \frac{1}{B} \frac{\partial}{\partial n} K_m \frac{\partial u}{\partial n} - \frac{1}{B} \left(u \frac{\partial u}{\partial s} + w \frac{\partial u}{\partial n} \right)$$

Where the buoyancy term, B , is defined as follows.

$$B = \sin \alpha \, g \frac{\theta}{\theta_0} - \cos \alpha \frac{g}{\theta_0} \frac{\partial(\bar{\theta}h)}{\partial s}$$

This nondimensional momentum budget represents a balance between mixing and drag, the first term on the right hand side of the nondimensional momentum equation, and advection, the second term on the right hand side of the nondimensional momentum equation.

A plot of the buoyancy normalized total momentum budget is presented in figure 2.14. In the top two plots, total advection and mixing and drag for all runs have been normalized by the total buoyancy term, while the lower plot shows the total advection to mixing and drag ratio for all runs. As can be seen in this figure, the momentum budgets of the slope flows exhibit a self-similar behavior with regards to surface heat fluxes. That is, the advection to buoyancy (top), mixing and drag to buoyancy (middle), and advection to mixing and drag ratios (bottom) are all constant regardless of the amount of surface cooling that is applied. The flow is

partitioning its buoyant energy in a similar manner regardless of the magnitude of surface heat fluxes. It should also be noted that advection is less in magnitude than mixing and drag near the top of the slope, while downslope, advection is greater in magnitude than mixing and drag. So the relative magnitude of the terms in the normalized momentum budget vary with downslope distance.

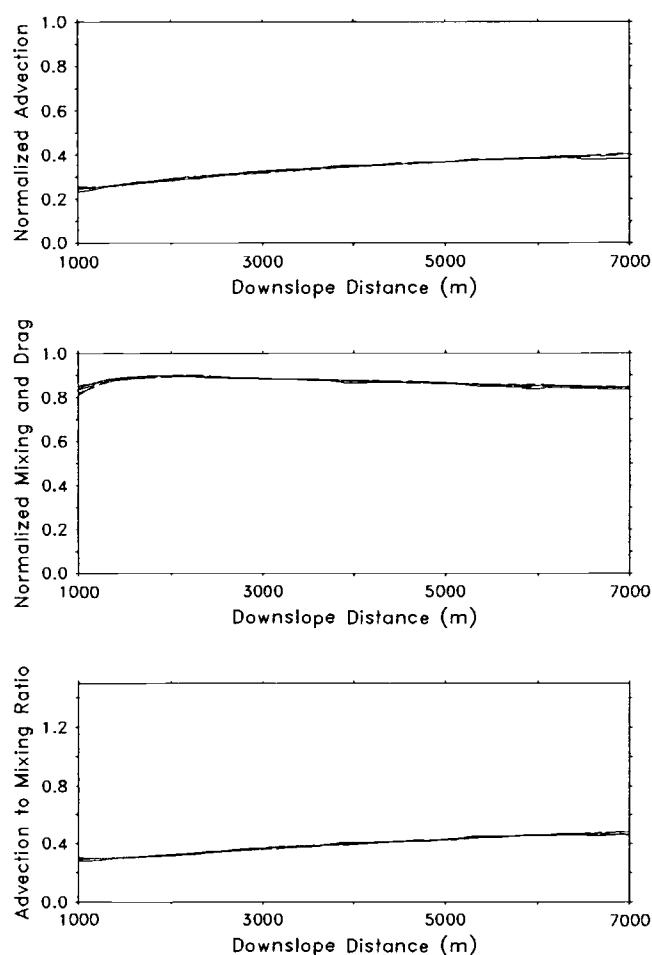


Figure 2.14: Buoyancy normalized momentum budget (top two) and advection to mixing ratio as a function of down-slope distance for surface cooling runs.

Discussions of flow strength are better done in terms of bulk parameters rather than vertical profiles of velocity and temperature. Thus we define a velocity strength scale, UH , and a buoyancy strength scale, $\Delta'H'$, based on velocity and potential temperature deficit profiles after Manins and Sawford (1979) and Doran and Horst (1983).

$$UH = \int u \, dz$$

$$\Delta'H' = \int \frac{gd}{\theta_0} \, dz$$

where u is down-slope velocity, z is in the vertical direction, and the buoyancy deficit, d , is defined as the difference between the potential temperature of the katabatic flow, and the potential temperature of the ambient air at the same height but away from the surface of the slope.

$$d = \theta_{katabatic} - \theta_{ambient}$$

In practice these integrals extend from the slope surface up to a point where the velocity and potential temperature deficit become arbitrarily close to zero.

Velocity and buoyancy depth scales increase with surface heat fluxes since down-slope velocity and potential temperature deficits also grow with increasing surface fluxes. Plots of buoyancy and velocity strength scales versus down-slope distance as a function of surface heat fluxes are shown in figures 2.15 and 2.16 respectively.

It can be seen from these figures that the buoyancy and velocity strength scales are significantly affected by surface heat fluxes. Parameterizations of the strength scales have been developed to account for surface heat fluxes. These parameterizations have the form

$$UH = C_u (Q_0) s^m$$

$$\Delta'H' = C_b (Q_0) s^n$$

Where C_u and C_b are constants that depends on various physical parameters of the flow and s is the along slope distance. For the buoyancy strength scale, $n = 1.4$, while for the velocity strength scale, $m = 2.2$. For the cases of constant slope angle, C_b and C_u , the coefficients for buoyancy and velocity strength scales, depend on surface heating in a nearly linear fashion. Plots of the coefficient of velocity strength scale and buoyancy strength scales are shown in figures 2.17 and 2.18, respectively. A table of the tabulated variation of velocity and buoyancy strength scale coefficients with surface heat fluxes is listed below.

For surface heat fluxes, Q_0 , ranging from 20 to 100 W/m², parameterizations for velocity and buoyancy strength scale coefficients can be made as a linear function of surface heat fluxes using the following relations

$$C_u = 2.7 * 10^{-5} + 3.375 * 10^{-7} * (Q_0 - 20)$$

$$C_b = 2.8 * 10^{-4} + 1.525 * 10^{-5} * (Q_0 - 20)$$

Q_0 (W/m^2)	$C_b * 10^{-4}$ ($\text{m}^{-0.2} \text{s}^{-1}$)	$C_u * 10^{-5}$ ($\text{m}^{0.8} \text{s}^{-1}$)
20	2.8	2.6
30	4.4	3.0
40	6.0	3.5
50	7.6	3.8
60	9.2	4.1
70	11.0	4.5
80	12.0	4.8
90	14.0	5.0
100	15.0	5.3

Table 2.1: The variation of velocity and buoyancy strength scale coefficients with surface heat fluxes

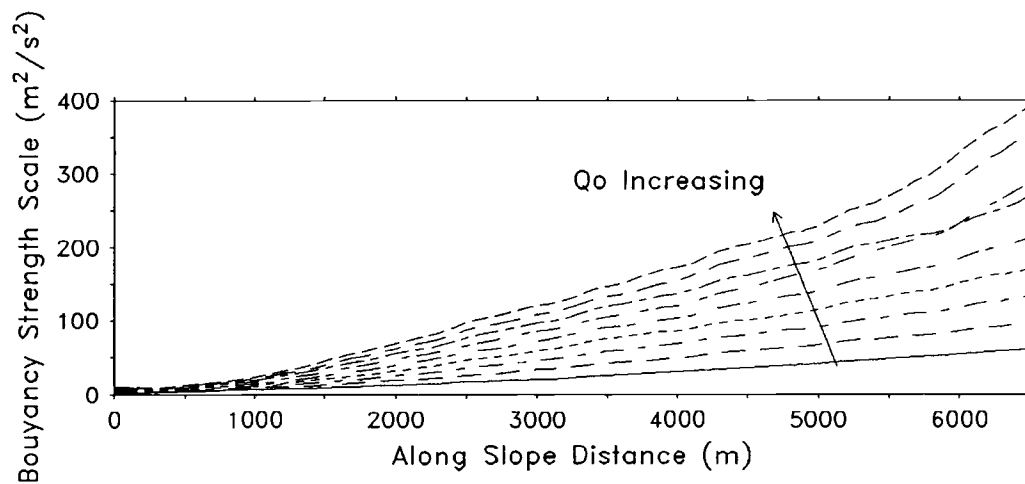


Figure 2.15: Buoyancy strength scale versus downslope distance for surface heat flux runs.

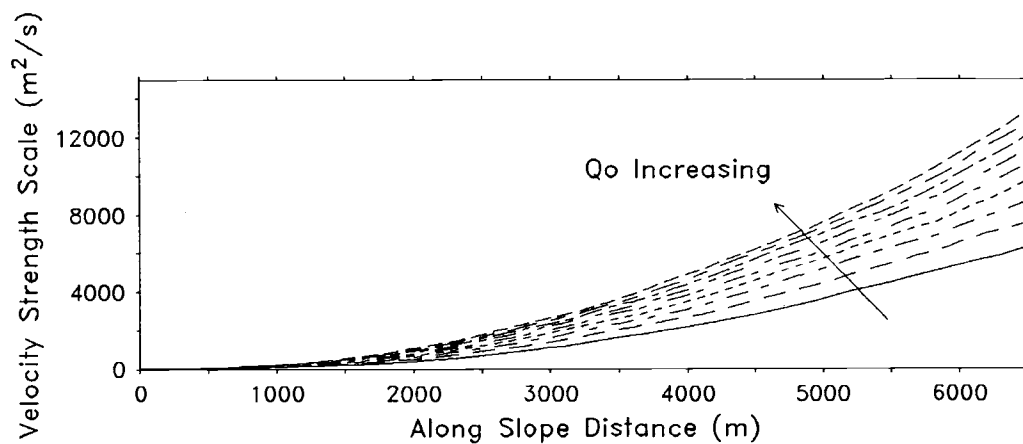


Figure 2.16: Velocity strength scale versus downslope distance for surface heat flux runs.

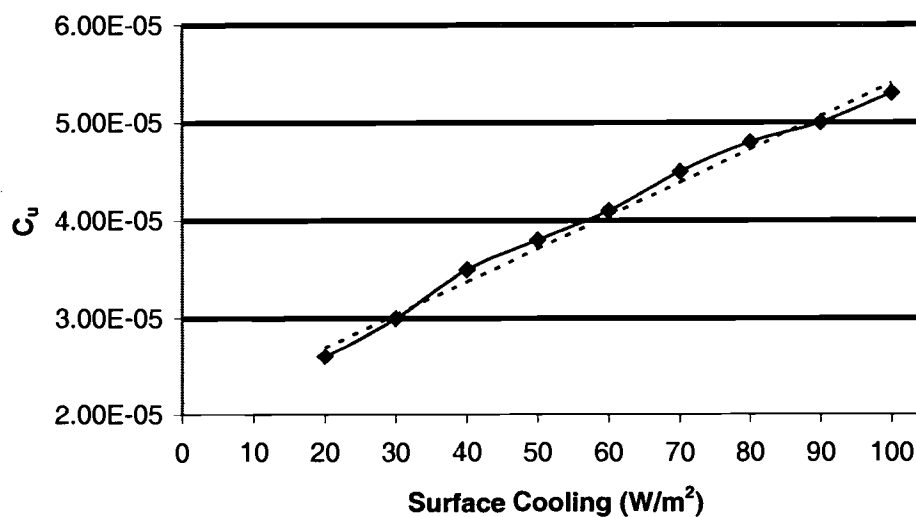


Figure 2.17: The coefficient of velocity strength scale versus surface heat flux for the model runs (-) and the parameterization (- -).

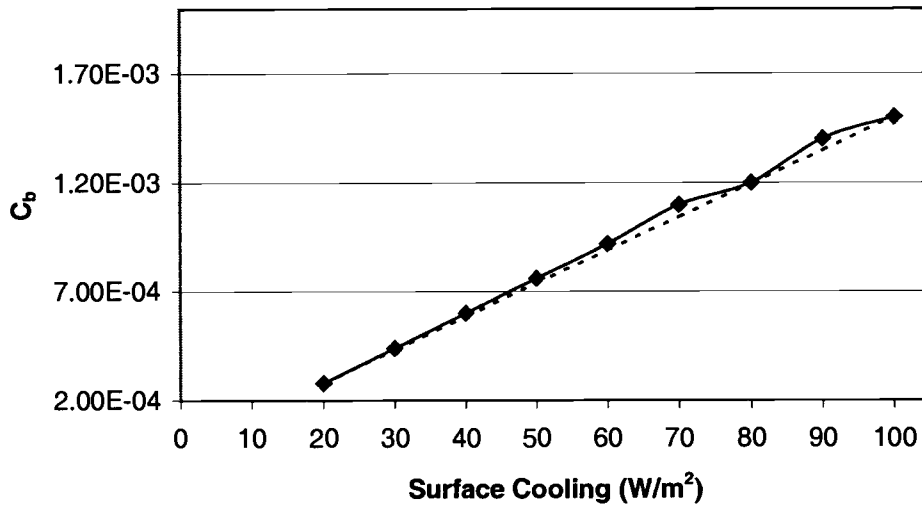


Figure 2.18: The coefficient of buoyancy strength scale versus surface heat flux for the model runs (-) and the parameterization (- -).

Further insight into the flow can be made by examining the total kinetic energy budget. Here the column kinetic energy is defined by

$$KE = \int_0^{h_u} \frac{1}{2} U^2 dz$$

where U is the down-slope velocity and h_u is the height where the down-slope velocity becomes arbitrarily close to zero. The column buoyant potential energy is defined by

$$BPE = \int_0^{h_u} \frac{d}{\theta_0} gh dz$$

Where h_b is the height where the buoyancy deficit becomes arbitrarily close to zero, h is average height of the flow, and the buoyancy deficit, d , is defined as the difference in temperature of the katabatic flow and the ambient air, at the same level.

$$d = \theta_{katabatic} - \theta_{ambient}$$

A plot of buoyant potential energy and kinetic energy versus down-slope distance for the surface heat flux runs is presented in figure 2.19. The buoyant potential energy has a maximum where buoyancy deficit and height products are highest, somewhere in the upper portion of the slope. Large buoyant potential energies are found at this location since the flow is being replenished with air that has cooled significantly over the upper portion of the slope through contact with the slope surface. Thus, as surface cooling increases, buoyant potential energies increase. Furthermore, larger buoyant potential energies can support larger kinetic energies, since dissipation of energy by mixing and drag also increases with surface cooling. Hence, the flows with the largest kinetic energies are those that are driven by the largest amount of surface cooling.

A measure of how efficiently a katabatic flow converts buoyant potential energy into kinetic energy can be defined as the katabatic efficiency, the ratio of change in kinetic energy to the change in buoyant potential energy.

$$\varepsilon = \frac{\Delta KE}{\Delta BPE}$$

Where ΔKE is calculated from the top of the slope to the bottom, and ΔBPE is calculated as the maximum buoyant potential energy over the slope minus the buoyant potential energy at the bottom of the slope.

A plot of katabatic efficiency versus surface heat fluxes is presented in figure 2.20. As can be seen, the katabatic efficiency is only a very weak function of surface heat fluxes, consistent with the self-similar behavior of the momentum budgets with respect to surface heat fluxes.

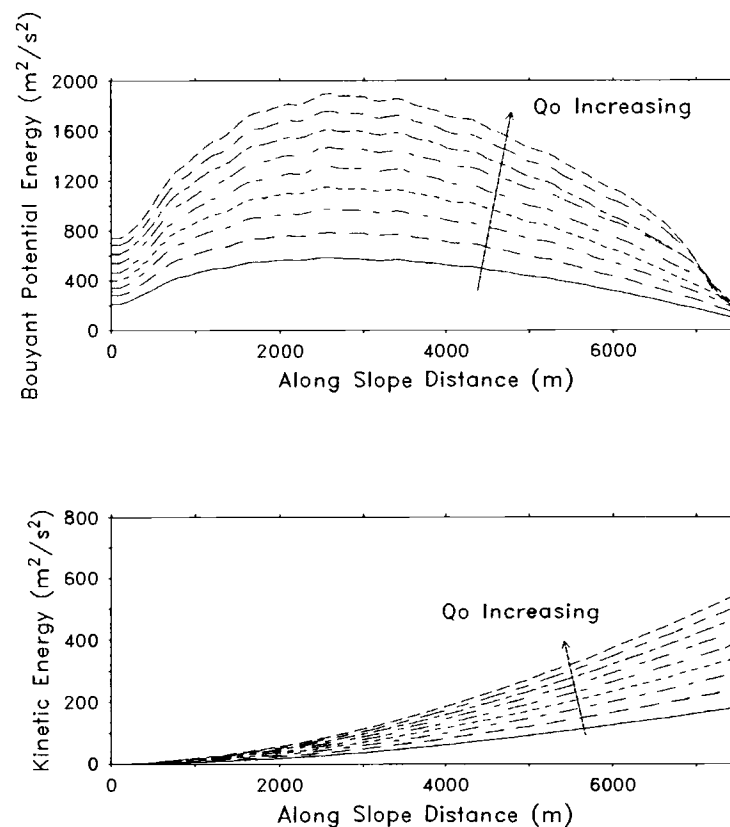


Figure 2.19: Buoyant potential energy (top) and kinetic energy (bottom) versus down-slope distance for surface heat flux runs.

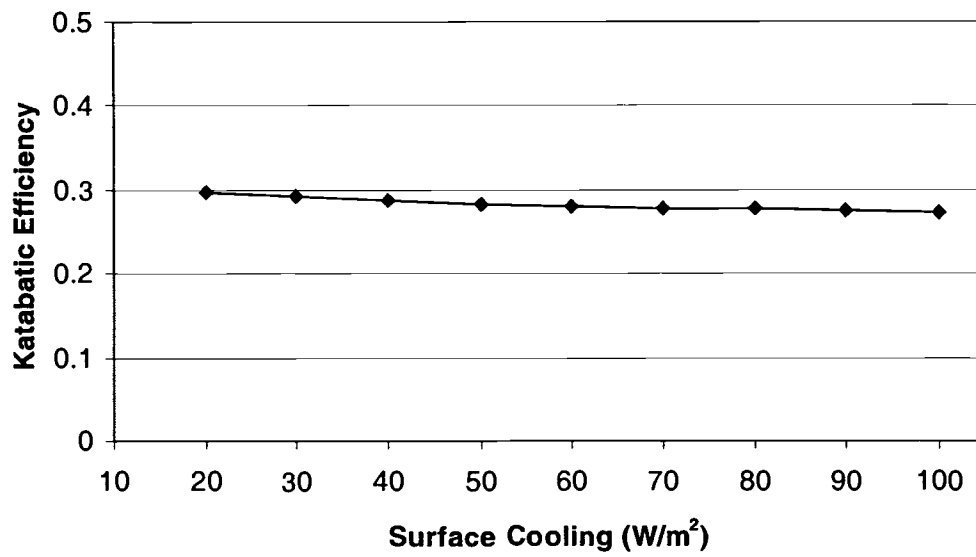


Figure 2.20: Katabatic efficiency versus surface heat flux.

2.4 The effect of slope angle

Simulations were run using the ARPS model to determine the effect of slope angle on drainage flow characteristics. The model runs are described in detail in section 2.1.1, and an X-Z cross section of the domain for different slope angles is shown in figure 2.21. The slope angle, α was varied from 4 to 16 degrees, in increments of 2 degrees. Surface fluxes were applied uniformly along the slope at 30 W/m^2 of cooling to drive the flow. The model was initialized at rest, with an isothermal atmosphere, and allowed to run for one hour of model time, by which time the flow had come to steady state.

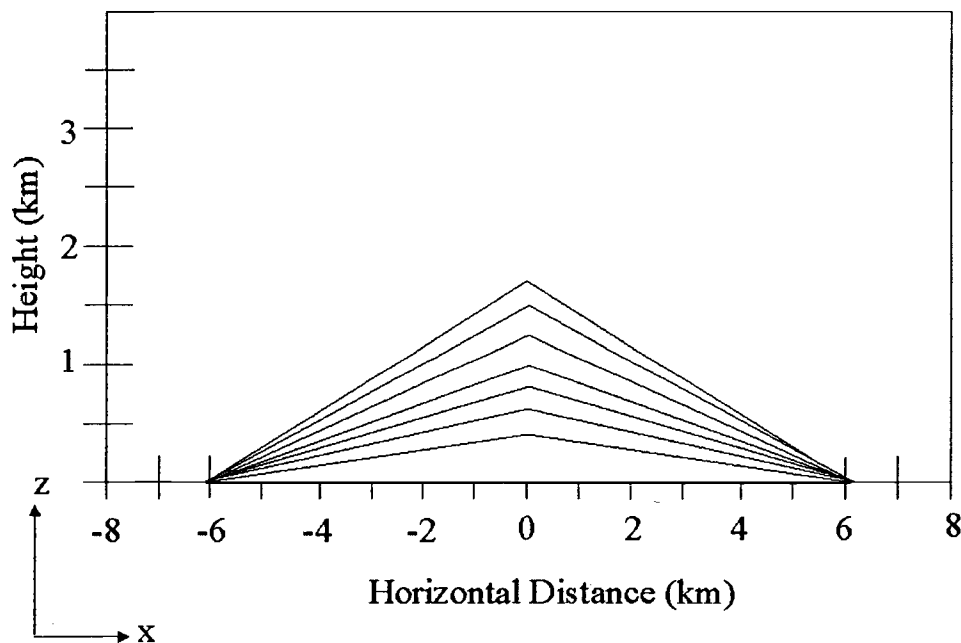


Figure 2.21: X-Z cross section of ARPS model domain for slope angle study runs.

Results of the simulations show that slope angle affects both velocity fields and temperature deficit fields. As slope angle increases the down-slope velocity increases, while the maximum temperature deficit decreases in magnitude. Figure 2.22 shows an X-Z cross section of the down-slope velocity evolution of the flow for slope angles of 4, 10 and 16 degrees. Figure 2.23 shows an X-Z cross section of the potential temperature evolution of the flow for slope angles of 4, 10 and 16 degrees. Figure 2.24 shows velocity profiles as a function of slope angle at a point 5 km from the top, near the foot of the slope. The height of the jet, n_{\max} , does not increase with increased slope angle, but the magnitude of the down-slope velocity jet increases from 3 m/s for the 4 degree slope angle case, to 4.6 m/s for the 16 degrees case. The buoyancy deficit profile 5 km down the slope as a function of slope angle is shown in figure 2.25. The buoyancy deficit decreases in magnitude from 8 K in the 4 degree slope angle case, to 2 K for the 16 degrees case. The decrease in buoyancy deficit with slope angle is partially due to the surface boundary condition. That is, the flow is required to cool by 30 W/m^2 at the surface, regardless of flow velocity. With decreasing slope angle, down-slope velocities decrease as well, so the flow must cool more to convect away the 30 W/m^2 imposed at the surface. It is probably not realistic to assume that a simple slope with high slope angle will cool just as much as simple slope with a low slope angle since there are a number of factors that would affect the down-slope variation of surface heat fluxes in real slope flows. As an example, since convective heat loss is a function of flow speed, and flow speed depends on slope angle, it follows that sensible heat fluxes from the surface will be a function of slope angle, and surface heat fluxes from a shallow slope should not be equal to those of a steep slope. Also, since convective heat loss from a surface is proportional to the

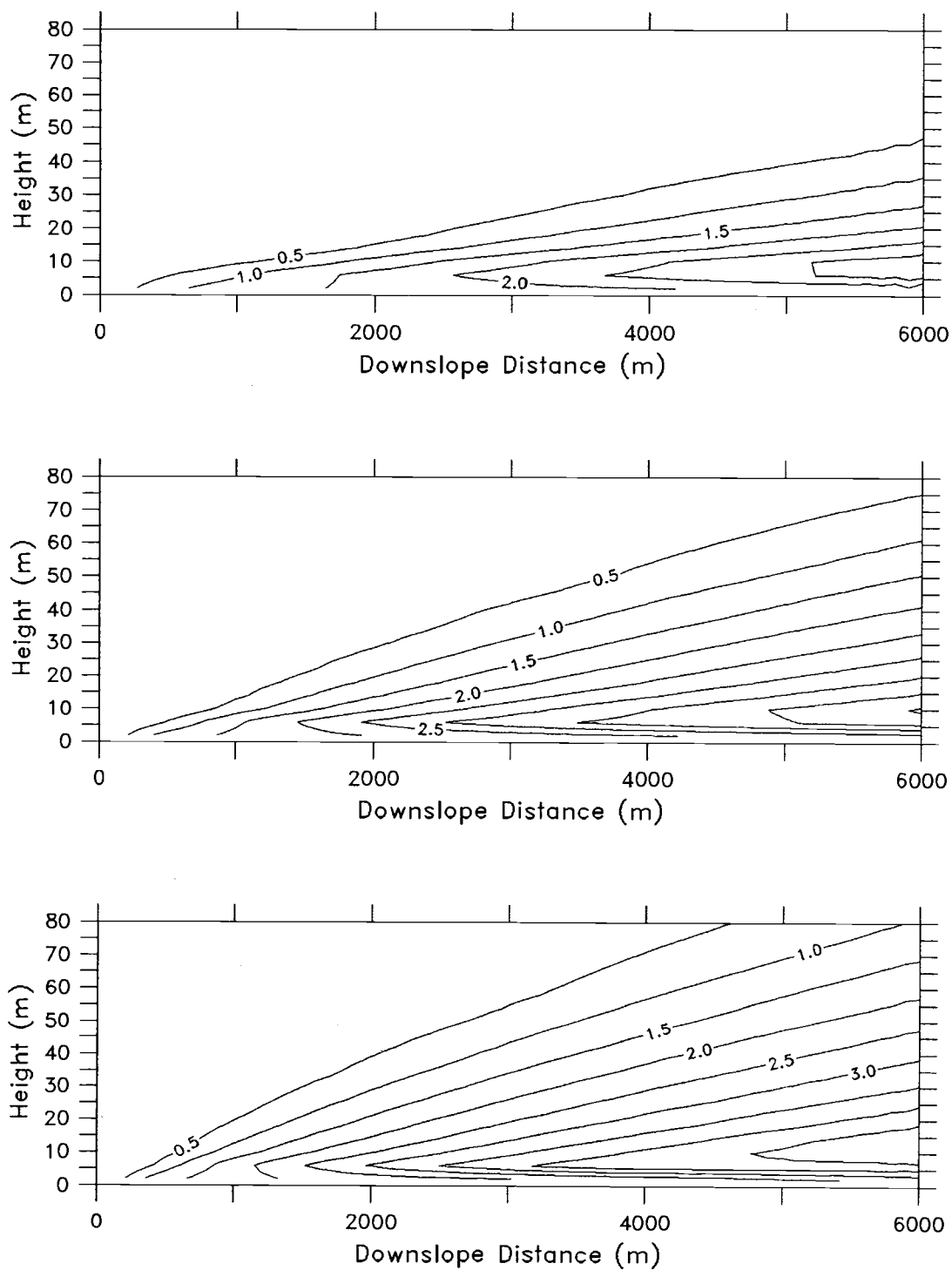


Figure 2.22: X-Z cross section of the down-slope evolution of velocity fields for $\alpha = 4, 10$, and 16 degrees.

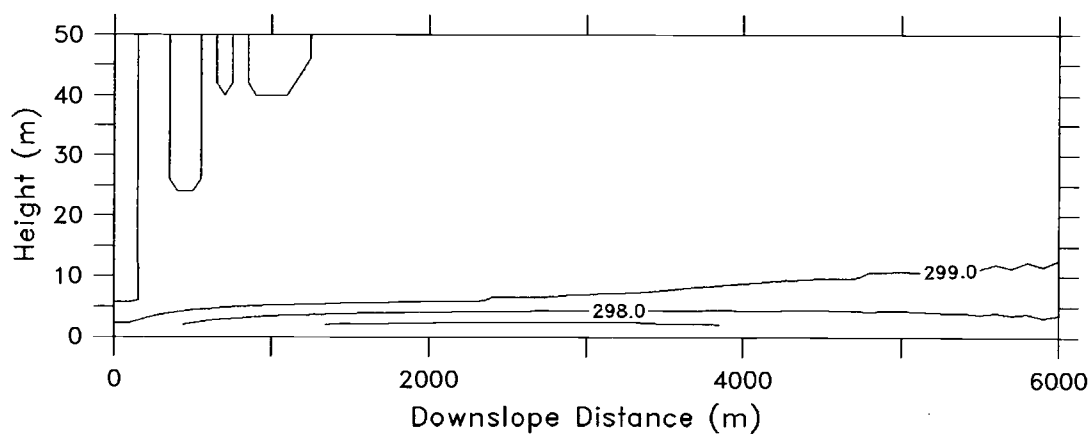
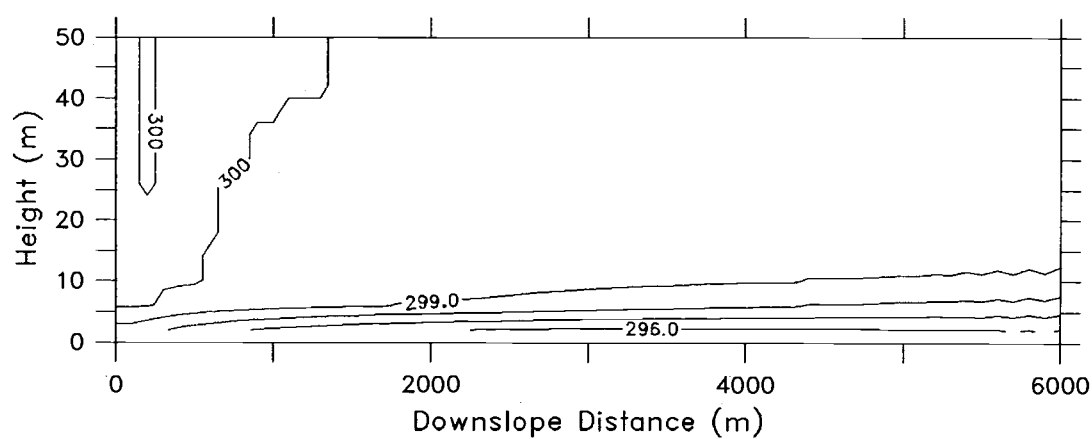
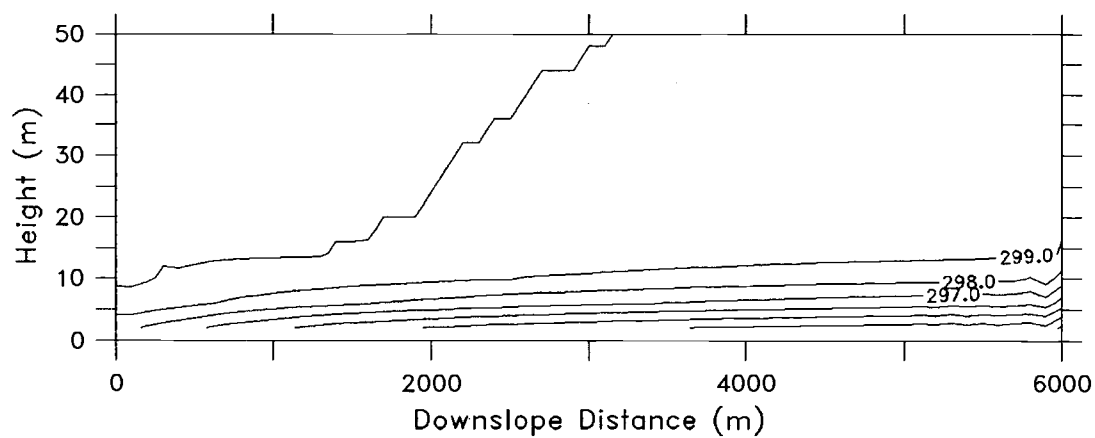


Figure 2.23: X-Z cross section of the down-slope evolution of potential temperature fields for $\alpha = 4, 10$, and 16 degrees.

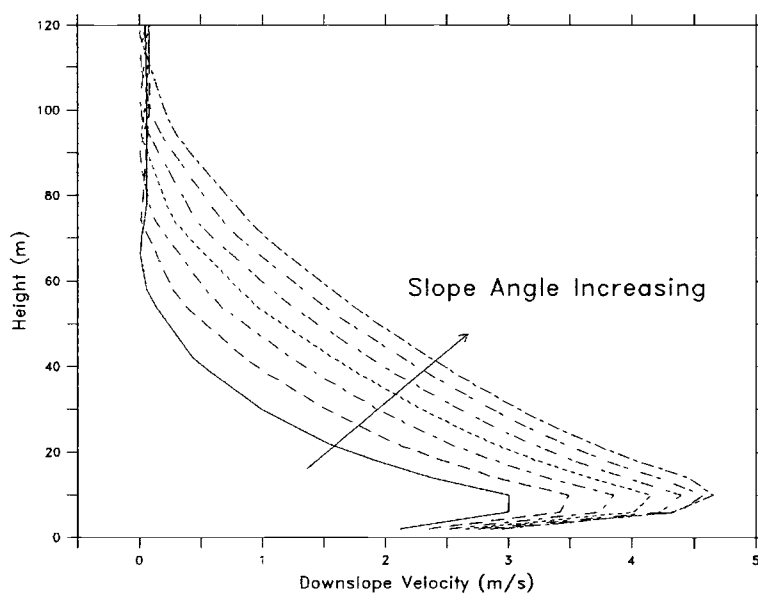


Figure 2.24: Velocity profiles as a function of height for slope angle runs at 5 km down-slope.

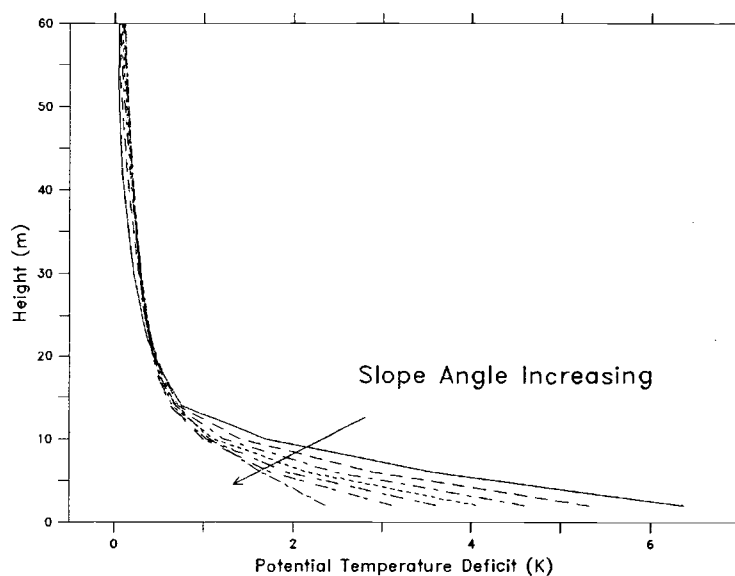


Figure 2.25: Buoyancy deficit profiles as a function of height for slope angle runs at 5 km down-slope.

temperature difference between the surface and the air just above the surface, and this temperature difference decreases with down-slope distance, it follows that assuming a surface heat flux constant with down-slope distance is not a realistic approximation.

The along slope momentum budget 5 km down the slope as a function of slope angle is shown in figure 2.26. The advection term increases greatly in magnitude with increasing slope angle, indicating that, at higher levels, horizontal advection of lower momentum from up slope is becoming more important. Entrainment of overlying ambient air into the flow increases as slope angle increases as well, and as entrainment increases so does the depth of the flow, as can be seen in figure 2.24.

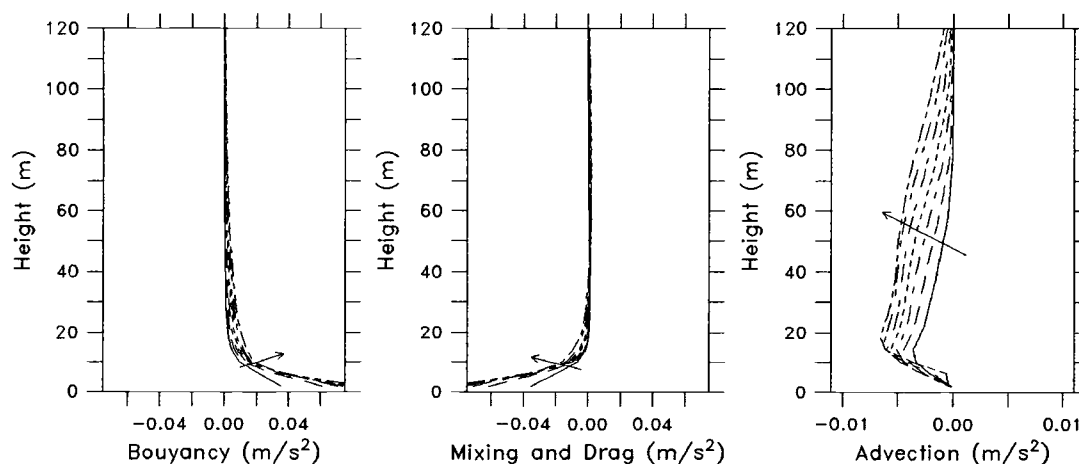


Figure 2.26: Along slope momentum budget 5 km down slope as a function of slope angle. The arrow points in the direction of increasing slope angle.

A plot of velocity strength scales versus down-slope distance for different slope angles is shown in figures 2.27. Also, a plot of buoyancy strength scales

versus down-slope distance for different slope angles is shown in figures 2.28. The buoyancy strength scale actually decreases with increasing slope angle due to higher near surface velocities leading to smaller potential temperature deficits with increasing slope angle. This is partly due to the surface thermodynamic boundary condition that 30 W/m^2 be applied at the surface regardless of slope angle. In actuality, surface cooling is probably a function of slope angle.

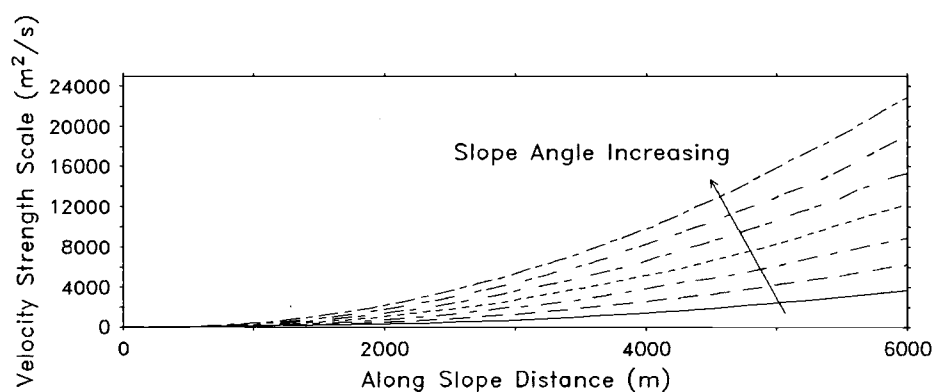


Figure 2.27: Velocity strength scale versus down-slope distance for slope angle runs.

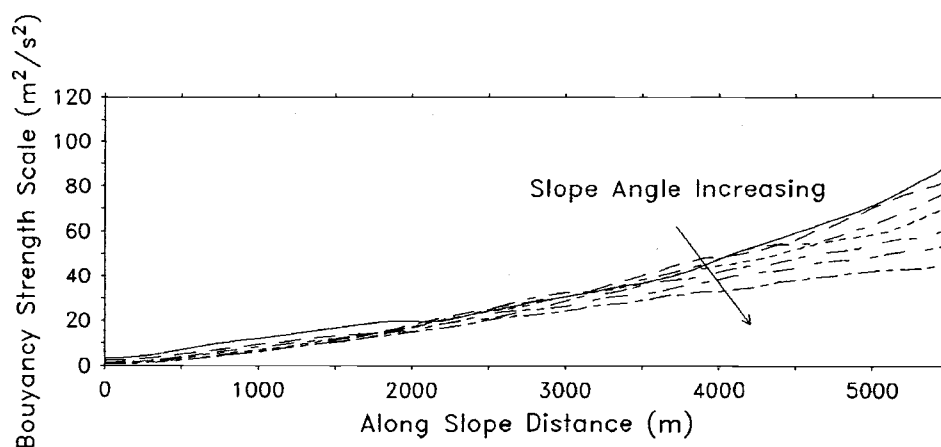


Figure 2.28: Buoyancy strength scale versus down-slope distance for slope angle runs.

It can be seen from figures 2.27 and 2.27 that velocity and buoyancy strength scales both depend on slope angle. Parameterizations of these scale parameters have been developed to account for slope angle. These parameterizations have the form

$$UH = C_u(\alpha) s^m$$

$$\Delta'H' = C_b(\alpha) s^n$$

Where C_u and C_b are constants that depend on various physical parameters of the flow, and s is the along slope distance. For the buoyancy strength scale, $n = 1.4$, while for the velocity strength scale $m = 2.2$. For the cases of constant surface heat fluxes, C_b and C_u , the coefficients for buoyancy and velocity strength scales, can be shown to be a function of slope angle. Plots of the coefficient of velocity strength scale and buoyancy strength scales are shown in figures 2.29 and 2.30, respectively. A table of the tabulated variation of velocity and buoyancy strength scale coefficients with slope angle is presented below.

α (degrees)	$C_b * 10^{-4} \text{ (m}^{-0.2} \text{ s}^{-1}\text{)}$	$C_u * 10^{-5} \text{ (m}^{0.8} \text{ s}^{-1}\text{)}$
4	5.02	1.71
6	4.53	3.04
8	4.31	4.39
10	3.83	6.00
12	3.61	7.87
14	3.03	9.62
16	2.96	12.0

Table 2.2: The variation of velocity and buoyancy strength scale coefficients with slope angle

In the range of 4 to 16 degrees, predictions for velocity and buoyancy strength scale coefficients can be made as a function of the slope angle, α , using the following relations

$$C_u = 1.71 * 10^{-5} + 5.0 * 10^{-4} * (\sin \alpha - 0.0698)$$

$$C_b = 5.02 * 10^{-4} - 1.0 * 10^{-3} * (\sin \alpha - 0.0698)$$

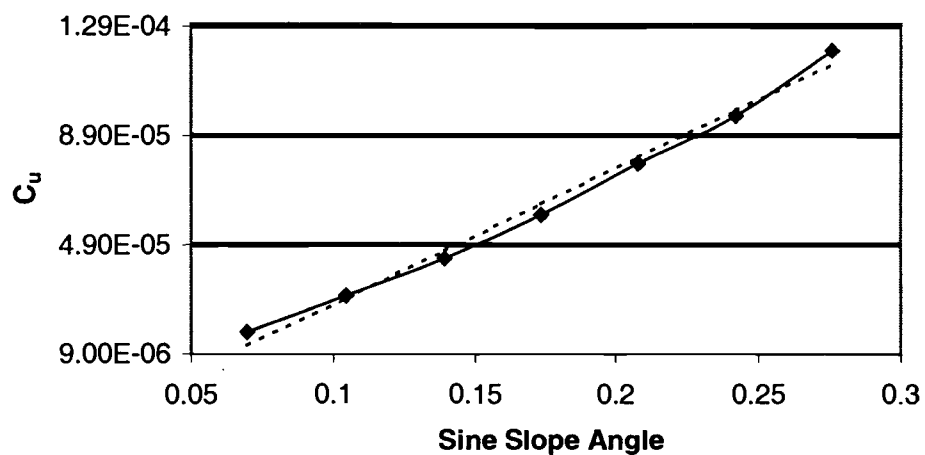


Figure 2.29: The coefficient of velocity strength scale versus sine of slope angle for the model runs (-) and the parameterization (- -).

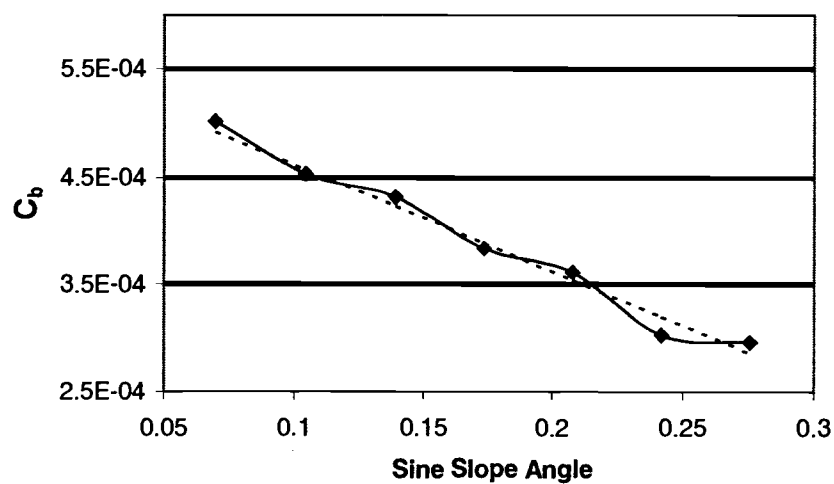


Figure 2.30: The coefficient of buoyancy strength scale versus sine of slope angle for the model runs (-) and the parameterization (- -).

A plot of buoyant potential energy and kinetic energy versus down-slope distance for the slope angle runs is presented in figure 2.31. As slope angle increases, mountain height increases, and buoyant potential energies increase due to the increase in mountain height. Larger kinetic energies are derived from larger buoyant potential energies, since dissipation of energy by mixing and drag also increases with slope angle, so the highest kinetic energies are found on slopes that have higher buoyant potential energies, i.e., the highest slopes.

A plot of the variation of katabatic efficiency with sine of slope angle is presented in figure 2.32. As can be seen, the katabatic efficiency goes up with increasing slope angle. When slope angle increases, not only is there an increase in kinetic energy due to a larger input of buoyant potential energy, but of that available buoyant potential energy, a higher percentage is converted into kinetic energy. One might be tempted to explain this using the argument that in katabatic flows buoyant potential energy is converted into kinetic energy over a slope whose length determines the amount of energy conversion that takes place. Katabatic efficiency is a function of slope length in that, for a fixed horizontal distance, steeper slopes have longer slope lengths. Since conversion of kinetic energy from buoyant potential energy requires a finite amount of slope length, more energy conversion can be expected to take place over longer slopes. However, when katabatic efficiency is computed for a fixed slope length, instead of horizontal distance, the plot of katabatic efficiency versus slope angle remains relatively unchanged. So the effect of changing slope distance is not the main reason behind the increase in katabatic efficiency with increasing slope angle.

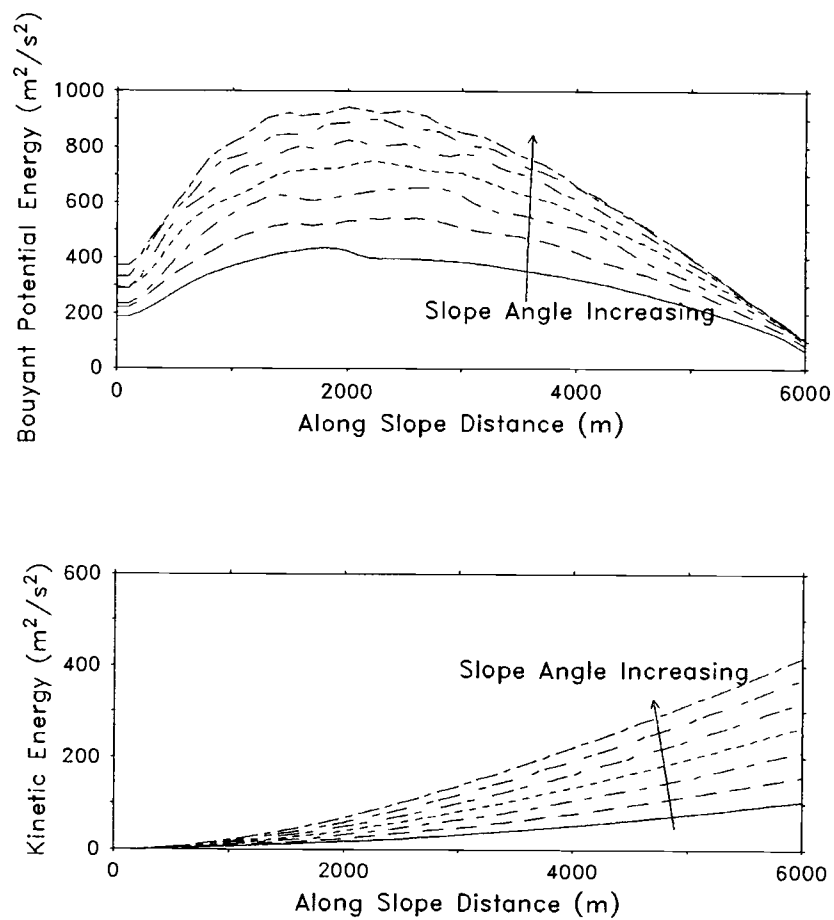


Figure 2.31: Buoyant potential energy (top) and kinetic energy (bottom) versus down-slope distance for slope angle runs.

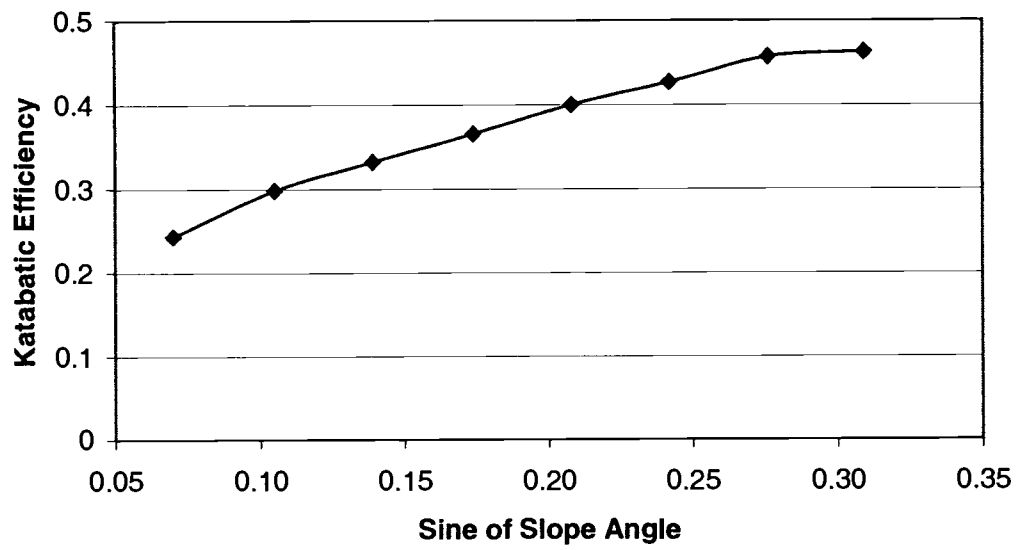


Figure 2.32: Katabatic efficiency versus sine slope angle.

2.5 The effect of ambient stratification

Simulations were run using the ARPS model to determine the effect of stable ambient stratification on drainage flow characteristics. The model runs are described in detail in section 2.1.1, and a X-Z cross section of the domain is shown in figure 2.8. The slope angle, α , was set to 6.1 degrees. The ambient stratification, Γ , was set to 0, 0.5, 1, 1.5, 2, 2.5, 3, 4, 5, and 6 K/km, where Γ is defined as the change in potential temperature with height.

$$\Gamma = \frac{d\theta}{dz}$$

Surface fluxes were applied uniformly along the slope at 30 W/m² of cooling to drive the flow. The model was initialized at rest, and allowed to run for one hour of model time, by which time the flow had come to steady state.

Results of the simulations show that ambient stratification strongly affects down-slope velocity and potential temperature deficit fields. As ambient stratification decreases, the flow deepens and the down-slope velocity increases in magnitude. This can be seen in figure 2.33, which shows an X-Z cross section contour of down-slope velocity profiles for the neutral, $\Gamma = 2$ K/km, and $\Gamma = 6$ K/km cases. Figure 2.34 shows an X-Z cross section contour of potential temperature profiles for the neutral, $\Gamma = 2$ K/km, and $\Gamma = 6$ K/km cases, and figure 2.35 shows down-slope velocity profiles as a function of surface fluxes at a point 6.5 km from the top, near the foot of the slope. The magnitude of the down-slope

velocity jet decreases from 4.3 m/s for the neutral stratification case, to 2.3 m/s for the 6 K/km stable stratification case. The buoyancy deficit profile 6.5 km down the slope is shown in figure 2.36. The buoyancy deficit decreases in magnitude from a maximum of 5 K in the neutral case, to 3 K for the 6 K/km stable stratification case. Since entrained ambient air into katabatic flows in very stably stratified ambient conditions is warmer than that of neutral to slightly stratified conditions, buoyancy deficits decrease with increasing stable stratification.

The down-slope momentum budget 6.5 km down the slope as a function of ambient stratification is shown in figure 2.37. The advection term in the momentum budget in the neutral case is larger in magnitude than it is for the stably stratified cases. Since katabatic flows in highly stably stratified ambient conditions grow little by entrainment of overlying air, velocity and buoyancy strength scales for these flows are smaller than those of katabatic flows in neutral to slightly ambient conditions. In very stably stratified flows, the ambient air that is entrained from above can be warm enough to arrest the growth of the depth of the katabatic flow. This can be seen more clearly in the down-slope velocity fields in figure 2.33, where for the highly stably stratified case, the flow ceases growing in the down-slope direction, and becomes nearly one dimensional at some point down the slope.

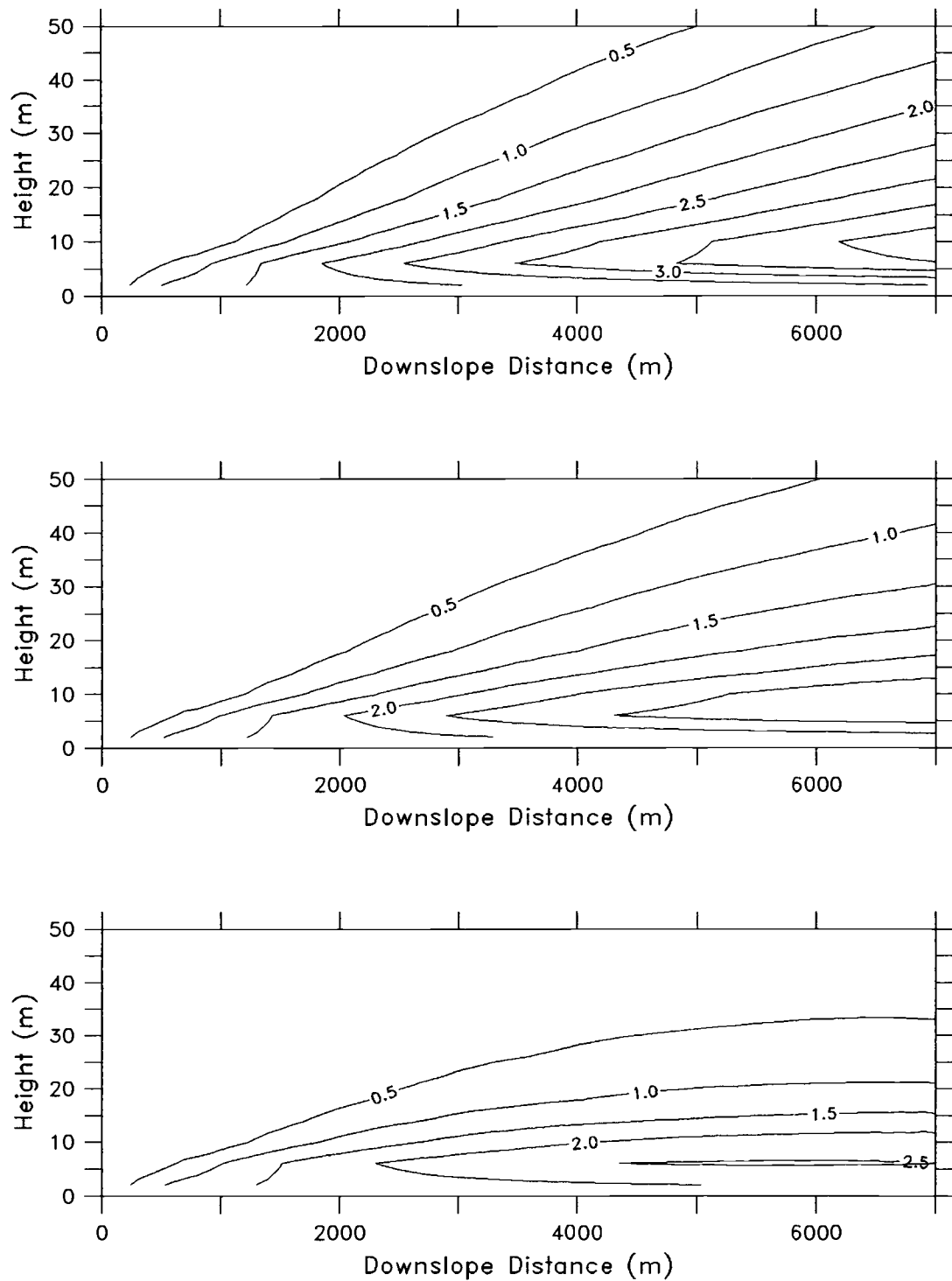


Figure 2.33: X-Z cross section contour of down-slope velocity profiles for the neutral (top), $\Gamma = 2$ K/km (middle), and $\Gamma = 6$ K/km (bottom) cases.

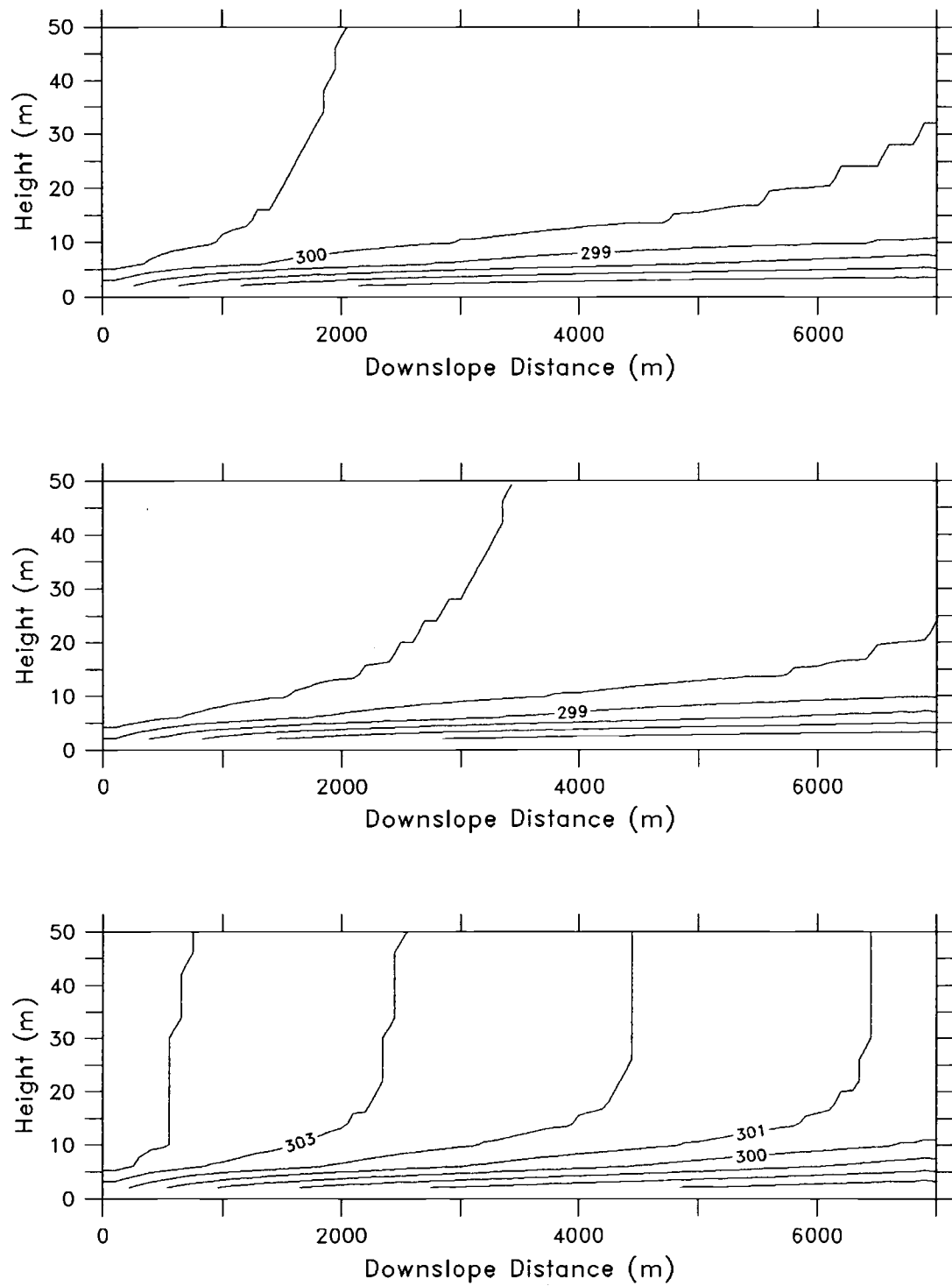


Figure 2.34: X-Z cross section contour of potential temperature profiles for the neutral (top), $\Gamma = 2$ K/km (middle), and $\Gamma = 6$ K/km (bottom) cases.

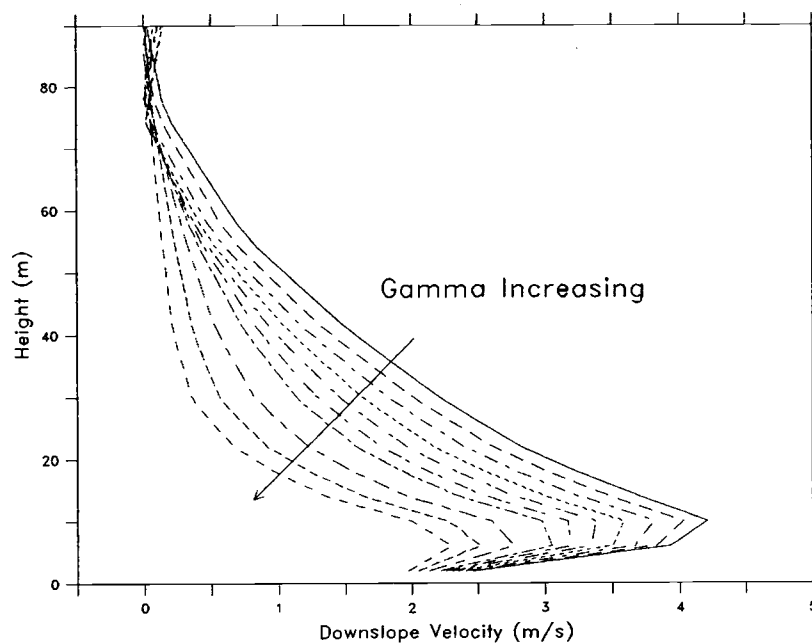


Figure 2.35: Velocity profiles as a function of height for ambient stratification runs at 6.5 km down-slope.

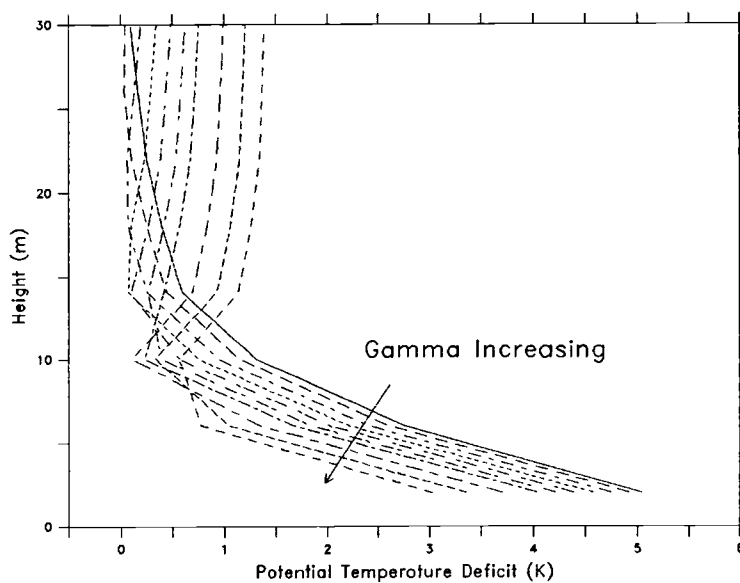


Figure 2.36: Potential temperature deficit profiles as a function of height for ambient stratification runs at 6.5 km down-slope.

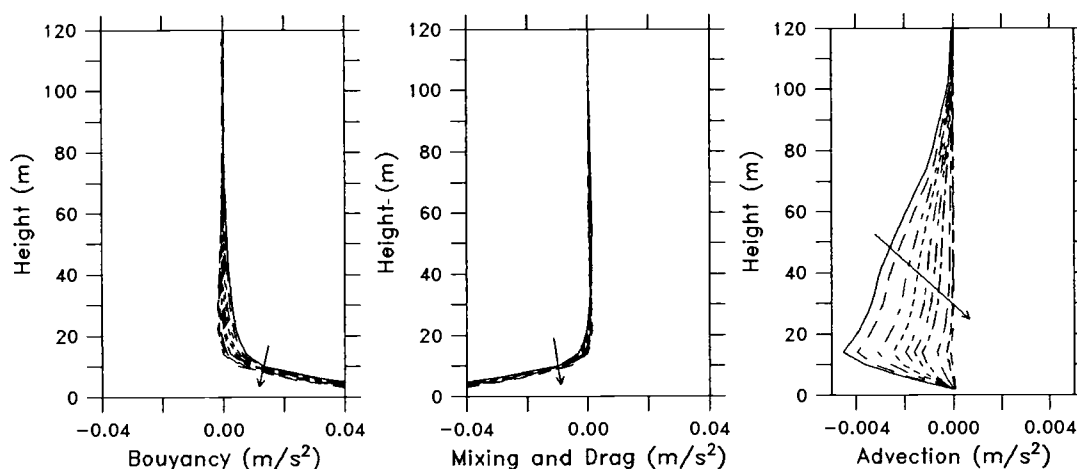


Figure 2.37: Along slope momentum budget as a function of height for ambient stratification runs 6.5 km down-slope. The arrow points in the direction of increasing ambient stratification.

A look at the total momentum budget reveals that buoyancy, advection, and mixing and drag terms in the momentum budget all decrease as ambient stratification increases. This can be seen in figure 2.38, a plot of the terms of the total momentum budget as a function of down-slope distance. At highly stable ambient stratifications the buoyancy term is asymptotic, consistent with the conclusion that the flow is no longer growing in the down-slope direction, and the growth of the katabatic flow by entrainment of overlying ambient air into the flow becomes less important.

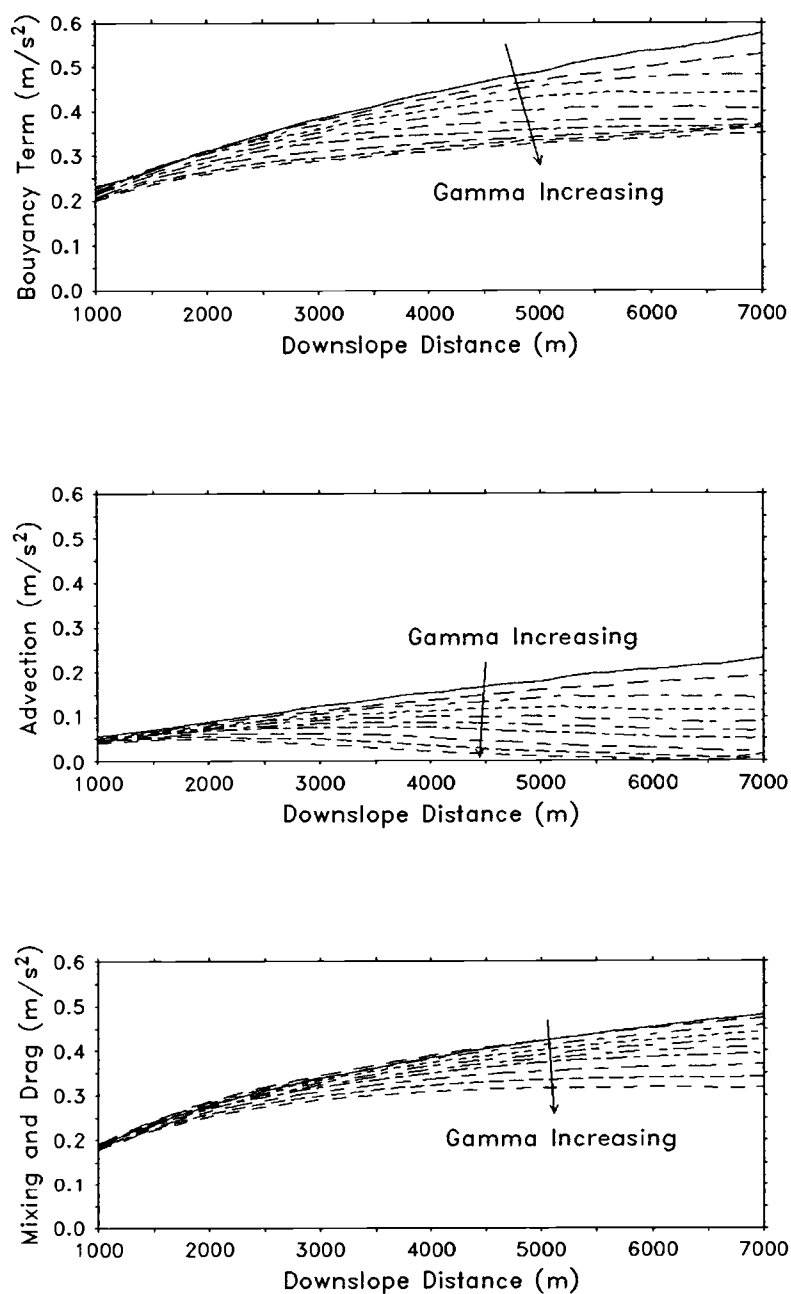


Figure 2.38: Buoyancy (top), advection (middle), and mixing and drag (bottom) terms in the total momentum budget as a function of down-slope distance for ambient stratification runs.

More insight into the effect of ambient stratification on the momentum budget of slope flows is presented in figure 2.39, a plot of the buoyancy normalized total momentum budget and total advection to mixing and ratio for all runs. As can be seen in this figure, mixing and drag become more important, and advection becomes less important as ambient stratification is increased. For the highly stratified runs, the momentum equation down the slope is reduced to a two-way balance between the buoyancy and the mixing and drag terms. These flows can be classified as equilibrium flows according to Mahrt (1982).

Plots of the buoyancy and velocity strength scales as a function of down-slope distance for different ambient stratifications, figures 2.40 and 2.41 respectively, more clearly reveal the arrest of the growth of katabatic flows in highly stably stratified atmospheres. As the stratification increases, the strength scale increases at a slower rate with down-slope distance, and ceases to grow at all for the highly stratified cases.

A plot of buoyant potential energy and kinetic energy versus down-slope distance for the ambient stratification runs is presented in figure 2.42. As ambient stratification increases, buoyant potential energy decreases due to the entrainment of warmer, overlying air. Larger kinetic energy is derived from larger buoyant potential energy, since dissipation of energy by mixing and drag also increases with ambient stratification. Hence kinetic energy in neutral to slightly stable ambient conditions is significantly higher than kinetic energy in highly stably stratified ambient conditions.

A plot of the variation of katabatic efficiency with ambient stratification is presented in figure 2.43. As can be seen, the katabatic efficiency is a strong function of ambient stratification. As ambient stratification increases, less buoyant potential energy is available to the flow, and of that available buoyant potential energy, even less is converted in kinetic energy.

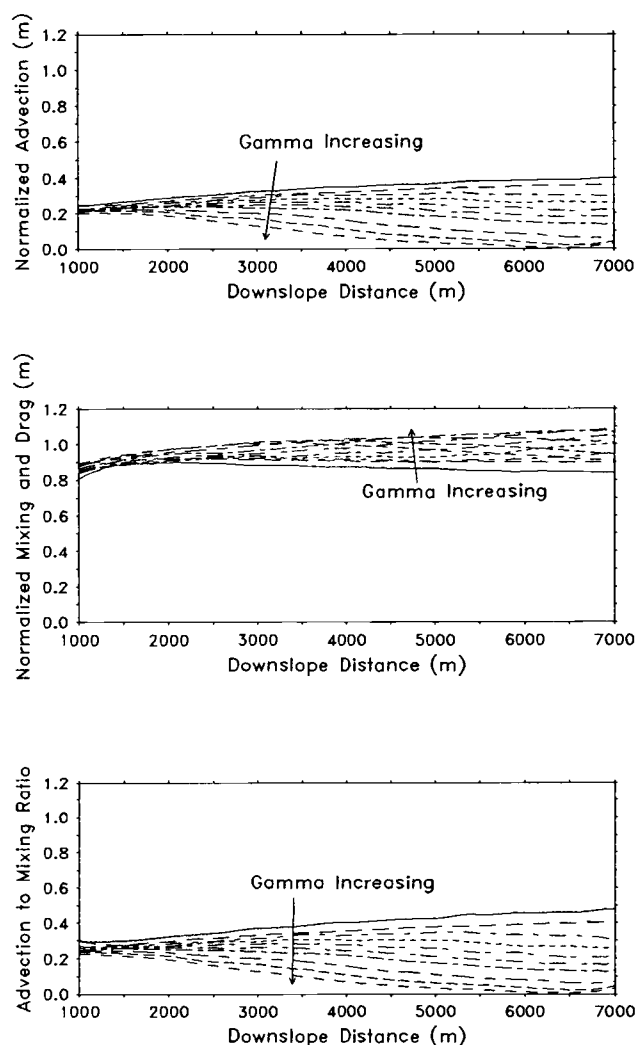


Figure 2.39: Buoyancy normalized momentum budget (top two) and advection to mixing ratio as a function of down-slope distance for ambient stratification runs.

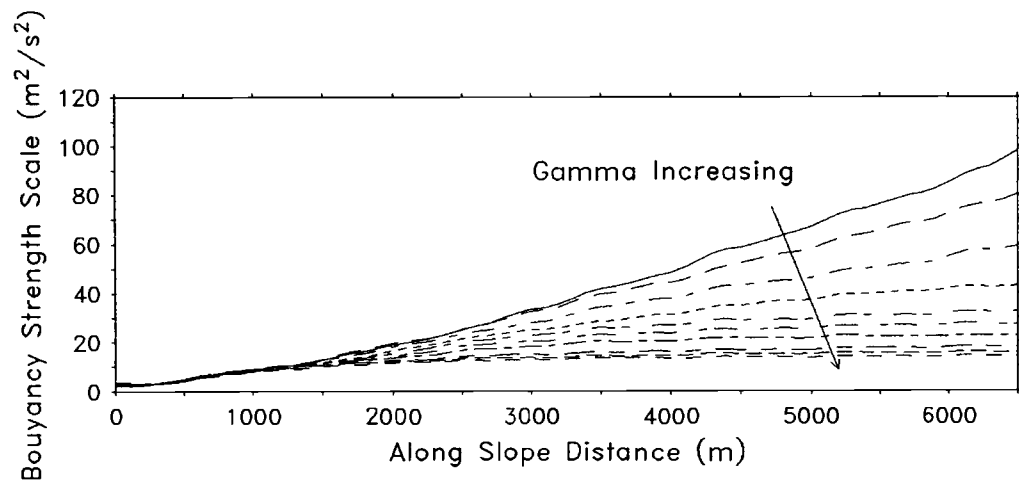


Figure 2.40: Buoyancy strength scale versus distance as a function for ambient stratification runs.

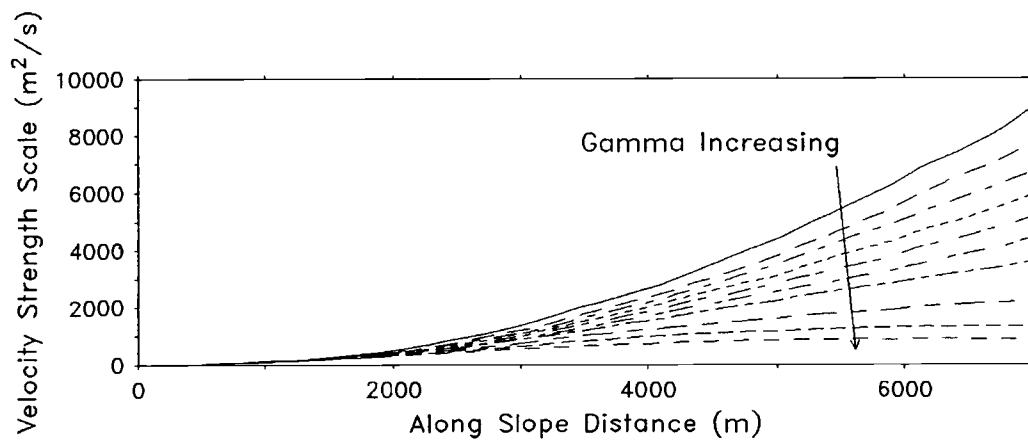


Figure 2.41: Velocity strength scale versus distance as a function for ambient stratification.

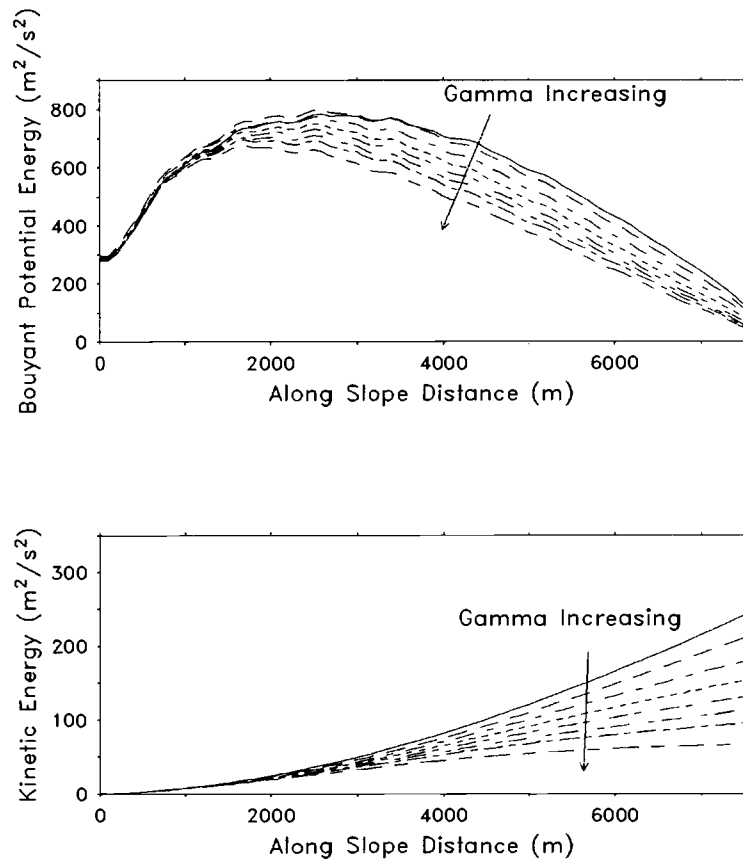


Figure 2.42: Buoyant potential energy (top) and kinetic energy (bottom) versus down-slope distance for ambient stratification runs.

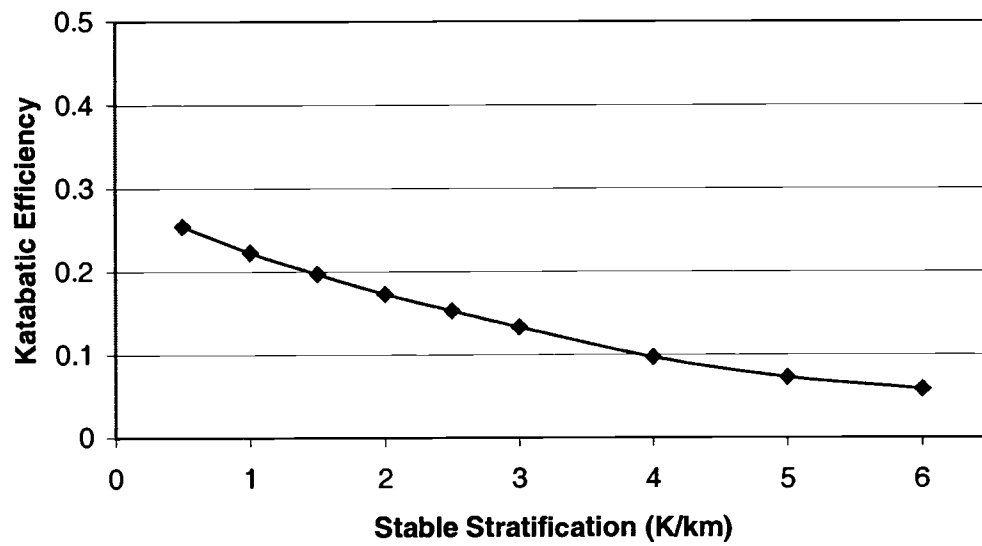


Figure 2.43: Katabatic efficiency versus ambient stratification.

3. Study of Combined Slopes versus Simple Slopes

3.1 Simple versus combined slopes

Simulations were run using the ARPS model to determine the effect of a change in slope angle on drainage flow characteristics. The model runs are described in detail in section 2.1.1, and an X-Z cross section of the right half of the domain is shown in figure 3.1. This figure shows both mountain profiles from the center of the modeling domain. The slope angle for the simple mountain profile, α_s was 6.1 degrees, while the upper and lower slope angles for the combined slope, α_2 and α_1 , were 11 and 1.6 degrees respectively. Also shown on this figure are locations A, B, C, where the flow will be analyzed. These locations are 2.5, 4.3, 6.9 km down-slope respectively. Thirty W/m^2 of cooling was applied uniformly along the slope to drive the flow. The model was initialized at rest, with a stable stratification of 1 K/km, and allowed to run for one hour of model time, by which time the flow had come to steady state.

Figure 3.2 shows the down-slope velocity profiles for the simple and combined slope at locations A, B, and C. The combined slope, with a steeper upslope angle, has a slightly greater down-slope velocity upslope of the discontinuity than the simple slope. However, down-slope of the slope discontinuity the combined flow grows much slower. Meanwhile, the flow on the simple slope continues to gain speed evenly all along the slope. This can be seen

more clearly in an X-Z cross section of down-slope velocity contours in figure 3.3. On the lower portion of the slope, the simple slope flow velocity jet is higher in magnitude than that of the combined flow, and the velocity profile is slightly deeper too. At location C, near the foot of the slope, the maximum velocity for the simple slope flow is roughly 5.2 m/s, while the maximum velocity for the combined slope flow is roughly 4.0 m/s. Thus, the decrease in slope angle has the effect of slowing the growth of the katabatic flow.

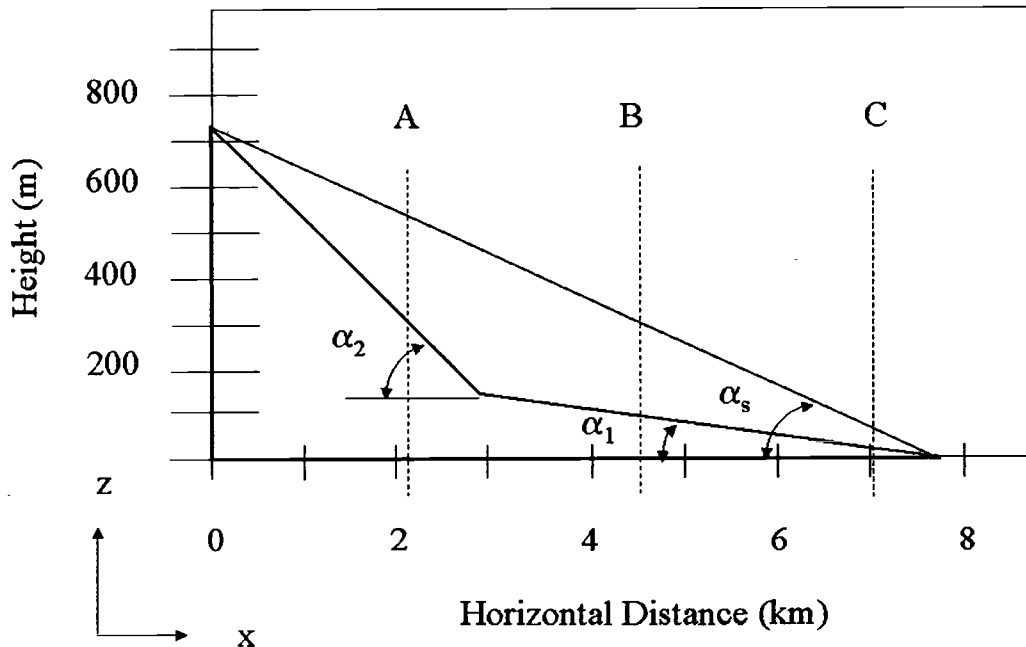


Figure 3.1: X-Z cross section of the right half of the ARPS modeling domain for combined slope study runs, showing simple and combined slope profiles.

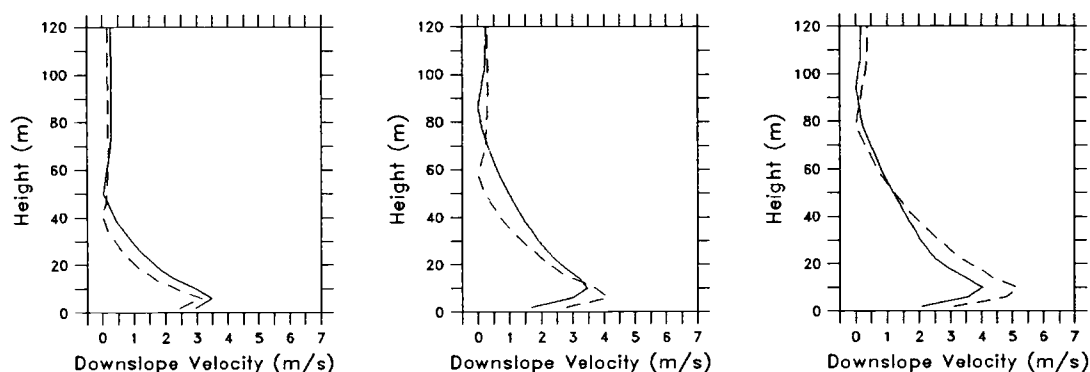


Figure 3.2: Velocity profiles of simple (- -) and combined (-) slopes at locations A (left), B (middle), and C (right).

Figure 3.4 shows the potential temperature deficit profiles for locations A, B, C. Along the lower portion of the combined slope, which has a very low slope angle, the combined flow cools more than the simple flow. At location C, near the foot of the slope, the potential temperature deficit of the flow near the surface of the combined slope is 8 K, while that of the foot of the simple slope is 5 K. Near the foot of the slope the combined slope flow has cooled more, while the simple slope flow is moving faster. This can be explained by looking back at the down-slope velocities in figure 3.3. The thermodynamic boundary condition imposed at the surface requires that the flow convect away 30 W/m^2 of heat, regardless of flow speed. Since the combined slope flow is moving much slower over the lower portion of the slope than the simple slope flow, the near surface air must cool more than the faster moving simple slope flow. It is not known whether or not the prescribed bottom thermodynamic boundary condition is representative of actual

katabatic flows. It is assumed, however, that this is probably not the case, as discussed in section 2.4.

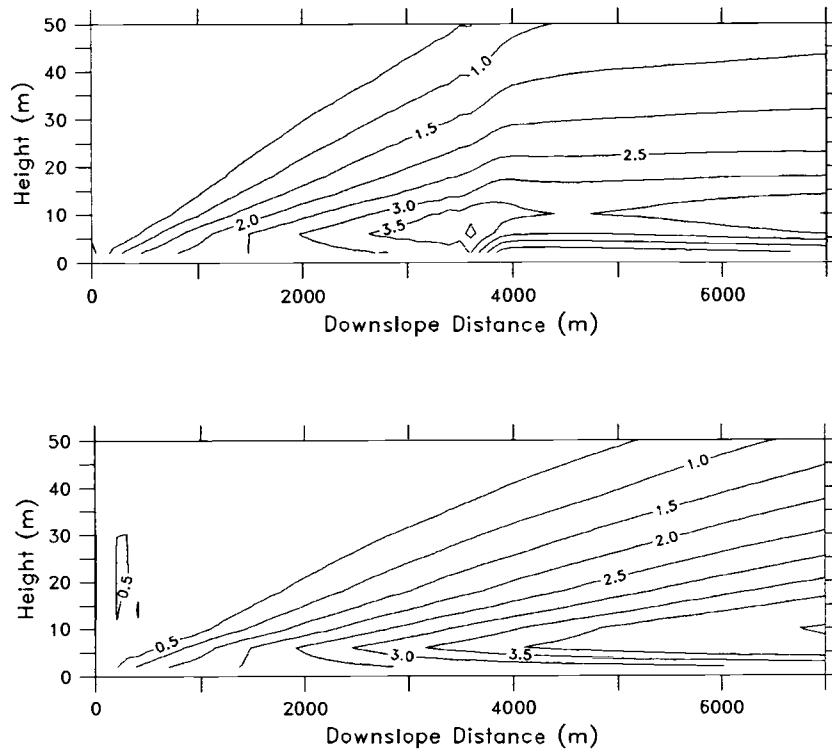


Figure 3.3: X-Z cross section of the down-slope evolution of velocity fields for combined (top) and simple (bottom) slope flows.

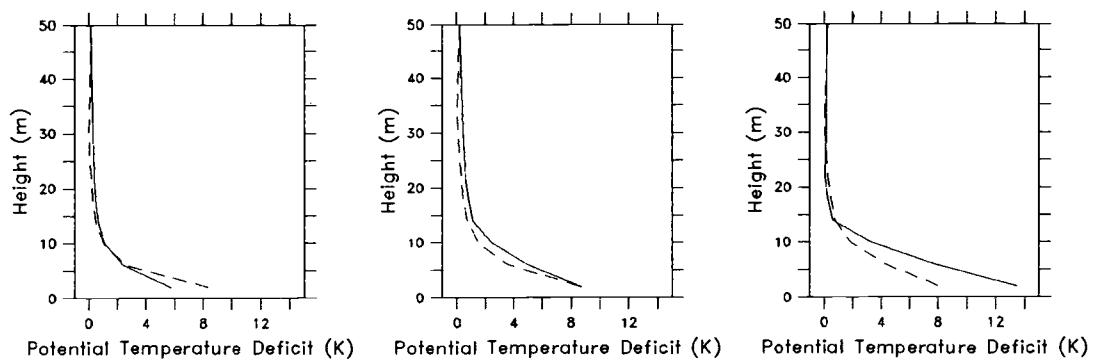


Figure 3.4: Potential temperature deficit profiles of simple (- -) and combined (-) slopes at locations A (left), B (middle), and C (right)..

In figure 3.5, the magnitude of TKE versus height above slope is shown for locations A, B, C. In figure 3.6, total TKE versus down-slope distance is shown for the combined and simple slopes. Hereafter, total TKE is defined as the column summed TKE from the surface to 200 m from the surface. Whereas the TKE for simple slope grows evenly with down-slope distance, the TKE for the combined slope flow is significantly reduced after the slope discontinuity. In the section of slope down-slope from the slope discontinuity, there is less TKE in the combined slope flow than the simple slope flow. With less TKE comes less mixing in the vertical and hence the combined slope flow is more confined to the surface, while the simple slope flow is deeper.

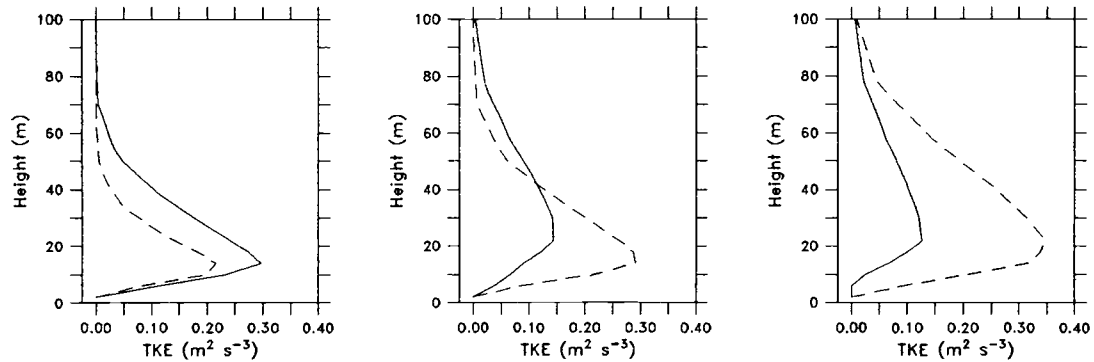


Figure 3.5: TKE profiles as a function of height for simple (- -) and combined (-) slope flows at locations A (left), B (middle), C (right).

Plots of the velocity and buoyancy strength scales as a function of down-slope distance are shown for the simple and combined cases in figure 3.7 and figure 3.8, respectively. As expected, the velocity strength scales of the flow scale with the slope angle in a predictable manner. That is, higher slope angle leads to a faster increase in velocity strength scale. On the other hand, higher slope angles lead to a

slower increase in buoyancy strength scales, as can be seen in figure 3.8. Upslope of the discontinuity, the simple slope buoyancy strength scale grows faster than that of the combined slope, since the simple slope has a smaller slope angle here.

Down-slope of the discontinuity, the simple slope buoyancy strength scale grows slower than that of the combined slope since the simple slope flow is partitioning more of its energy into kinetic energy to produce a faster moving flow than that of the combined slope.

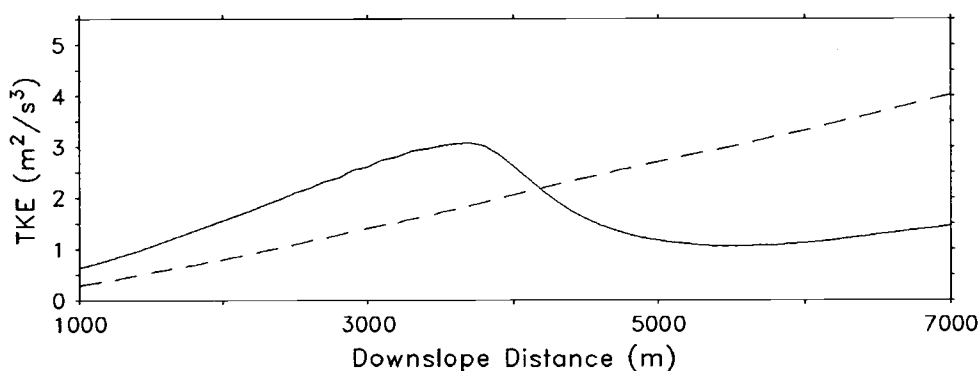


Figure 3.6: Total turbulent kinetic energy as a function of down-slope distance for combined (-) and simple (- -) slopes.

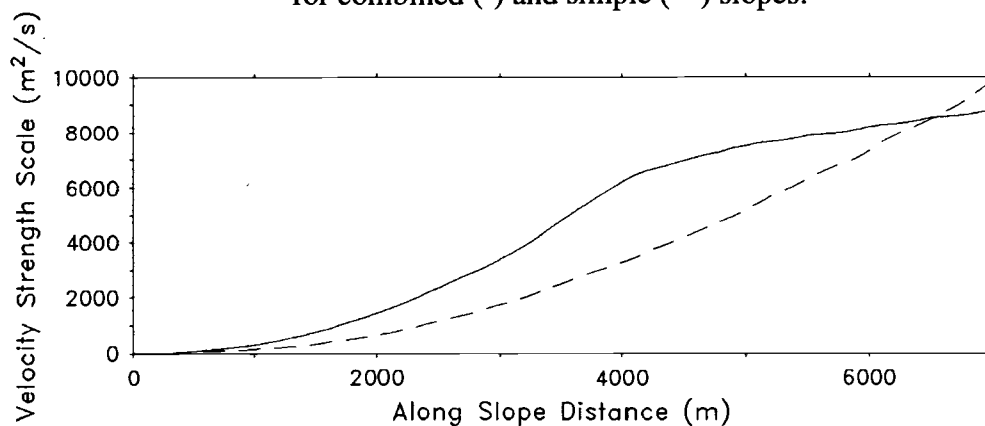


Figure 3.7: Velocity strength profiles as a function of down-slope distance for simple (- -) and combined (-) slope flows.

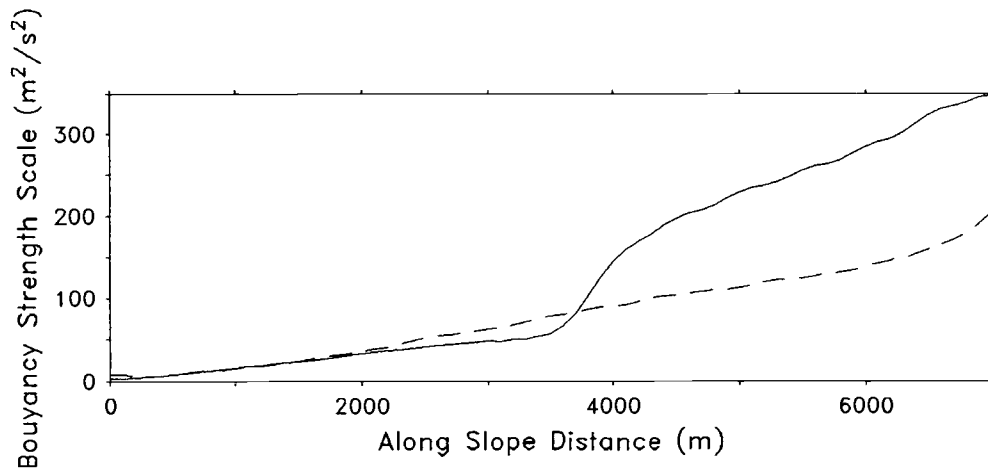


Figure 3.8: Buoyancy strength profiles as a function of down-slope distance for simple (- -) and combined (-) slope flows.

An interesting aspect of katabatic flows was noted by Manins and Sawford (1979a), who pointed out that most drainage flows are everywhere supercritical. That is, no information can be passed upstream, and information about all disturbances, including slope discontinuities, is swept downstream. Thus the flow upstream of the slope discontinuity has no knowledge of the flow over the lower portion of the slope. This explains the hydraulic jump in the flow at the slope discontinuity that indicates that the flow is adjusting to a new slope angle. The grid resolution in the model is not sufficient to resolve the hydraulic jump, which would be smeared out by turbulence anyway. However, the portion of the slope above the slope discontinuity is easily modeled using the parameterizations for buoyancy and velocity strength coefficients for the higher slope angle presented in chapter two. The flow downstream of the slope discontinuities also grows according to parameterizations developed in chapter two based on the slope angle, but in a way that is offset due to the upstream portion of higher slope angle. Like Horst and

Doran (1983), attempts to parameterize the upstream effect on the flow downstream of the slope discontinuity were met with ambiguity. The result obtained was that the velocity strength downstream of the slope discontinuity grew at a rate proportional to its slope angle, but offset by 12 km in the down-slope direction. That is, the velocity strength scale downstream of the slope discontinuity matched a parameterization for velocity strength scales for a slope with the same slope angle, only 12 km longer. The reason for the combined flow to be offset by this distance is unknown, but is explored further in the next section.

More insight into the physics of the simple and combined flows is gained by a plot of the total advection to mixing ratio in the total momentum budget as a function of down-slope distance. This is shown in figure 3.9. Down-slope of the slope discontinuity, horizontal advection of lower momentum from up-slope by the combined flow becomes much smaller in magnitude. Thus, down-slope of the discontinuity, the combined flow is slowed mostly by mixing and drag, and advection is less important than for the simple flow, producing a shallower flow than that of the simple slope.

A plot of buoyant potential energy and kinetic energy versus down-slope distance for the simple and combined flows is presented in figure 3.10. There are two maximums in the plot of buoyant potential energy versus down-slope distance for the combined flow, and all along the slope, parcels of the simple flow have higher buoyant potential energy than that of the combined flow, since the simple slope is everywhere higher than the combined slope. Increased down-slope kinetic energies in the simple flow are a direct result of increased buoyant potential energies. Thus, the simple slope flow has more buoyant potential energy to

partition into kinetic energy than does the combined flow. The flows have a very similar katabatic efficiency, 0.24 for the simple slope, and 0.23 for the combined slope. As was shown earlier, katabatic efficiencies increase with increasing slope angle, so it follows that the efficiency of a combined slope can be expected to approach that of a simple slope with slope angle greater than the smaller combined slope angle, and less than the greater combined slope angle. However, due to the enhanced region of mixing located just down-slope of the slope discontinuity, the combined flow has a katabatic efficiency slightly lower than that of the simple slope

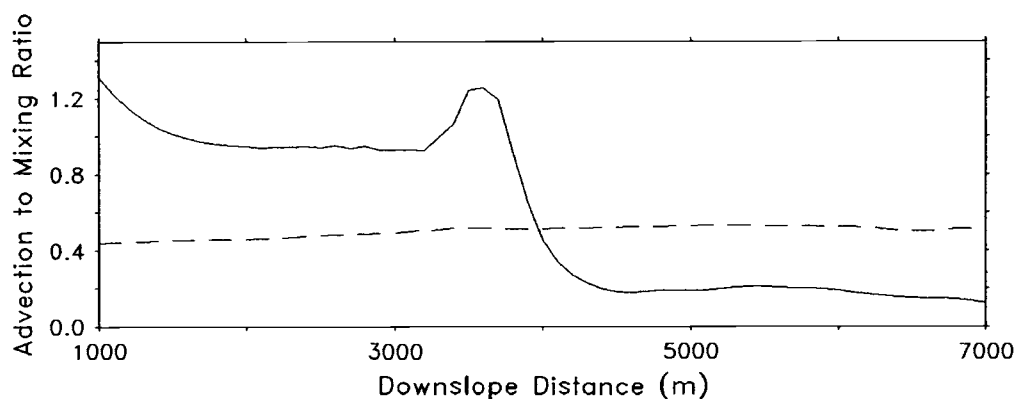


Figure 3.9: Advection to mixing ratio as a function of down-slope distance for simple (—) and combined (---) slope flows.

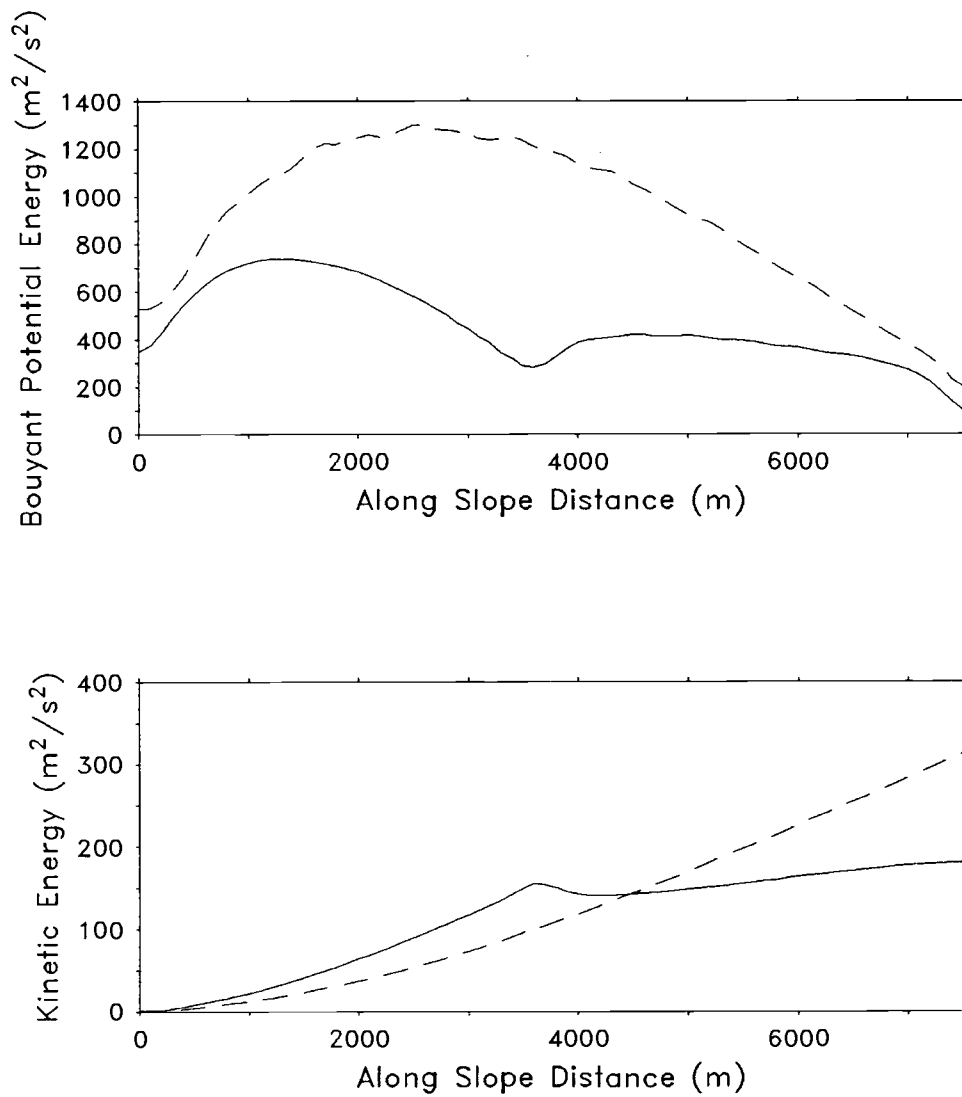


Figure 3.10: Buoyant potential energy (top) and kinetic energy (bottom) versus down-slope distance for simple (- -) and combined (-) slope flows.

3.2 The equivalent slope angle method

Simulations were run using the ARPS model to determine the effect of a changing upper slope angle on drainage flow characteristics over combined slopes. In this portion of the study, the effect of changes in terrain profile will be examined in order to produce some guidelines that will enable us to account for subgrid scale terrain features in katabatic flow models.

The model runs are described in detail in section 2.1.1, and a X-Z cross section of the right half of the domain showing mountain profiles is shown in figure 3.11. The lower slope angle for all the mountain profiles, α_1 , was 5.7 degrees, while the upper slope angles were set to 5.7, 7.5, 9.2, 11.0, 12.7, and 14.5 degrees. Also shown on this figure is location A, 2 km down-slope of the change in slope angle, where the flow will be analyzed. At this point the flow over the combined slope has fully adjusted to the lower slope angle, and is free from the effects of the end of the slope. Thirty W/m^2 of cooling was applied uniformly along the slope to drive the flow. The model was initialized at rest, with an isothermal atmosphere, and allowed to run for one hour of model time, by which time the flow had come to steady state.

The goal of this portion of the study is to determine if the flow at point A of the combined slope can be parameterized as a simple slope of different slope angle. For the equivalent slope angle method, we will equate the flow at point A over the lower portion of the combined slope with a flow over an equivalent simple slope with a different slope angle, under the constraint that the equivalent slope has the

same horizontal distance as that of the total combined slope. This is shown graphically in figure 3.12. In this case, the idea is to tailor predictions of drainage flows based on the amount of terrain that is resolved by the model, and to develop an idea of how subgrid scale terrain feature can be accounted for in mesoscale models of katabatic flows. Relationships between the equivalent slope angle, total slope angle and combined slope angle ratio will be determined.

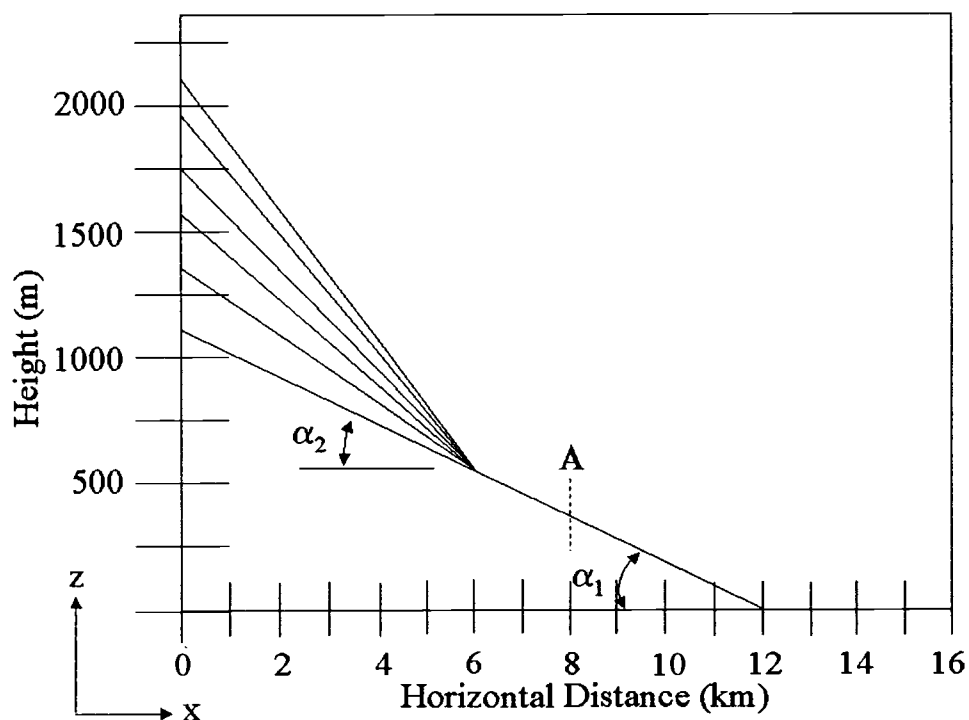


Figure 3.11: X-Z cross section of the right half of the ARPS modeling domain for upper slope angle combined slope study runs, and location A, where the flows will be compared.

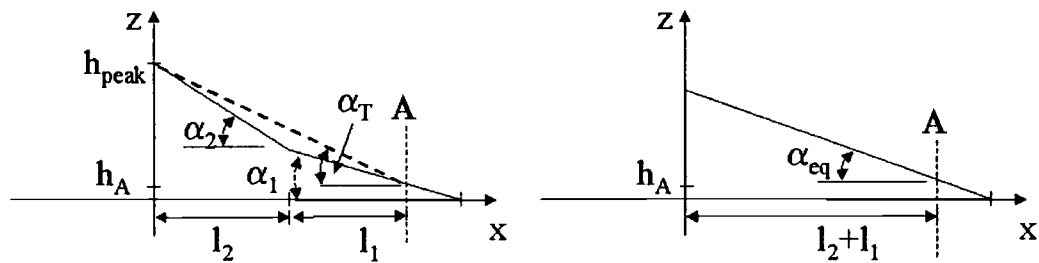


Figure 3.12: Graphical representation of equivalent slope angle method.

A plot of the X-Z velocity cross section contours for $\alpha_2 = 9.2, 14.5$, and 5.7 (simple slope) degrees is shown in figure 3.13. The slope discontinuity is located 6 km down-slope, and is readily apparent in the down-slope velocity contours. Figure 3.14 shows the down-slope evolution of velocity strength scales for the different cases. Over the portion of the lower slope where the flow is free from the effects of the discontinuity and the foot of the slope (near 8 km down-slope, location A), the velocity strength scales for all the flows grow at the same rate, that is, at the rate of growth for a flow with slope angle equal to α_l . However, since the flows with greater upper slope angle generate higher velocity strength scales over the upper portion of the slope, over the lower portion of the combined slope the combined slope velocity strength scales are larger in magnitude than those of a simple slope.

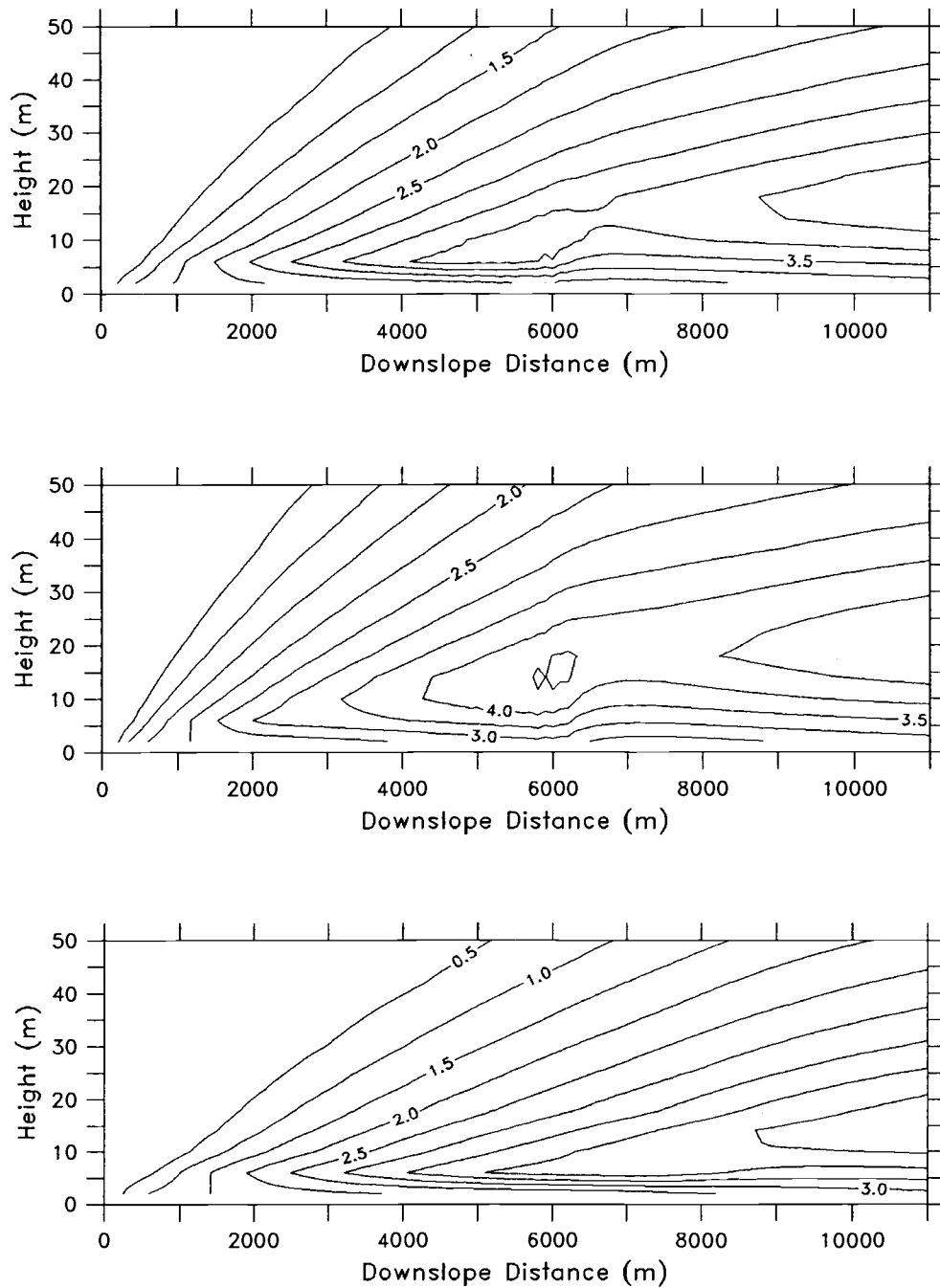


Figure 3.13: X-Z cross section of the down-slope evolution of velocity fields for combined slopes and simple slope flows. $\alpha_2 = 9.2$ for the top plot, $\alpha_2 = 14.5$ for the middle plot, and $\alpha_2 = \alpha_1 = 5.7$ for the bottom plot. The change in slope angle is located at 6 km.

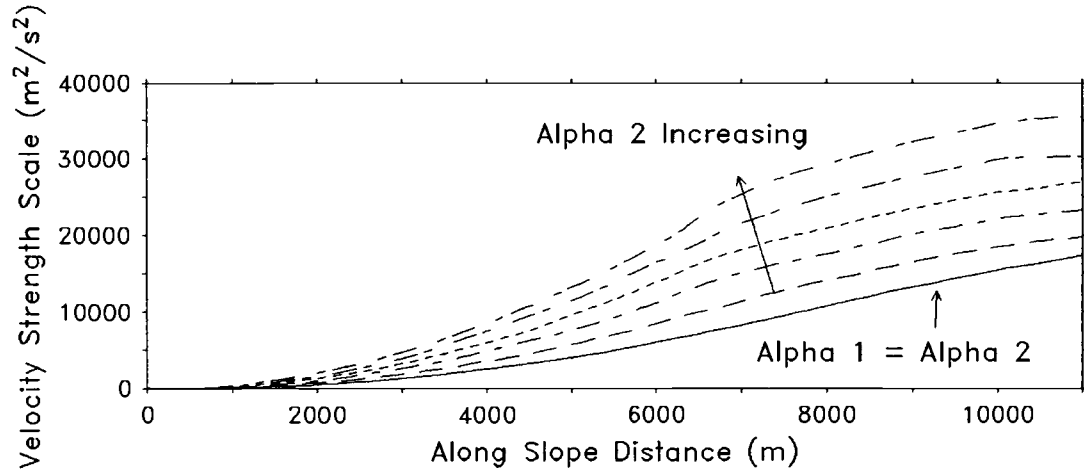


Figure 3.14: Down-slope evolution of velocity strength scales for the upper slope angle cases.

Results of the equivalent slope angle method are shown in figure 3.15, a plot of the equivalent slope angle versus combined slope angle ratio, α_2/α_1 . For $\alpha_1 = \alpha_2$, the slope is reduced to a simple one, and the equivalent slope angle is equal to the slope angle for the simple case, 5.74 degrees. As the ratio of upper slope angle to lower slope angle increases, the equivalent slope angle increases since more buoyant potential energy is needed to generate higher kinetic energy. Also plotted in figure 3.15 is a line that indicates an equivalent slope angle equal to the total slope angle. The total slope angle, α_T , is defined at point A as the angle that the combined slope would have if it were a simple slope, with the same horizontal distance, $l_1 + l_2$, and height, $h_{peak} - h_A$, as the combined slope, as shown in the left hand side of figure 3.12. Equivalent slope angle, α_{eq} is determined by using parameterizations of the coefficient of velocity strength scale as a function of slope angle developed in chapter two. The horizontal distance of the equivalent slope is constrained to be that of the combined slope from peak of the slope to point A.

For all combined slopes, the equivalent slope angle is smaller than the total combined slope angle. For all upper slope angles, combined slope flows have velocity strengths less in magnitude than simple slopes with a slope angle equal to the above defined total slope angle. Furthermore, as the combined slope angle ratio increases, the magnitude of the difference between combined slope velocity strengths and total slope angle velocity strengths increases as well.

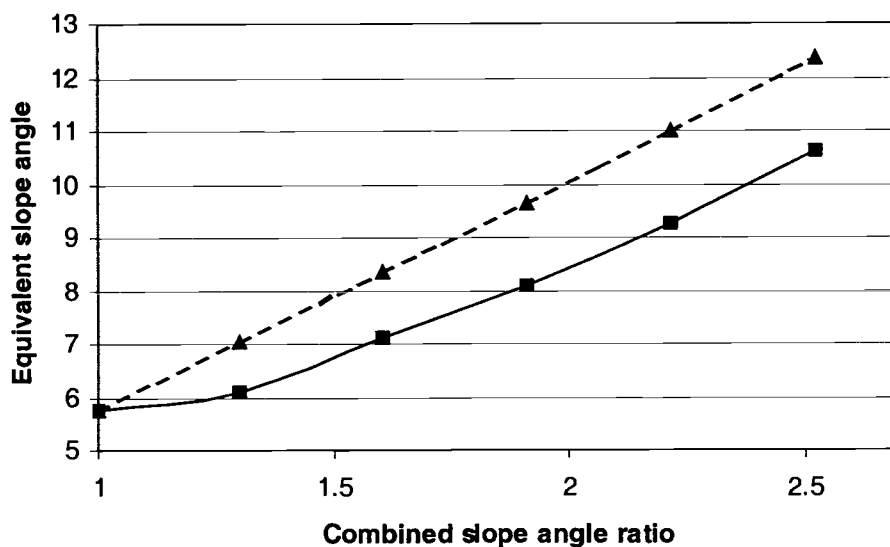


Figure 3.15: Equivalent slope angle (solid) versus combined slope angle ratio for the equivalent slope angle method. Also shown for comparison is the line where equivalent slope angle is equal to the total slope angle (dashed).

This phenomena is probably due to a combination of four factors. First, velocity strength scales grow faster over steeper than over less steep slopes. Second, steeper slopes convert buoyant potential energy into kinetic energy more

efficiently than gentler slopes. Third, slope length depends on slope angle, and velocity strength scales depend on both slope angle and slope length. And finally, there are finite mixing effects that occur in the vicinity of the slope discontinuity that significantly reduce the velocity strength scales of the combined flows.

The first two factors have been explored in chapter 2. The third factor, the increase of slope length with increasing slope angle for constrained horizontal distance, is discussed in section 2.4 and is small in magnitude.

Insight into the fourth factor is presented in figure 3.16, a plot of the total TKE as a function of down-slope distance. It can be seen that for all combined slope cases the TKE between the slope discontinuity (6000 m) and point A (8000 m) is significantly enhanced over that of the simple slope, indicating an increase in mixing which would tend to slow the flow down. In this section of the slope, the TKE is larger for larger combined slope angle ratios as well.

Further evidence is presented in figure 3.17, a plot of buoyancy, advection, and mixing and drag terms in the total momentum budget as a function of down-slope distance. In the transition part of the slope, between the slope discontinuity (6000 m) and point A (8000 m), mixing and drag in the combined slope flows are significantly enhanced relative to the that of simple slope flows, while the driving force behind the flow, the buoyancy term, relaxes to that which would be found over simple slopes, in a much shorter distance. This figure also shows that, in the above mentioned section of slope, mixing and drag is higher for higher combined slope angle ratio, whereas the magnitude of the buoyancy term is relatively constant for all combined slope angle ratios.

Thus, the combined flow cannot be simply equated as a combination of two simple slope flows, since the transition portion of the flow constitutes a period of enhanced mixing and drag that cannot be easily predicted. In conclusion, the parameterization of subgrid terrain features has been shown to be a difficult problem. In the case that the differences between actual terrain and the model resolved terrain are known, one can make adjustments to model predicted drainage flows to account for unresolved slope angle changes. However, the magnitude of those adjustments are not well known due to the effects of the increase in mixing that occurs in the turbulent hydraulic jump near the slope angle change. As the difference between the upper and lower slope angle increases, mixing increases in the turbulent hydraulic jump near the slope angle. Qualitatively, it is straightforward to apply results obtained through the sensitivity study of the effect of slope angle on simple slope flows to predictions for combined katabatic flow parameters. However, one must be careful to take into account the ratio of combined slope angles, and the lengths of the slopes, in determining how much katabatic flows will be decreased due to the presence of subgrid scale terrain features.

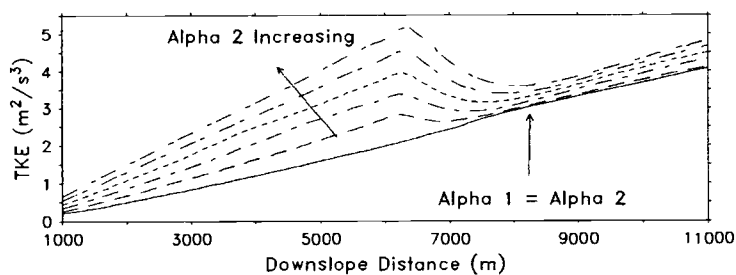


Figure 3.16: Total turbulent kinetic energy as a function of down-slope distance for upper slope angle runs.

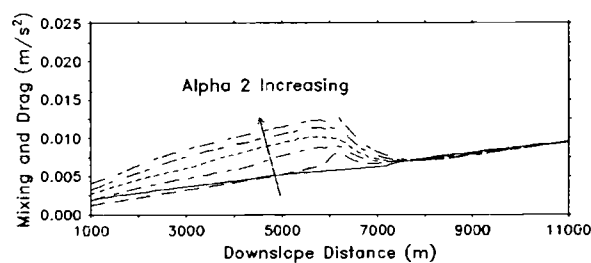
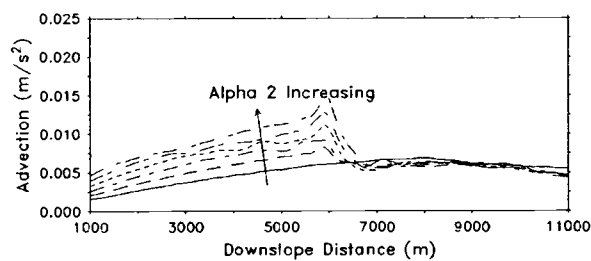
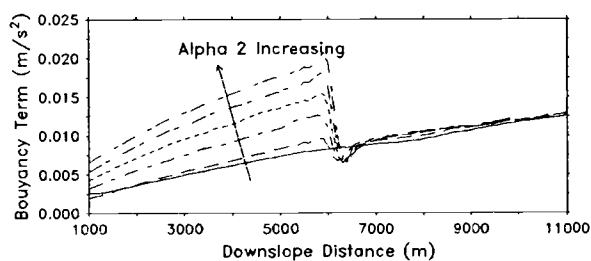


Figure 3.17: Buoyancy (top), advection (middle), and mixing and drag (bottom) terms in the total momentum budget as a function of down-slope distance for upper slope angle runs.

4. Conclusions

A modeling study of katabatic flows has been performed. The objectives of this study included a comparison between a large eddy simulation and a mesoscale model of katabatic flows, and investigations into the effect of surface heat fluxes, ambient stratification, and slope angle on katabatic flows. An examination of the difference between katabatic flows over simple slopes versus those over combined slopes was performed, with further investigation of the effect of changing upper slope angle on katabatic flows down-slope of the slope angle change. Qualitative methods in which subgrid scale terrain features may be accounted for in models of katabatic flows in areas of inadequate terrain resolution were suggested. Finally, buoyant potential energy and katabatic flow efficiency parameters were introduced in order to study the energy conversion characteristics of slope flows.

The first objective of this study was to make a comparison between a large eddy simulation and a mesoscale model of katabatic flows. The models were in qualitatively good agreement on a number of flow parameters. In particular, down-slope flow velocity profiles matched well, but a discrepancy between the potential temperature deficit profiles was noted, with the LES model cooling more near the surface than the ARPS model. An examination of the momentum budget revealed further insight to the physics of the flow. It was noted that ARPS produced relatively higher rates of horizontal advection away from the surface than did the LES model, but otherwise the momentum budgets were very similar. Finally, a comparison of TKE budgets provided a way to verify the subgrid model of ARPS.

Although qualitatively in agreement with each other, ARPS had relatively higher amounts of TKE, which was due to an overproduction by shear.

Secondly, the effect of surface heat fluxes on katabatic flows was examined. It was determined that down-slope velocity and potential temperature are strongly dependent on surface heat fluxes. Momentum budgets of the flows revealed the self similar behavior of katabatic flows with respect to surface heat fluxes. That is, increased surface cooling leads to increases in the buoyancy force, mixing and drag, and advection. Furthermore, total advection to mixing ratios for the flows were nearly identical, which explains the very weak dependence of katabatic efficiency on surface heat fluxes, with larger inputs of buoyant potential energies (from increased surface cooling) leading to larger kinetic energies on similar scales. In addition, parameterizations of velocity and buoyancy strength scales as a function of surface heat fluxes were developed.

The third objective of this study was to look at the effect of ambient stable stratification on katabatic flows. It was found that velocity and potential temperature deficit fields are strongly affected by stable ambient stratification. Entrainment of ambient air into the flow was found to be strongly dependent on ambient stratification, and for the very stable case, mixing and drag was found to be more important than advection. The velocity and potential temperature fields of the flows revealed that at high ambient stratifications, katabatic flows can become one-dimensional and cease growing in the down-slope direction. In this case, the momentum budget of the flows becomes a balance between the buoyancy force and mixing and drag, with entrainment of ambient air into flow becoming small.

Furthermore, as stable stratification increases, buoyant potential energy goes down, leading to less kinetic energy, as well as less efficient energy conversion.

Next, the effect of slope angle on katabatic flows was examined. Steeper slope angles create stronger, deeper velocity profiles, and larger velocity strength scales. At the same time, potential temperature deficits decrease since surface cooling was held constant. Although this is probably not a realistic assumption, in the absence of observational data to confirm or refute this, use of this simplistic thermodynamic surface condition is justified. It is expected that sensible heat loss from the surface would increase as surface velocities increase, but as flow progresses down-slope, the near surface air temperature approaches that of the surface, thus decreasing surface heat fluxes. Hence, the down-slope variation of surface heat fluxes for katabatic flow is an issue that needs to be looked into further. In addition, parameterizations of velocity and buoyancy strength scales as a function of slope angle were developed. Katabatic efficiencies increase with increasing slope angle, which, under the constraint of equal horizontal distance, also implies an increase in slope height and hence a larger buoyant potential energy input to the system, which leads to greater kinetic energy down-slope. Parameterizations developed in this section are subsequently used in the equivalent slope angle method of chapter 3.

The fourth objective of the study was to examine the difference between katabatic flows on simple and combined slopes. It was found that near the foot of the slope, simple slopes produce higher velocities and hence smaller potential temperature deficits than combined slopes. On the lower portion of the slope, the combined flow has less adv, and less TKE than that of the simple flow, which

explains why the simple flow is deeper here than that of the combined flow. One important difference between simple and combined flows is that parcels on the simple slope have more buoyant potential energy than those of the combined flow. This is a simple consequence of geometry, since the simple slope everywhere has higher terrain than the combined slope. It follows that simple slope flows will derive larger kinetic energies from larger amounts of buoyant potential energy than combined flows.

Finally, an investigation into the effect of a changing upper slope angle on katabatic flows over combined slopes was made to determine if the effect of subgrid scale terrain features can be accounted for in models. The effects of changing upper slope angle on katabatic flows over the lower portion of the slope are complex, and an equivalent slope angle method is proposed to help tailor katabatic flow predictions in areas of inadequate terrain resolution. In this method, results derived from earlier studies are used, namely, that katabatic efficiency is a function of slope angle, and velocity strength scales, which can be predicted for simple slopes based on the physical parameters of the flow, grow with down-slope distance. Predictions of strength scales for combined slopes exhibit a complex behavior that can decrease katabatic flows relative to that of simple slopes. One reason for this is due to the region of enhanced mixing just down-slope of the slope angle change. Regions such as this represent a challenge to predictions of slope flows in areas of complex terrain, and further study into their effects is warranted. In that the effect of subgrid scale terrain features is not altogether straightforward, it is necessary to have accurate knowledge of actual versus modeled terrain profiles in order to make prediction adjustments to account for subgrid scale terrain features. Furthermore, since the difference between actual and modeled terrain is a function

of grid spacing, the effects of subgrid scale terrain features may vary from model to model, but will most likely follow along a consistent pattern. Namely, in areas of inadequate resolution, buoyant potential energies will probably be increased as concave mountain profiles are smoothed over, and terrain heights are raised, and the effect of an increase in buoyant potential energy along a slope is to increase kinetic energy down-slope, thus overestimating katabatic flow strengths.

References

- Bader, D. C., McKee, T. B., and Tripoli, G. J., 1987: Mesoscale Boundary Layer Evolution over Complex Terrain. Part I: Numerical Simulation of the Diurnal Cycle. *J. Atmos. Sci.*, 44, 2823-2838.
- Bader, D. C., and T. B. McKee, 1983: Dynamical simulation of the morning boundary layer development in deep mountain valleys. *J. Climate Appl. Meteor.*, 22, 341-351.
- Ball, F. K., 1956: The theory of strong katabatic winds. *Aust. J. Phys.*, 9, 373-386.
- Banta, R. and Cotton, W., 1981: An analysis of the structure of local wind system in a broad mountain basin. *J. Appl. Meteorol.* 20, 1255-1266.
- Davies, T., Palutikof, J., Guo, X., Berkofsky, L., and Halliday, J., 1995. Development and testing of a two dimensional downslope wind model. *Boundary-Layer Meteor.*, 73, 279-297.
- Deardorff, J. W., 1980. Stratocumulus-capped mixed layers derived from a three-dimensional model. *Boundary-Layer Meteor.*, 18, 495-527.
- Defant, F., 1949: Zur theorie der Hangwinde, nebst Bemerkungen zur Theorie der Berg- und Talwinde. *Arch. Meteor. Geophys. Bioklim.*, A1, 421-450.
- Denby, B., 1999: Second order modeling of turbulence in katabatic flows. *Boundary-Layer Meteor.*, 92, 67-100.
- Doran, J.C., and T.W. Horst, 1983: Observations and models of simple nocturnal slope flows. *J. Atmos. Sci.*, 40, 708-717.
- Doran, J.C., and C. D. Whiteman, 1990: The development and structure of nocturnal slope winds in a simple valley. *Boundary-Layer Meteor.*, 52, 41-68.
- Doran, J.C., J.D. Fast, and J. Horel, 2002: The VTMX 2000 campaign. *Bull. Amer. Meteor. Soc.*, 83, 537-551
- Ducros, F, Comte, P, Lesieur, M, 1996: Large-eddy simulation of transition to turbulence in a boundary layer developing spatially over a flat plate. *J. Fluid Mech.* 326, 1-37.
- Ellison, T. H., and J. S. Turner, 1959: Turbulent entrainment in stratified flows. *J. Fluid Mech.*, 6, 423-448.

- Fitzjarrald, D. R., 1986: Slope winds in Veracruz. *J. Climate. Appl. Meteorol.*, 25, 133-144.
- Fleagle, R. G., 1950: A theory of air drainage. *J. Meteor.*, 7, 227-232.
- Hassid, S., and Galperin, B., 1983. A turbulent energy model for geophysical flows. *Boundary-Layer Meteor.*, 26, 397-412.
- Horst, T.W., and J.C. Doran, 1986: Nocturnal drainage flow on simple slopes. *Boundary-Layer Meteor.*, 34, 263-286.
- Horst, T., and Doran, J., 1988. The turbulence structure of nocturnal slope flow. *J. Atmos. Sci.*, 45, 605-616.
- Klemp, J. B., and Lilly, D. K., 1978. Numerical simulation of hydrostatic mountain waves. *J. Atmos. Sci.*, 35, 78-107.
- Kondo, H. and Sato, T., 1988: A simple model of drainage flow on a slope. *Boundary-Layer Meteor.*, 43, 103-123.
- Mahrt, L., 1982: Momentum balance in gravity flows. *J. Atmos. Sci.*, 39, 2701-2711.
- Mahrt, L., D. Vickers, R. Nakamura, M. R. Soler, J. Sun, S. Burns, and D.H. Lenschow, 2001: Shallow drainage flows. *Boundary-Layer Meteor.*, 101, 243-260.
- Manins, P.C., and B.L. Sawford, 1979a: A model of katabatic winds. *J. Atmos. Sci.*, 36, 619-630.
- Manins, P.C., and B.L. Sawford, 199b: Katabatic winds: A field case study. *Quart. J. Roy. Meteor. Soc.*, 105, 1011-1025.
- Mellor, G. L., and T. Yamada, 1974: A hierarchy of turbulence closure models for planetary boundary layers. *J. Atmos. Sci.*, 31, 1791-1806.
- Moeng, C. H., 1984: A large eddy simulation model for the study of planetary boundary layer turbulence. *J. Atmos. Sci.*, 41, 2052-2062.
- Monti, P., Fernando, H. J. S., Princevac, M., Chan, W. C., Kowalewski, T. A., Pardyjak, E.R., 2002. Observations of flow and turbulence in the nocturnal boundary layer over a slope. *J. Atmos. Sci.*, 59, no 17, 2513-2534.

Nappo, C. J. and S. Rao, 1987: A model study of pure katabtic flows. *Tellus*, 39A, 61-71.

Papadoupoulos, K. H., and C. G. Helmis, 1999: Evening and morning transistion of katabatic flows. *Boundary-Layer Meteor.*, 92, 227.

Papadopoulos, K. H., Helmis, C. G., Soilemes, At T., Kalogiros, J., Papageorgas, P. G., and Asimakopoulos, D. N., 1997: The structure of katabatic flows along a simple slope. *Quart. J. Roy. Meteorol. Soc.* 123, 1581-1601.

Prandtl, L.: 1942: *Stromungslehre*, Vieweg und Sohn, Braunschweig, 382 pp.

Prandtl, L., 1952: *Essentials of Fluid Dynamics*. Hafner Publishing Co., New York, 452 pgs.

Rao, K.S., and H.F. Snodgrass, 1981: A nonstationary nocturnal drainage flow model. *Boundary-Layer Meteor.*, 20, 309-320.

Skyllingstad, E. D., 2003: Large eddy simulation of katabatic flows. *Boundary-Layer Meteor.*, 106, no. 2, 217-243

Skyllingstad, E. D.; Smyth, W. D.; Crawford, G. B., 2000, Resonant wind-driven mixing in the ocean boundary layer. *Journal of Physical Oceanography* 30, no. 8 (2000): 1866-1890

Stull, R. B., 1988: *An Introduction to Boundary Layer Meteorology*. Kluwer Academic, 666 pp.

Xue M, Droegemeier KK, Wong V, 2000: The Advanced Regional Predictoin System (ARPS) – A multi-scale nonhydrostatic atmospheric simulation and prediction model. Part I: Model dynamics and verification. *Meteorology and Atmospheric Physics*, 75, 161-193

Yamada, T., 1981: A numerical simulation of nocturnal drainage flows with strong wind and temperature gradients. *J. Appl. Meteor*, 28, 545-554.